Fall 2020

Removal of non-metallic inclusions from molten steel by ceramic foam filtration

Soumava Chakraborty

REMOVAL OF NON-METALLIC INCLUSIONS FROM MOLTEN STEEL BY CERAMIC FOAM FILTRATION

by

SOUMAVA CHAKRABORTY

A DISSERTATION

Presented to the Graduate Faculty of the

MISSOURI UNIVERSITY OF SCIENCE AND TECHNOLOGY

In Partial Fulfillment of the Requirements for the Degree

DOCTOR OF PHILOSOPHY

in

MATERIALS SCIENCE AND ENGINEERING

2020

Approved by:

Ronald J. O'Malley, Advisor
Laura Bartlett
Mingzhi Xu
Von Richards
Kamalesh Mandal

PUBLICATION DISSERTATION OPTION

This dissertation consists of the following three articles, formatted in the style used by the Missouri University of Science and Technology:

Paper I, found on pages 23–60, has been published online in *International Journal of Metalcasting*.

Paper II, found on pages 61–91, has been published in the Proceedings of the Iron and Steel Technology Conference in Pittsburgh, PA, USA in May 2019.

Paper III, found on pages 92–127, is intended for submission to *International Journal of Metalcasting*.

ABSTRACT

Ceramic filters are routinely used in steel foundries to remove non-metallic inclusions from steel melt. Removal efficiency for both solid and liquid inclusions by magnesia-stabilized zirconia foam filters (10ppi) were evaluated and distribution of the captured inclusions through the filter thickness was also investigated. A mold design was developed using a commercial computational fluid dynamics software package to produce two castings that fill simultaneously, one with a filter and the other without a filter, from a single ladle pour, while also matching the fill rates and avoid turbulence and reoxidation during pouring. An industrial-scale experiment was also performed to investigate the distribution of captured inclusions through the filter thickness for higher inclusion loading compared to that of laboratory-scale experiments.

Inclusion removal efficiency was observed to be strongly dependent on the initial inclusion concentration. Solid alumina inclusions are found to be captured within the filter at the metal-filter macropore interface. The concentration of the captured solid inclusions decreased exponentially from the entry to exit side of the filter, following first order capture kinetics. Liquid inclusions were captured within the micropores of the ceramic web structure and at the metal-filter macropore interface. The captured liquid inclusion concentration within filter micropores also followed an exponential trend for lower inclusion loading, whereas it became constant for higher inclusion loading due to complete saturation of the ceramic web micropores. Upon filter micropore saturation, continuous liquid inclusion films developed at the metal-filter macropore interface, increasing the possibility for the release of large liquid inclusions from the filter.

ACKNOWLEDGMENTS

First and foremost, I would like to thank Dr. Ronald J. O'Malley, my advisor, for his support, guidance, motivation, and his belief in me. Thanks for all the advice, both personal and professional, of which I will be forever indebted.

Thanks to Dr. Laura Bartlett for the advice and numerous discussions. I would also like to thank Dr. Mingzhi Xu, Dr. Von Richards, and Dr. Kamalesh Mandal for their time and valuable inputs to this work. Thanks to the Department of Materials Science and Engineering for helping me throughout my stay at Missouri S&T.

I also wish to thank the participating member companies and the industry mentoring committee of the Peaslee Steel Manufacturing Research Center (PSMRC) at the Department of Materials Science and Engineering of Missouri S&T for funding this research and providing the technical guidance.

I am grateful to all the professors, graduate researchers, undergraduate researchers, and the staffs of the Department of Materials Science and Engineering of Missouri S&T for their immense help and support.

Finally, lots of love to my wife Mousumi and my daughter Samsthita for bringing smiles to my face during the tough times and being a ball of happiness. I would like to thank my parents for their understanding and unconditional support during my doctoral study. This journey, during which I have seen highs and lows in life, would never have been possible without blessings from the Almighty.

TABLE OF CONTENTS

LIST OF ILLUSTRATIONS

SECTION Page

PAPER I

PAPER II

SECTION

LIST OF TABLES

1. INTRODUCTION

1.1. BACKGROUND INFORMATION

Non-metallic inclusions can be formed during the melting, pouring and casting of steelmaking processes. They are classified into two main categories of endogenous and exogenous inclusions. Endogenous inclusions are produced during refining and post-solidification of molten steel, and accordingly they are termed as primary or secondary inclusions. These inclusions can be oxides, sulfides, nitrides, carbides etc. and various complex combinations of them [1, 2]. Exogenous inclusions come from sources outside the refining process, such as worn refractories, slag, sand, or by reoxidation of the melt and are often much larger than endogenous inclusions [3-5].

Molten steel contains variable amount of dissolved oxygen depending on the steel grade and due to the low solubility of the dissolved oxygen, it reacts with the carbon present in steel to form carbon monoxide gas. The formation of carbon monoxide creates blowholes in the casting. These defects are undesirable and reduce the quality of the castings [6-8]. Deoxidation of molten steel is thereby important in steelmaking practices to scavenge out the dissolved oxygen from molten steel, which leads to formation of non-metallic inclusions.

Evolution of nonmetallic inclusions is composed of three stages: (i) nucleation, (ii) growth and (iii) floatation. Inclusions nucleate in liquid steel when the thermodynamic driving force (Gibbs free energy) of their formation reaction is negative. Growth occurs when a critical radius of the nucleus is exceeded. Diffusion, local thermodynamics, Ostwald ripening, or physical agglomeration are the primary

mechanisms for the growth of a non-metallic inclusions. Sub-micron sized inclusions are affected by Brownian collision and therefore get agglomerated. Larger inclusions are more affected by molten metal flow. Agglomeration leads to removal of non-metallic inclusions by floatation and this process is more efficient for the liquid inclusions compared to the solid inclusions. For unstirred systems with low Reynolds numbers Stokes' Law can be implemented to estimate the rising velocity of the inclusion particles, as represented in Equation (1). For stirred systems with high Reynolds number, the inclusion agglomeration occurs due to macroscopic velocity and turbulence of the molten metal.

$$v_s = \frac{2(\rho_p - \rho_f)}{9\mu} g R^2 \tag{1}$$

where v_s is the particle velocity, ρ_p is the particle density, ρ_f is the fluid density, g is the gravitational constant, and R is the particle radius. [9, 10]

1.2. DEOXIDATION PRACTICES

In steel industries, different types of deoxidizers, such as, aluminum, silicon, manganese, calcium, titanium etc., their ferroalloys and the combination of these ferroalloys, are mostly used [2]. These deoxidizers react with dissolved oxygen present in liquid metal and form oxide inclusions. Removal of these oxide inclusions are very much essential to maintain the quality and appearance of the castings [11].

Aluminum is the most commonly used deoxidizer because of its ability to produce steel having with very low oxygen potential. Figure 1.1 is the deoxidation equilibria for aluminum in liquid steel with 0.2wt% C at 1600 ˚C [12]. At sufficient levels of addition, it generates solid alumina inclusions in the steel melt. These inclusions can be of different

shapes, such as, spherical, dendritic etc., as represented in Figure 1.2 [13], depending on the oxygen content of the steel melt. Alumina inclusions tend to attract each other and form clusters [14]. The chemical reaction for alumina inclusion formation is shown in Equation (2).

$$2[Al] + 3[O] = (Al_2O_3)_{solid} \quad (2)$$

Alumina inclusions generated in molten steel can be further treated with calcium to generate calcium aluminate inclusions. Calcium modification of alumina inclusions in steel at various temperatures are shown in Figure 1.3 [12]. Formation of spherical liquid inclusions, as shown in Figure 1.4 [15], can be represented by the chemical reaction given in Equation (3).

$$[Ca] + [O] + (Al_2O_3)_{solid} = (CaO.Al_2O_3)_{liquid} \quad (3)$$

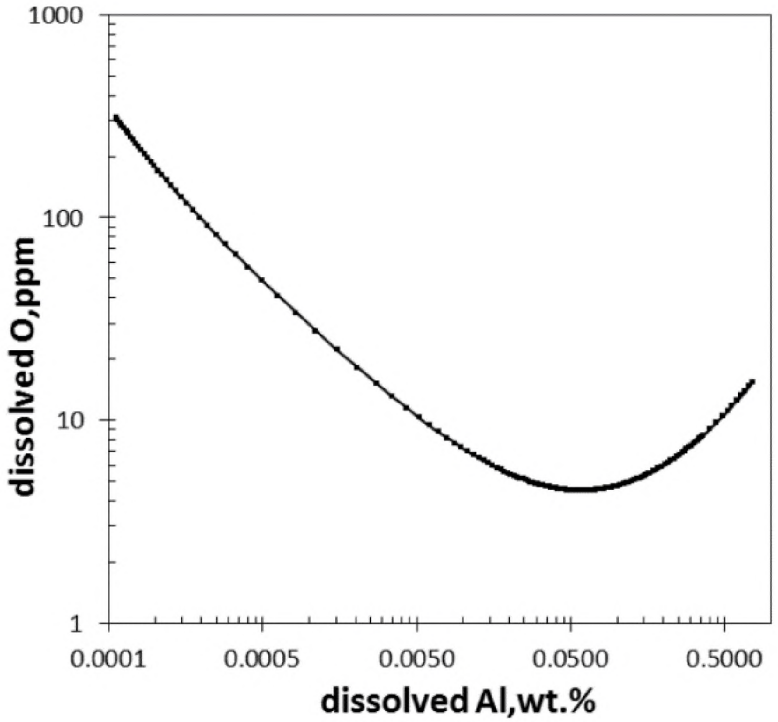

Figure 1.1. Aluminum deoxidation equilibria in liquid steel [12].

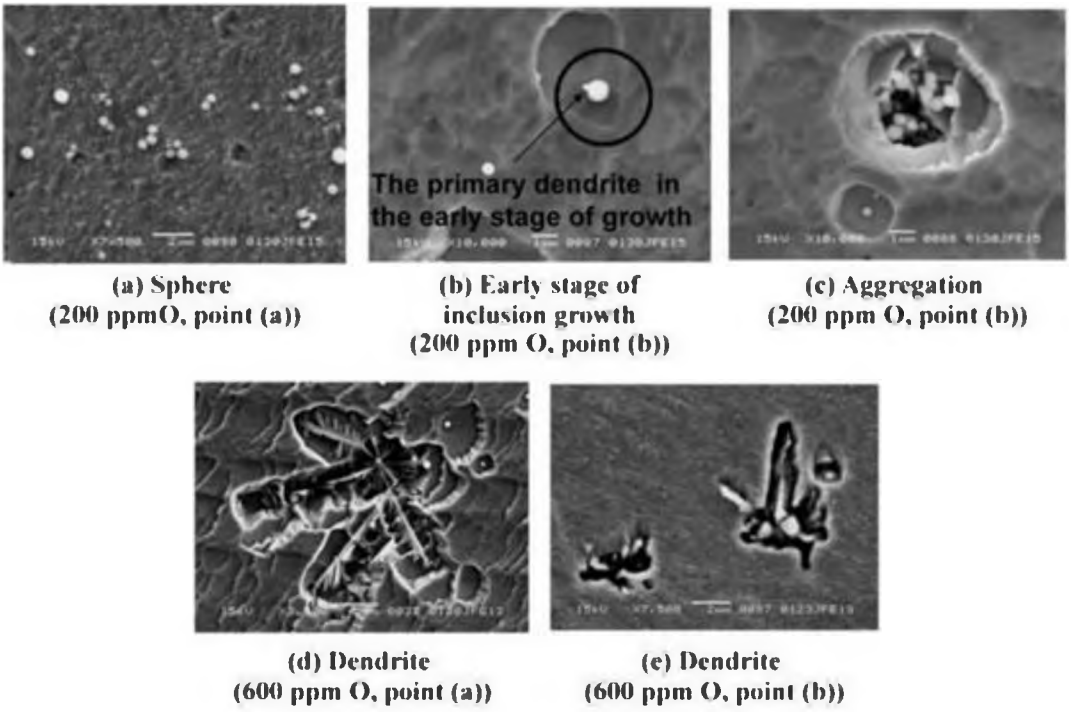

Figure 1.2. Alumina inclusions [13].

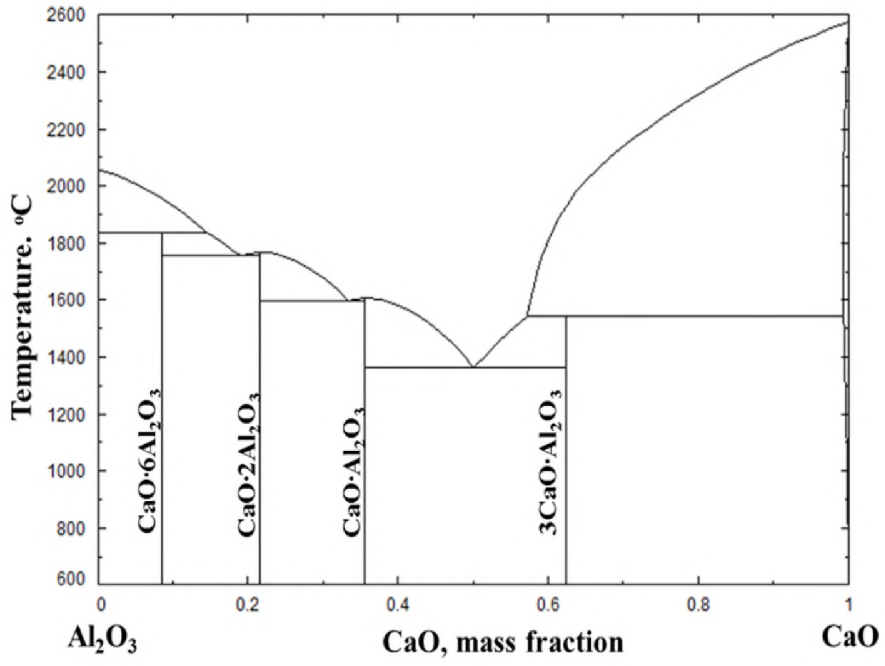

Figure 1.3. Calcium modification of alumina inclusions [12].

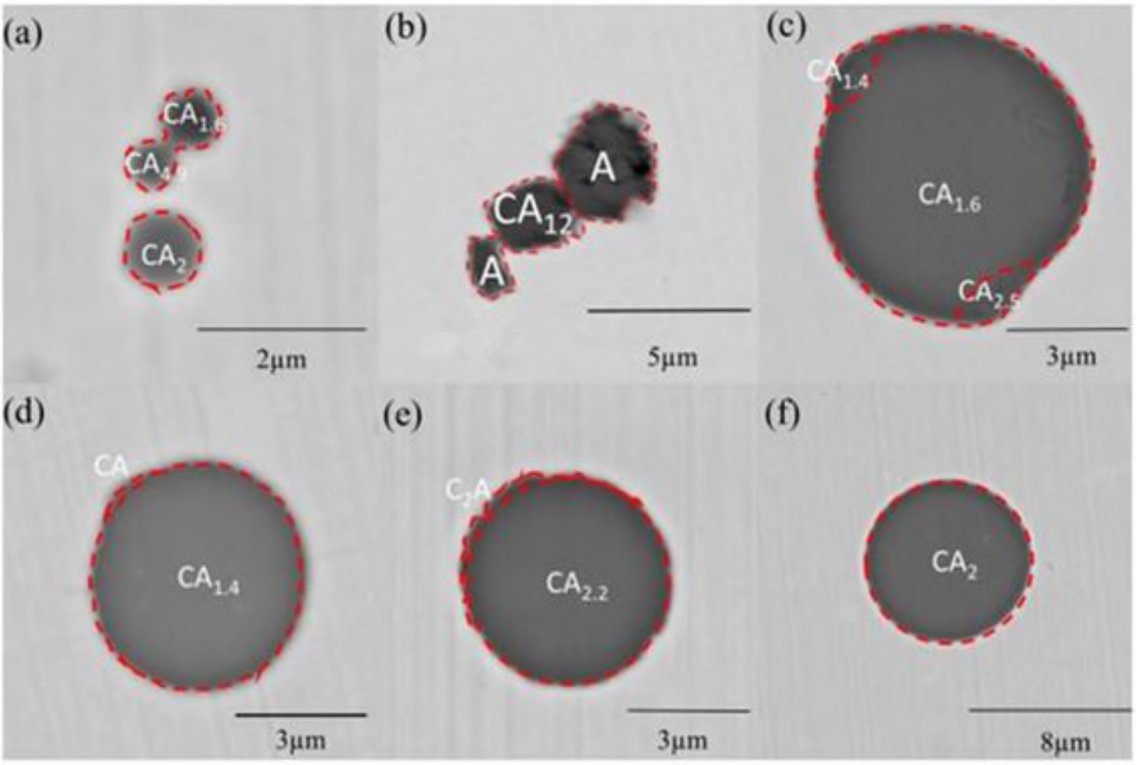

Figure 1.4. Calcium aluminate inclusions [15].

Silicon and manganese are also used as deoxidizers and react with dissolved oxygen present in molten steel. The activity of silica in manganese silicate (in case of SiMn deoxidation) is lower than solid silica (in case of Si deoxidation only) which drives deoxidation process more efficiently [2, 16]. The formation of liquid manganese silicate or solid silica depends on the silicon to manganese ratio present at the steelmaking temperatures, as shown in Figure 1.5 [2]. These liquid manganese silicate inclusions are spherical in shape and are represented in Figure 1.6 [17]. The chemical reaction for manganese silicate inclusion formation is shown in Equation (4).

$$x[Mn] + y[Si] + (x+2y)[O] = (xMnO, ySiO_2)_{liquid} \quad (4)$$

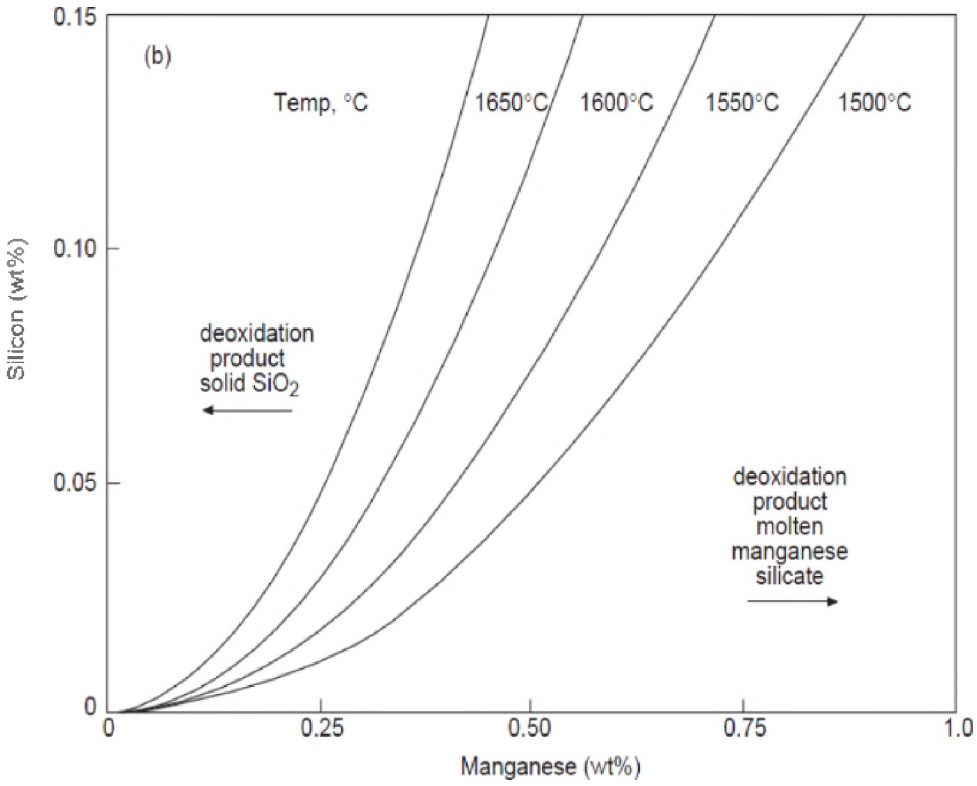

Figure 1.5. Equilibrium relations for deoxidation of steel with Si and Mn [2].

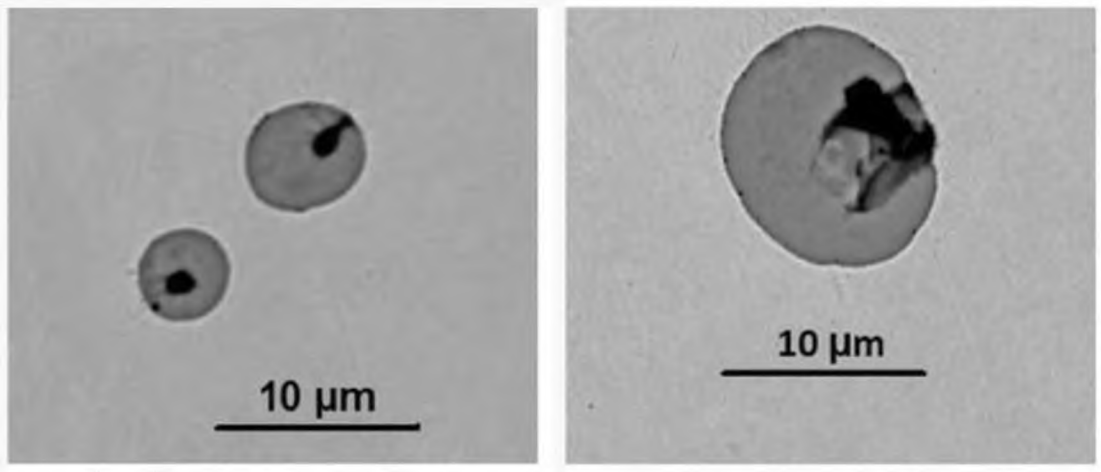

Figure 1.6. Manganese silicate inclusions [17].

1.3. CERAMIC FILTERS AND STEEL FILTRATION

Non-metallic inclusions in steel can reduce mechanical properties, impact machinability, produce surface defects and increase scrap rates and their removal is critical for the steel quality [11]. These inclusions can be removed from molten steel by various processes. Argon stirring in steel melt is generally used in integrated and mini mills [18-20]. In foundry steelmaking, steel melt filtration is the common practice for removal of primary endogenous inclusions [21-24]. Ceramic foam filters are commonly utilized in multiple positions in the gating system of sand molds, as shown in Figure 1.7 [25], and are effective by a deep bed filtration mechanism [26]. Secondary endogenous inclusions cannot be captured by the ceramic filters as they formed during or after solidification of steel.

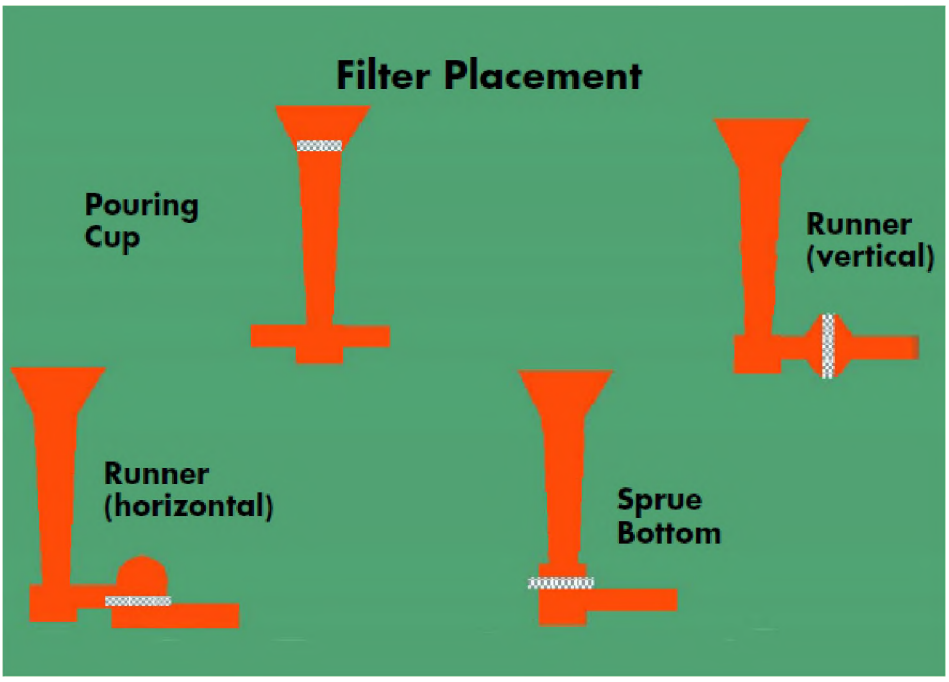

Figure 1.7. Gating system locations where filters are commonly placed [25].

Ceramic filters can be of different types according to their compositions. Due to the high chemical and mechanical stabilities at steelmaking temperatures, zirconia filters are most commonly used in steel foundries [27]. Zirconia filters can be of many types according to their shapes, such as loop filters, multi-hole filters, monolithic filters, foam filters etc. [26, 28-32], as shown in Figure 1.8 [26, 30-32]. Primary endogenous inclusions can be captured by these different types of zirconia filters, the choice of which depends on the specific application and location in the process.

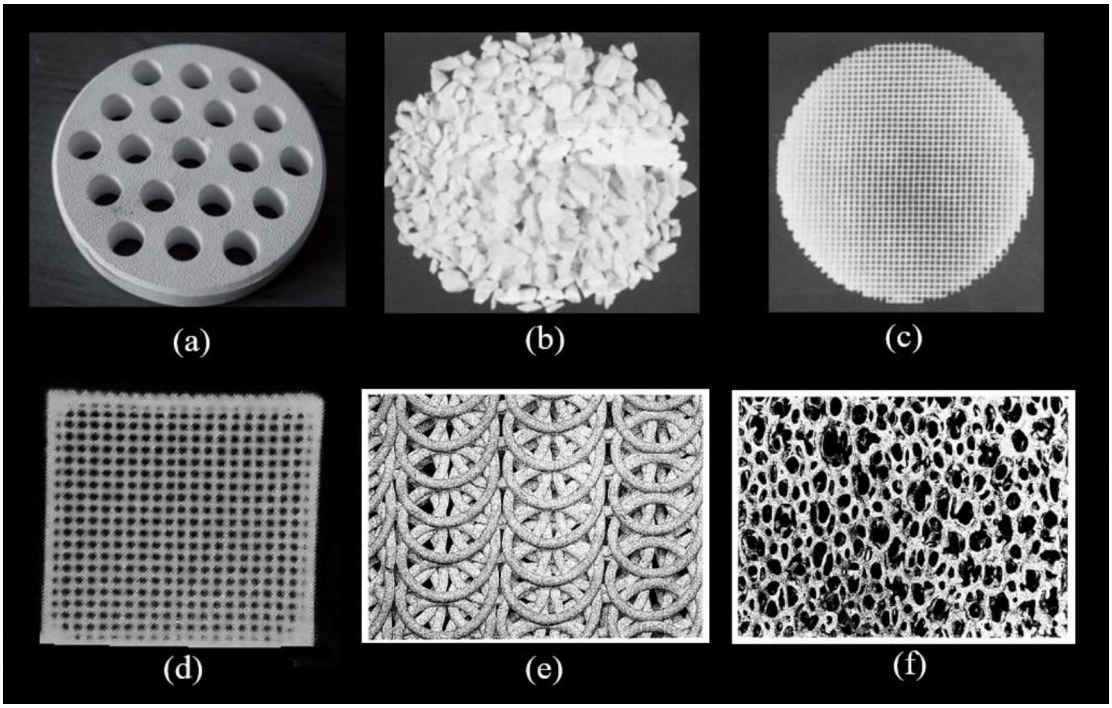

Figure 1.8. Different types of ceramic filters [26, 30-32]: (a) multi-hole filter, (b) tabular filter, (c) monolithic filter, (d) cellular filter, (e) loop filter and (f) foam filter.

Filtration of both solid and liquid inclusions from steel melts have been reported by several authors [26, 29, 33-41], as shown in Figure 1.9 [35], though the mechanisms are different and will be discussed in the following section. Turbulent metal flow helps

the inclusions to attach with the filter surface [42]. Another important aspect of using ceramic filters is to modify the velocity of the incoming metal [43-45], as represented in Figure 1.10 [37]. A previous study showed that many defects, such as macroporosity, microporosity and mold erosion and consequential sand inclusions can arise due to higher filling rate or velocity and introducing a ceramic filter at various positions in the gating system helps to reduce such defects by modifying the metal flow from turbulent to streamline [46].

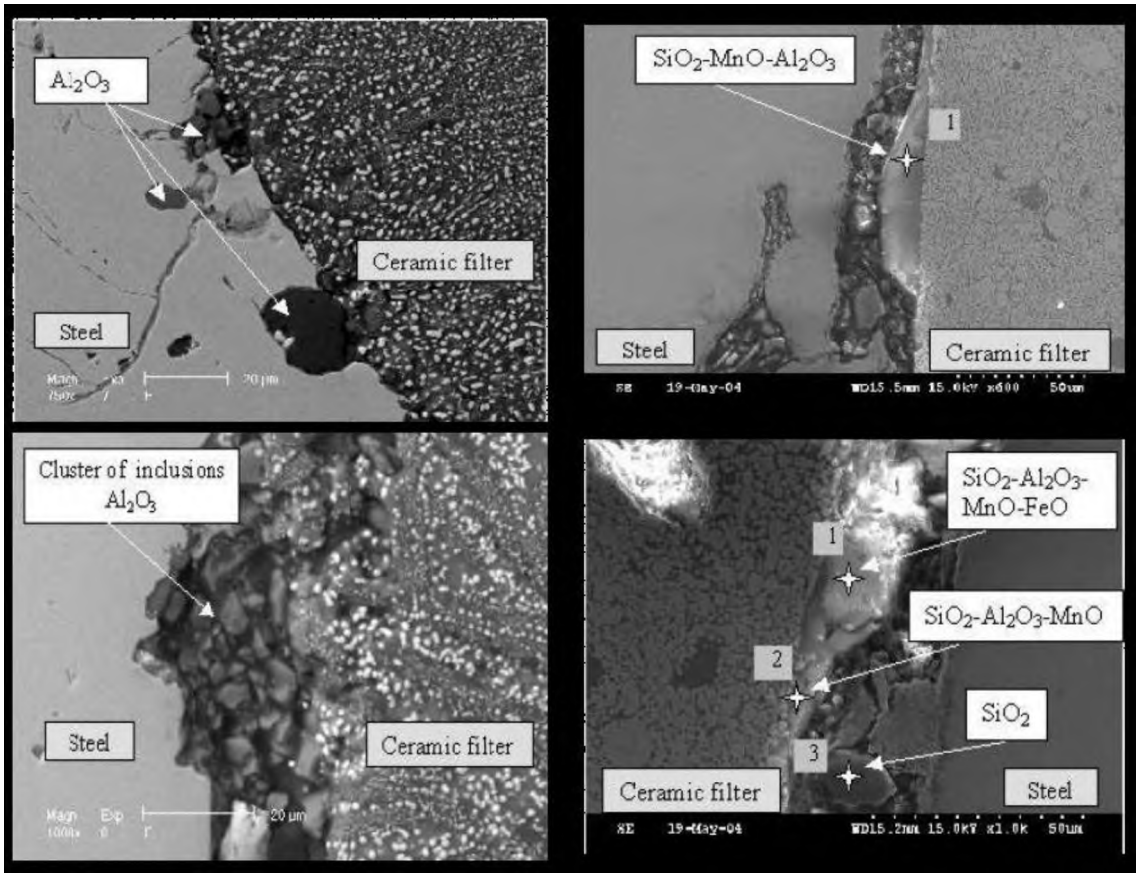

Figure 1.9. Removal of solid and liquid inclusions using ceramic filters [35].

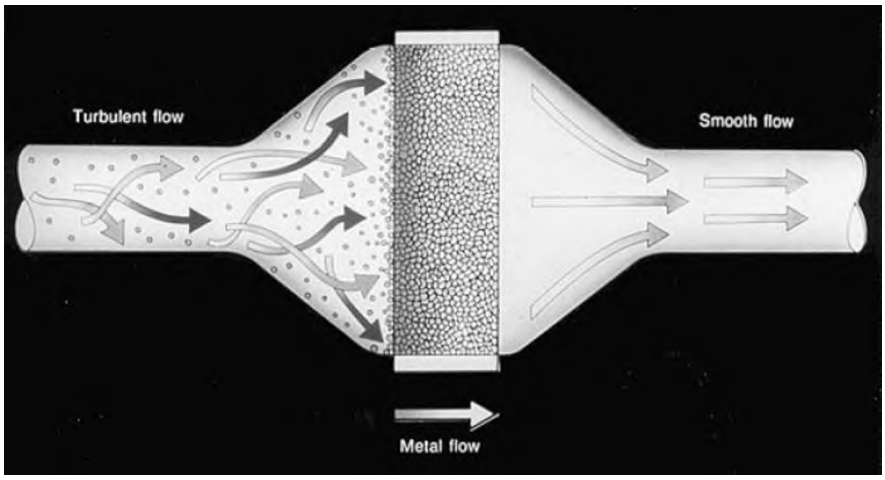

Figure 1.10. Ceramic filter as flow modifier [37].

1.4. RESEARCH OBJECTIVES

The objectives of this research are to understand, investigate and document the removal efficiency, capture mechanism and kinetics of various non-metallic oxide inclusions. Specific tasks include:

1. To design a mold based on computational fluid dynamics modeling for estimating the removal efficiency of non-metallic inclusions by a ceramic filter.
2. To compare the filtration efficiency of various non-metallic inclusions by utilizing a common casting pattern.
3. To understand the influence of physical state of the non-metallic inclusions on the capture mechanism.
4. To investigate the capture kinetics through the thickness of the ceramic filters.
5. To document the effect of non-metallic inclusion loading on filtration efficiency and removal kinetics.

The current research work builds on the knowledge and previous researches at Missouri S&T on formation and evolution of non-metallic inclusions, their characterization techniques, and post processing analyses for different steel grades [12, 47-50].

2. LITERATURE REVIEW

2.1. THERMODYNAMICS OF FILTRATION PROCESS

In previous literatures, thermodynamic models were developed to predict the spontaneous attachment of non-metallic inclusions on ceramic filter [34, 51-53]. The surface area of the inclusions, the contact angle and interfacial tension between inclusion and filter were found to be directly proportional to the Gibbs free energy change during filtration [29, 51]. The adsorption force between a ceramic loop or monolithic filter and a spherical inclusion particle was determined to be higher than for two spherical inclusion particles, which helped the non-metallic inclusions to attach to the filter surface [52].

Removal of solid inclusions depend on the interfacial energy (γ) relationships between inclusions (I), filter (F) and metal (M), as shown in Equation (5), where ΔG is the Gibbs free energy of the system. Solid inclusions remain attached to the filter surface when Gibbs free energy is negative. If both the filter and inclusions are non-wetted by the melt, as shown in Figure 2.1 [34], then a capillary withdrawal of metal occurs at the interfacial region between the filter and inclusions [53], as represented in Figure 2.2 [34]. This capillary withdrawal of molten metal is followed by a sintering of solid inclusions with the ceramic filter, which actually helps the inclusions to remain attached [52]. Al_2O_3 and ZrO_2 have very high contact angles (135° and 122° respectively) with molten steel at steelmaking temperature and hence Al_2O_3 inclusions can be very effectively filtered using zirconia filters [53].

$$\Delta G = \gamma_{IF} - \gamma_{MF} - \gamma_{MI} \tag{5}$$

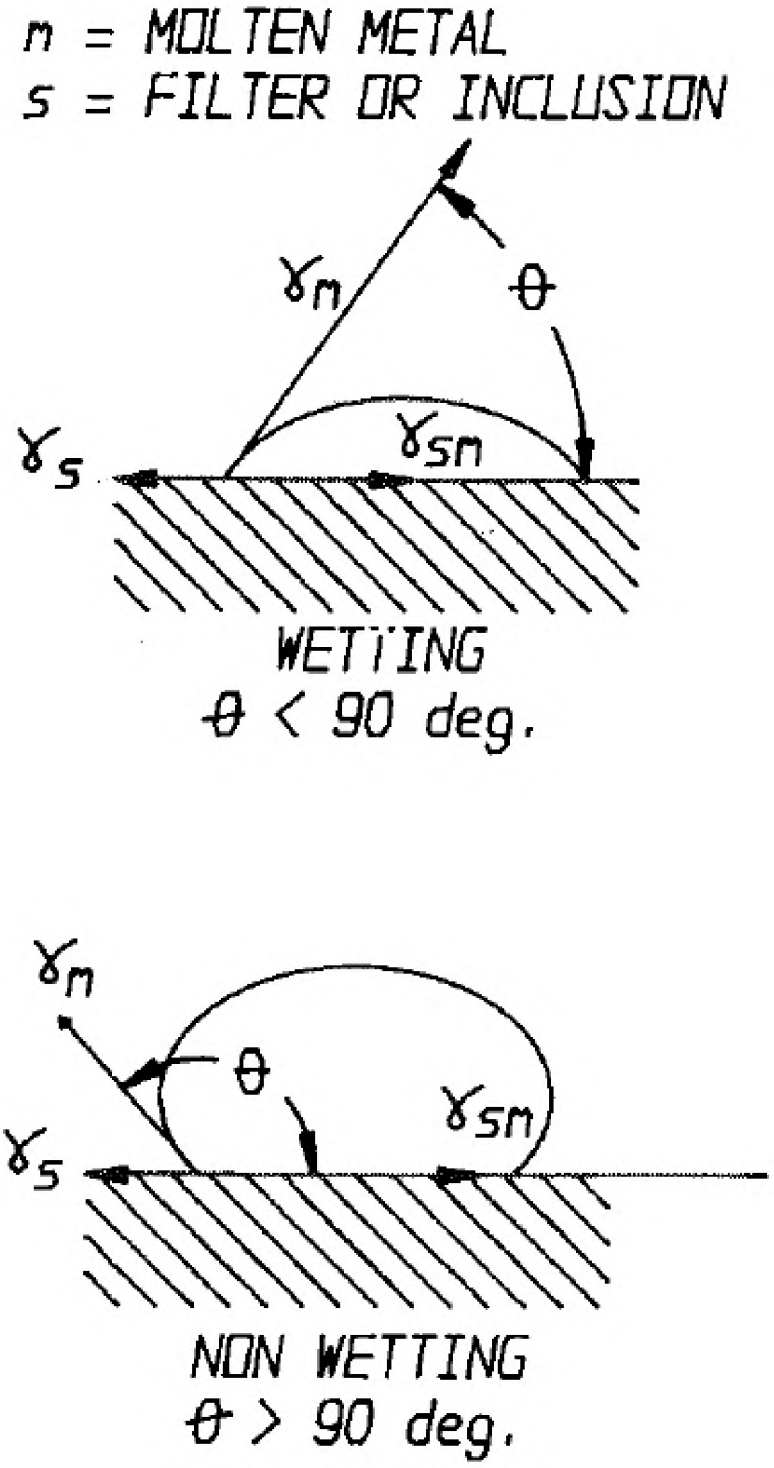

Figure 2.1. Shape of a liquid droplet on filter surface for non-wetting (θ>90°) and wetting (θ<90°) conditions [34].

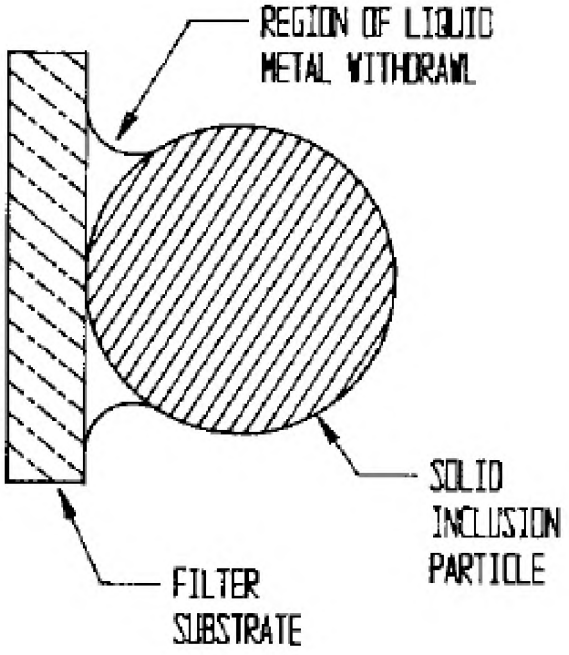

Figure 2.2. Capillary withdrawal of molten metal from the interfacial region between the filter surface and inclusions [34].

Removal of liquid inclusions depend on melt velocity as well as wettability of the liquid inclusions with the filter surface [53]. Accordingly, a high work of adhesion (WA), as defined in Equation (6), is required to separate the liquid inclusions from the filter surface to create new metal-inclusion and metal-filter interface. Equation (6) can further be modified into Equation (7), which shows that maximum inclusions adhesion occurs when the contact angle between filter and inclusion (θ, defined by Equation (8)) is low, i.e., liquid inclusions wets the filter. FeO-MnO-CaO-SiO_2-Al_2O_3 based liquid inclusions showed a contact angle between 5-20°, depending on the specific composition of the inclusions, with zirconia filter at steelmaking temperatures [53]. Filtration efficiency

depends on the wetting of filtration medium [54], and hence, liquid inclusions can be filtered very effectively using the zirconia filters.

$$(WA)_{IF} = \gamma_{MI} + \gamma_{MF} - \gamma_{IF} \tag{6}$$

$$(WA)_{IF} = \gamma_{MI}(1 + cos\theta) \tag{7}$$

$$\theta = cos^{-1}\left(\frac{\gamma_{MF} - \gamma_{IF}}{\gamma_{MI}}\right) \tag{8}$$

2.2. KINETICS OF FILTRATION PROCESS

Removal efficiency (η) of non-metallic inclusions is defined in Equation (9), where C_i and C_o are the inclusion concentrations in the steel melt at the filter inlet and at the outlet respectively [26, 51, 52]. One of the major issues with using a ceramic filter is to prime it properly. At the beginning of pouring, the liquid steel must pass through the filter without solidifying in the filter webs. This can be achieved by supplying enough heat from the incoming metal and designing a proper rigging system to build up sufficient ferrostatic head to overcome the capillarity effects [55].

$$\eta = \left(\frac{C_i - C_o}{C_i}\right) \times 100\% \tag{9}$$

The steel melt flowrate inside the mold cavity influences the inclusion removal efficiency. High melt velocities or flow rates through the filter lower the removal efficiency due to the decreased residence time of the steel inside the filter [28, 33]. Filter pore sizes plays an important role in controlling metal velocity and hence residence time, as shown in Figure 2.3 (a) and (b) [33, 56]. An increase in filter thickness or change in aspect ratio can also increase the residence time of steel melt in the filter [57, 30], which helps to increase the inclusion removal efficiency as represented in Figure 2.3 (c) [57].

The residence time ($t_{residence}$) of the inclusions inside a filter element is given by Equation (10), where T_{filter} is the thickness of the filter element, and V_{steel} is the instantaneous velocity of the steel melt passes through the porous area of that filter element.

$$t_{residence} = \frac{T_{filter}}{V_{steel}} \tag{10}$$

Several studies have been performed to understand the role of ceramic filters on capturing the non-metallic inclusions. The rate determining step of alumina inclusion filtration by a ceramic loop filter, which is effective for high filtration efficiency, is the transport of inclusions from molten steel to filter surface. This transport of inclusions depends on several parameters such as effective turbulent diffusivity in molten steel, radii of alumina inclusions, diameter and total surface area of loop filter string, temperature, volume, velocity and viscosity of molten steel, filter void ratio etc. [32].

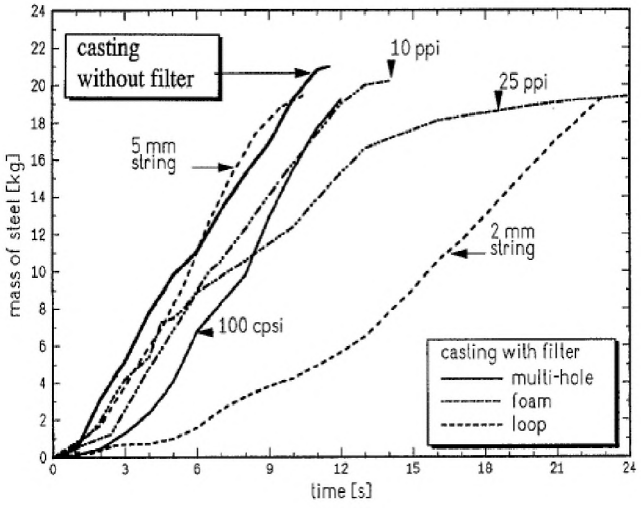

(a)

Figure 2.3. (a) Smaller pore size decreases steel flow rate [33], (b) smaller pore size increases filtration efficiency [56] and (c) thicker filter geometry increases filtration efficiency [57].

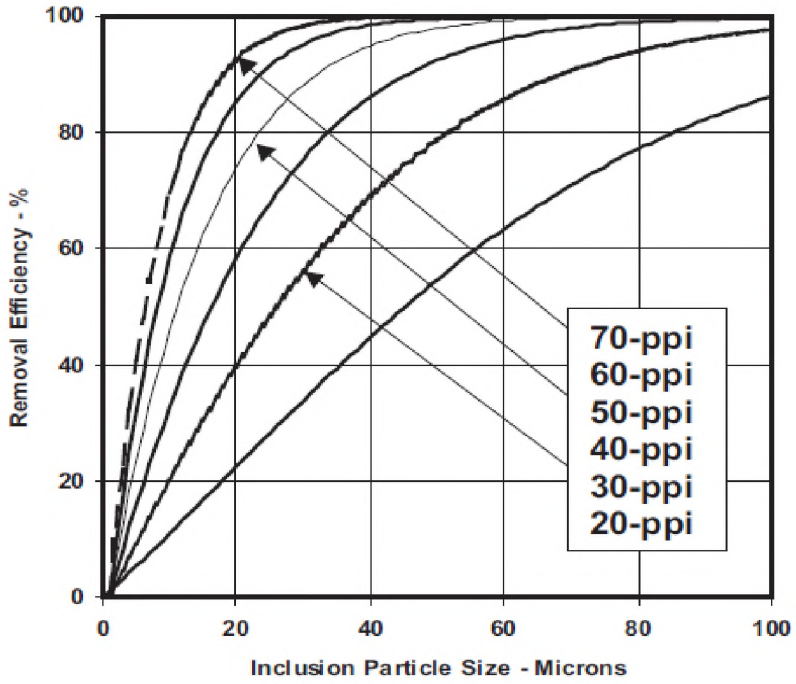

(b)

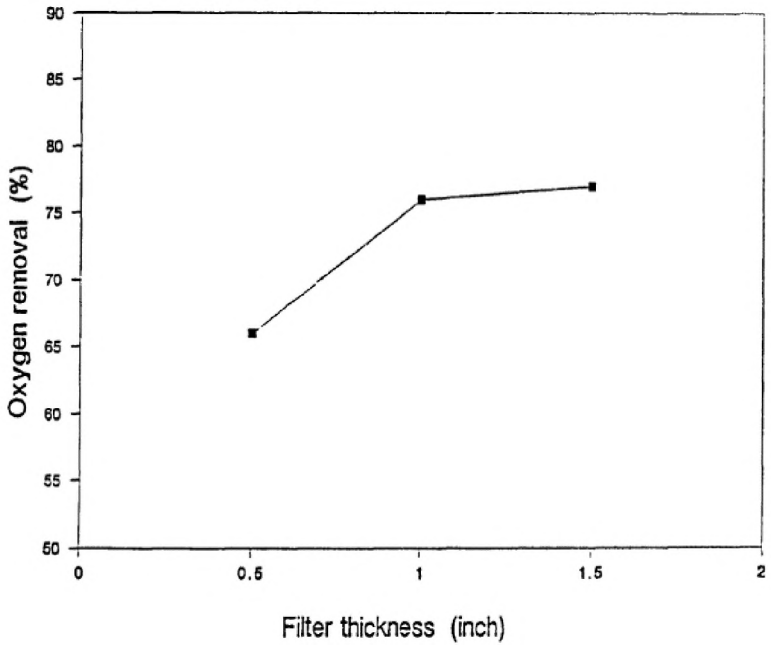

(c)

Figure 2.3. (a) Smaller pore size decreases steel flow rate [33], (b) smaller pore size increases filtration efficiency [56] and (c) thicker filter geometry increases filtration efficiency [57] (cont.).

Figure 2.4 (a) [42] shows that with increase in the fluid velocity across the filter grain, the inclusion having a higher mass inertia deviates from the streamline fluid flow and tends to follow the path shown by the dashed line in Figure 2.4 (b) [42], due to the turbulent motion of the fluid. Hence, the number of inclusions which approach the filter grain also increases in proportion to the velocity, as the fluid velocity increases [42]. The kinetics of inclusion capture by deep bed filtration was reported in a previous literature to follow first order kinetics [42]. Deep bed filtration mechanism is shown in Figure 2.5 [33].

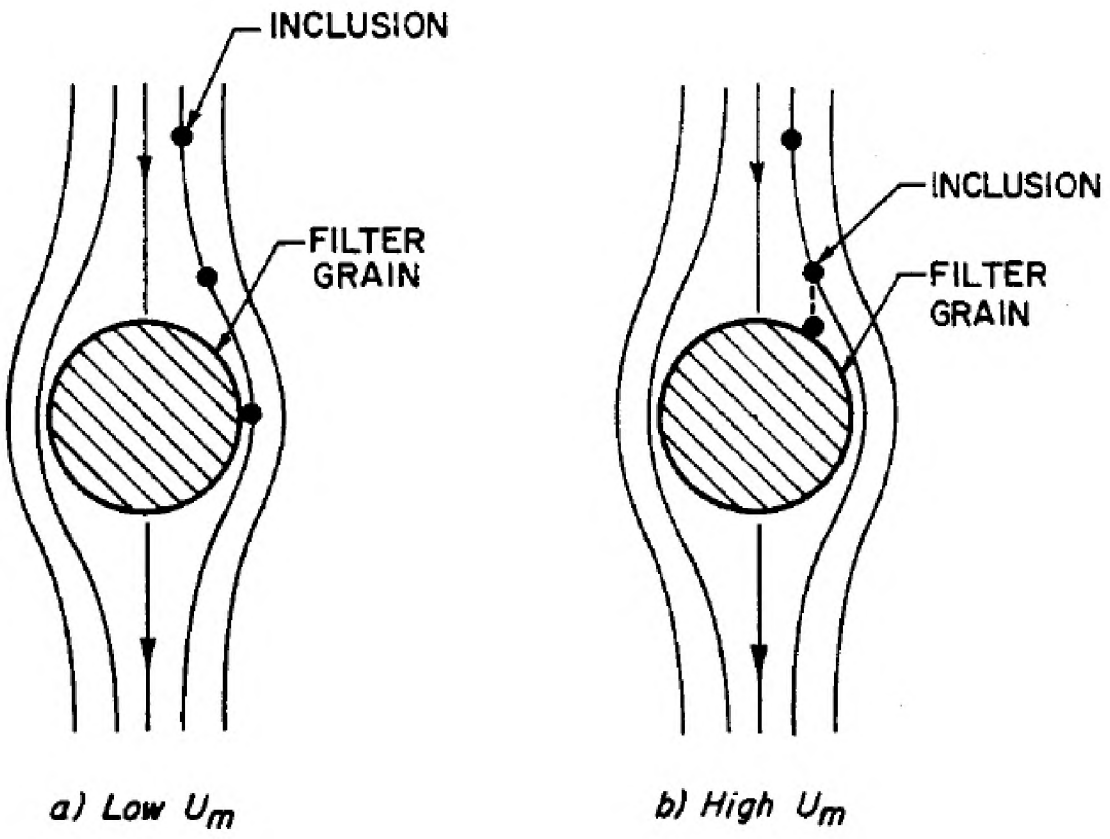

Figure 2.4. Effect of velocity on inclusion trajectory near a spherical filter grain [42].

Change in inclusion concentration through filter thickness can be represented by Equation (11), where C_i and $C(Z)$ are the concentrations of the inclusions at the filter inlet and a distance, Z, from the filter inlet respectively, U_m is the approach velocity of metal and K_0 is a function of the characteristics of the filter, such as pore structure, tortuosity, etc. The change in inclusion concentration strongly depends on the metal approach velocity, as represented in Figure 2.6 [42].

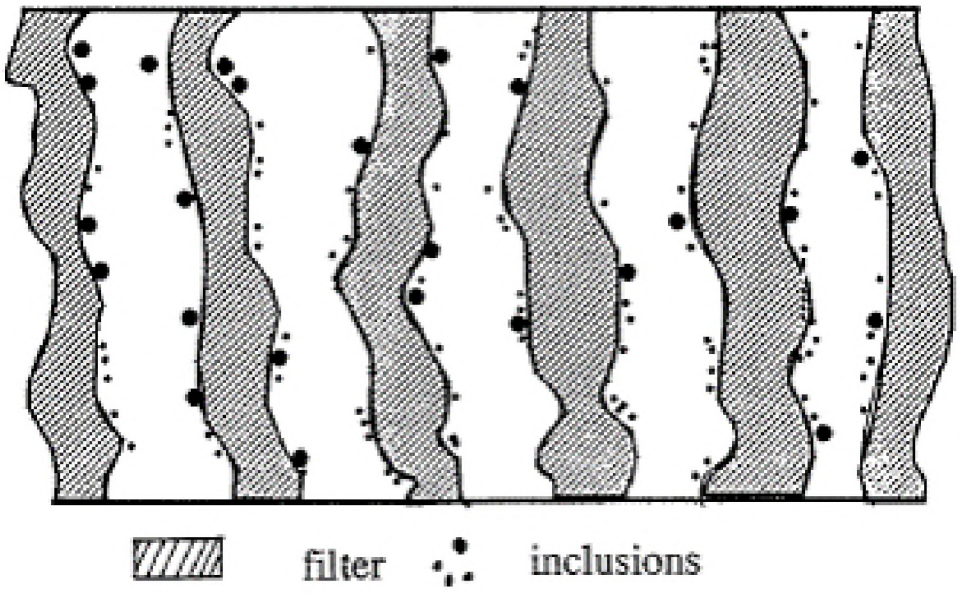

Figure 2.5. Inclusion removal by deep bed filtration mechanism [33].

This kinetic model predicts that the concentration of captured inclusions should decrease exponentially from the entry side to the exit side of the filter element within the body of the filter. The model was established indirectly by finding a linear correlation between U_m^{-1} and $ln(C_o/Ci)$, where Co is the concentration of the inclusions at the filter outlet. However, no direct measurements were carried out in an attempt to verify this

prediction by sectioning the filter and measuring the local concentrations of inclusion within the filter element, possibly due to lack of suitable characterization techniques available at the time of the experiment.

$$\frac{C(Z)}{C_i} = exp(\frac{-K_0 Z}{U_m}) \tag{11}$$

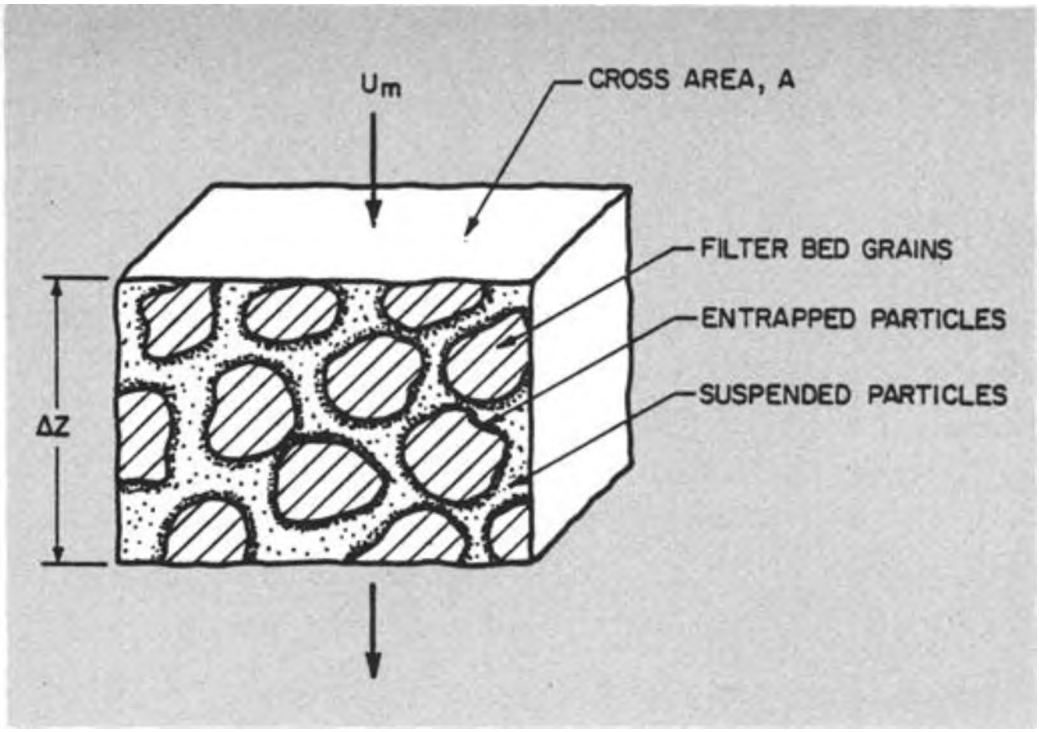

Figure 2.6. Change in inclusion concentration through the filter thickness is strongly depends on metal approach velocity during deep bed filtration [42].

Many researchers have tried to simulate metal flow through a filter [58-65]. Though modeling a turbulent fluid flow through a complex filter geometry is always a challenging task. A simplistic approach to deal with this problem is to consider a flow through porous medium following Darcy's law, which is given in Equation (12). For a Darcy type flow, the flow rate (Q), through a filter thickness L and cross-sectional area

A, is directly proportional to the pressure drop (ΔP). This equation is valid for low pressure and low velocity condition. K is a proportionality constant and it can be further defined as a ratio of specific permeability (k) of the porous medium and the viscosity of the molten steel (μ), as given in Equation (13).

$$Q = \frac{KA\Delta P}{L} \tag{12}$$

$$K = \frac{k}{\mu} \tag{13}$$

Computational fluid dynamics-based simulation software packages are vastly used for simulating molten steel flow and casting. Many researchers used these software packages to simulate fluid flow through filters or solidification process [66-69]. Campbell demonstrated the designing method for various gating systems to optimize the fluid flow and obtain sound castings [70]. Figure 2.7 [66] represents design of a mold for filtration process and Figure 2.8 [66] shows filling simulation of that filtration process using a simulation software [66].

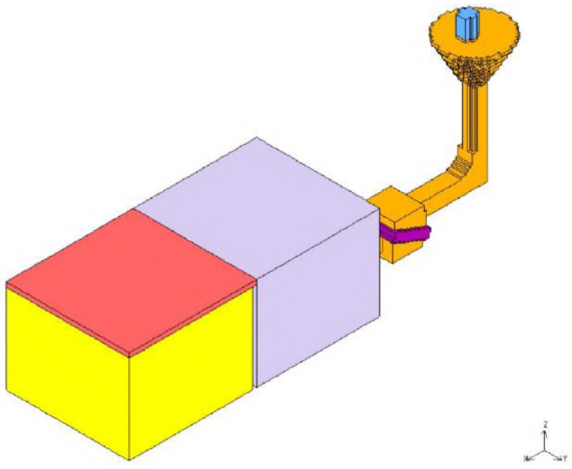

Figure 2.7. Mold design utilized for simulation work [66].

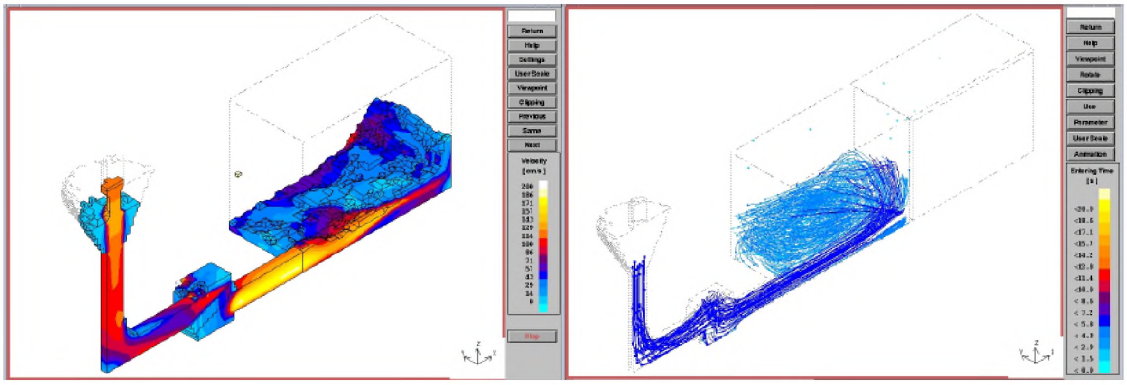

Figure 2.8. Filling simulation of filtration process [66].

PAPER

I. REMOVAL OF ALUMINA INCLUSIONS FROM MOLTEN STEEL BY CERAMIC FOAM FILTRATION

Soumava Chakraborty[1], Ronald J. O'Malley[1], Laura Bartlett[1] and Mingzhi Xu[2]

[1]Peaslee Steel Manufacturing Research Center, Department of Materials Science and Engineering, Missouri University of Science and Technology, Rolla, MO, USA, 65409

[2]Department of Mechanical Engineering, Georgia Southern University, Statesboro, GA, USA, 30460

ABSTRACT

The efficiency of removal of solid alumina inclusions by filtration and the distribution of inclusions captured through the thickness of the filter was investigated for an aluminum killed 316 stainless steel casting. A mold design was developed using modeling software to produce two castings that fill simultaneously, one with a filter and the other without a filter. The design was optimized to produce the filtered casting and unfiltered casting from a single ladle pour, while also matching the fill rates and avoiding turbulence and reoxidation during pouring. Samples from the filters and the castings were analyzed using an SEM with EDS and automated feature analysis to measure the efficiency of inclusion removal for a 10ppi zirconia foam filter. Results showed that inclusion removal efficiency depends strongly on the initial inclusion concentration and that the alumina inclusions are captured within the filter at the filter web-steel interface. This study also documented that inclusion floatation inside the mold cavity plays a role in

reducing the inclusion concentration in the casting. The distribution of alumina inclusions captured through the filter thickness was quantified using elemental mapping and the inclusion distribution was found to decrease exponentially, following first order capture kinetics.

Keywords: steel, non-metallic inclusions, filtration, floatation, removal kinetics, mathematical modeling

1. INTRODUCTION

In foundry steelmaking, ceramic filters are commonly used to remove non-metallic inclusions. Non-metallic inclusions in steel can reduce mechanical properties, impact machinability, produce surface defects and increase scrap rates [1]. Aluminum is a strong deoxidizer and at sufficient levels of addition, generates solid alumina inclusions in the steel melt. The equilibrium reaction of the formation of alumina inclusions in steel melt during deoxidization is shown in Equation (1).

$$2[Al] + 3[O] = (Al_2O_3)_{solid} \quad (1)$$

Several studies have shown that ceramic filters can effectively remove inclusions [2-9] from the steel melt. The melt flowrate inside the mold cavity influences the inclusion removal efficiency. High flow rates [4] or melt velocities [10] through the filter lower the removal efficiency due to the decreased residence time of the steel inside the filter. Filter geometry also plays an important role in inclusion removal. An increase in filter thickness [11] or change in aspect ratio [12] can also increase the residence time of steel melt in the filter, which helps to increase the inclusion removal efficiency. Inclusion

removal efficiency (η) is defined in Equation (2), where C_i and C_o are the inclusion concentrations in the steel melt at the filter inlet and at the outlet respectively.

$$\eta = \left(\frac{C_i - C_o}{C_i}\right) \times 100\% \quad (2)$$

In a previous study [13], the kinetics of inclusion capture by filtration was reported to follow first order kinetics, as represented in Equation (3). C_i and $C(Z)$ are the concentrations of the inclusions at the filter inlet and a distance, Z, from the filter inlet respectively. This kinetic model predicts that the concentration of captured inclusions should decrease exponentially from the entry side to the exit side of the filter element within the body of the filter. However, no direct measurements were carried out in an attempt to verify this prediction by sectioning the filter and measuring the local concentrations of inclusion within the filter element, possibly due to lack of suitable characterization techniques available at the time of the experiment.

$$\frac{C(Z)}{C_i} = exp(\frac{-K_0 Z}{U_m}) \quad (3)$$

The objective of the current study is to evaluate the effectiveness of filtration of solid alumina inclusions from steel by comparing the inclusion area fractions at filter inlet and outlet, comparing the castings produced with and without ceramic foam filter from the same heat, and quantifying the distribution of inclusions captured through the filter thickness.

2. MOLD DESIGN

A model of the experimental mold design was developed using MAGMASOFT® 5.3.1 [14] to simulate fluid flow, heat transfer, and solidification during mold fill for a 316 stainless steel casting. The casting and rigging design are shown in Figure 1. Two modified Y-block castings are shown in a vertically parted no-bake mold: one filtered and the other unfiltered. Both sides of the castings were designed to be filled by a common pouring cup so that the temperature and composition history of liquid steel was comparable for both castings. By characterizing and comparing the samples from both castings, a direct comparison can be made between the filtered and unfiltered castings and the effectiveness of the zirconia filter on inclusion removal can be determined. A dam was placed under the pouring cup to reduce the melt velocity and the potential for air entrainment. Bottom filling was also employed to minimize the reoxidation of the melt.

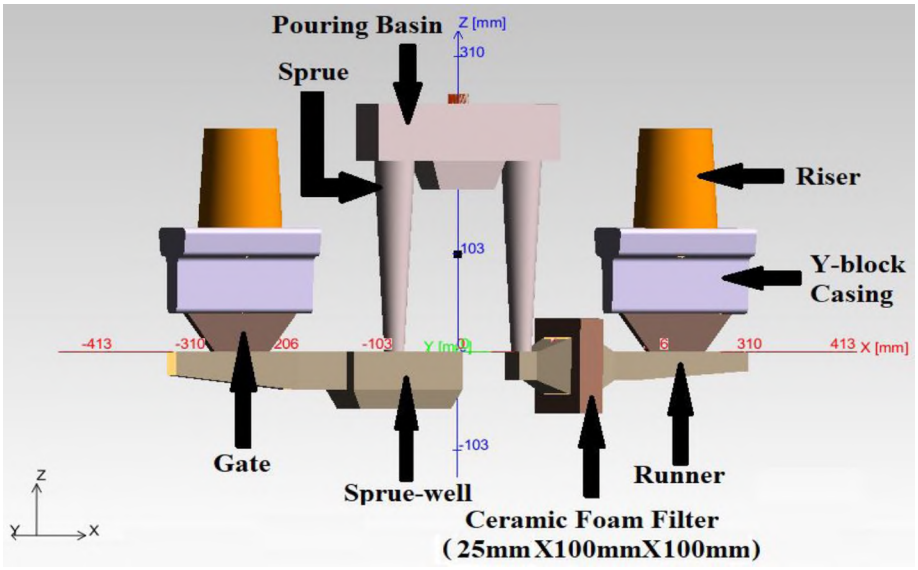

Figure 1. Designing of Y-block castings and the associated rigging systems using CFD software.

The dimension of the mold is 700mm x 200mm x 350mm. To avoid the back pressure during pouring, two separate sprues were fed from a single pouring cup to fill the two castings simultaneously. Sprue diameters were also optimized to minimize air entrainment during mold filling. The dimensions of the sprues, gates, castings and risers on both castings are same, although the runners are different to adjust the liquid metal flow rate and to ensure simultaneous filling of the mold cavities on both sides. Hence, the gating ratios are different for both sides: 1:2:3.8 (with filter) and 1:2.6:3.8 (without filter). This design also helped to minimize vortex formation inside the mold [15, 16]. Pouring temperature and ferrostatic head was optimized during modeling to avoid any premature solidification in the filter.

In a previous study, Raiber et al. [4] showed that multi-hole filters and loop filters can remove large alumina inclusions from steel, but that ceramic foam filters remove these inclusion particles more effectively than multi-hole filters or loop filters. They reported a maximum inclusion removal efficiency of 95% for a 25ppi foam filter in their experiments. Consequently, foam filters were selected for use in this study. However, a 10ppi foam filter was used to avoid excessive filling resistance and allow simultaneous filling of both the filtered and unfiltered castings. The size of the filter was selected to maximize the residence time in the filter to increase the filtration efficiency. Zirconia foam filters (Foseco STELEX ZR^{TM} 10ppi:25mm x 100mm x 100mm) were employed in our experiments, shown in Figure 2.

Filling velocity, time and temperature were predicted for the mold design. The metal flow patterns during filling are different for the two different gating systems (with and without filter) as shown in Figure 3. The side without the filter initially showed a

higher velocity, as no filter was present to restrict the flow of the melt. To compensate for this, a sprue-well was added to the side without the filter as shown in Figure 1. In this design, mold filling was modeled by a 20mm diameter metal stream from a height of 50mm using a teapot-style ladle, which is representative of the experimental conditions in this study. The filling simulation showed that the mold cavity filled at a rate of 2.5kg/s in 10.3s.

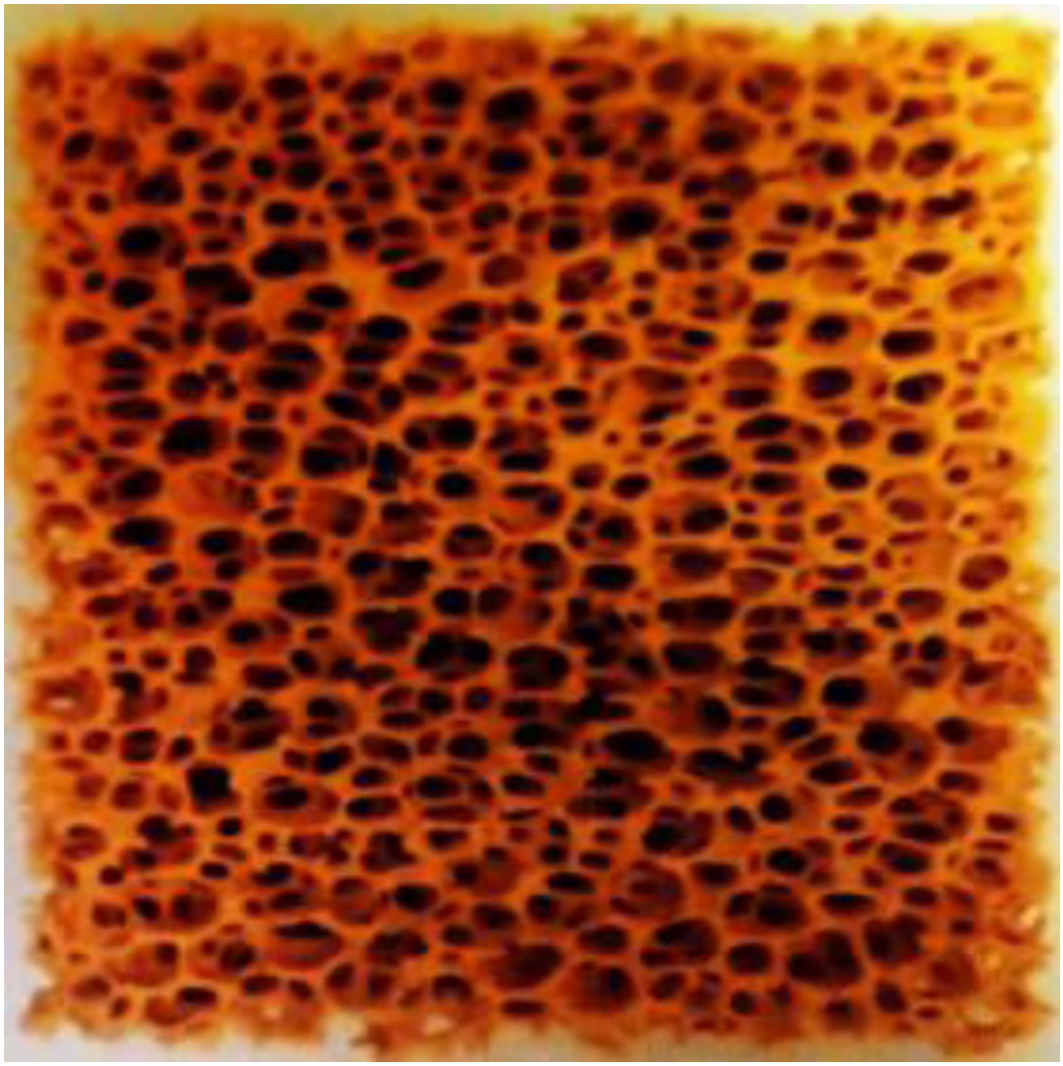

Figure 2. Magnesia-stabilized zirconia 10ppi foam filter (25mm x 100mm x 100mm) used in the experiment.

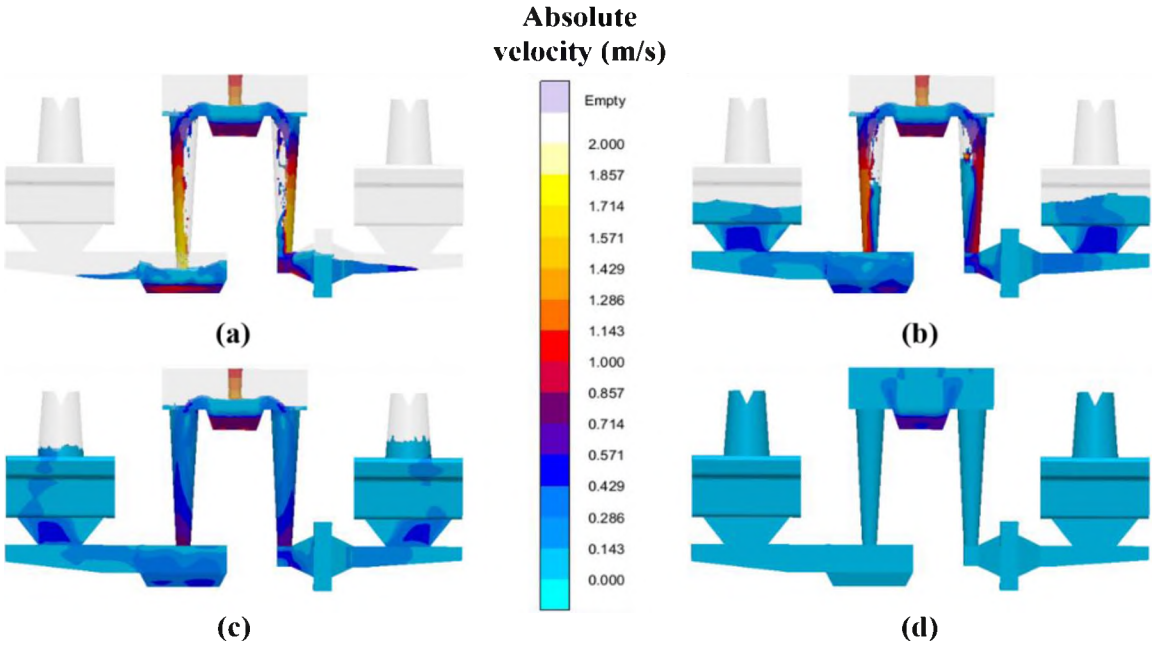

Figure 3. Absolute velocities of the steel melt at: (a) 25% (b) 50% (c) 75% and (d) 100% filling of mold.

The recommended maximum velocity of steel melt to minimize surface turbulence is less than 0.45m/s [17]. For most of the pouring time, as shown in Figure 3, the velocity in the runner is less than 0.45m/s. At the gate, the liquid metal changes its direction and due to a discontinuity in metal flow, the velocity increases slightly above the critical range. In the casting, the absolute velocity decreases further and is less than 0.45m/s at all times during the fill. The metal entering the runner has a lower velocity than in the sprue. Decreasing the velocity inside the mold cavity decreases the turbulence created by the liquid metal during filling which in turn decreases reoxidation of the melt [18, 19]. Thus, air entrapment during mold filling was minimized and is represented in Figure 4.

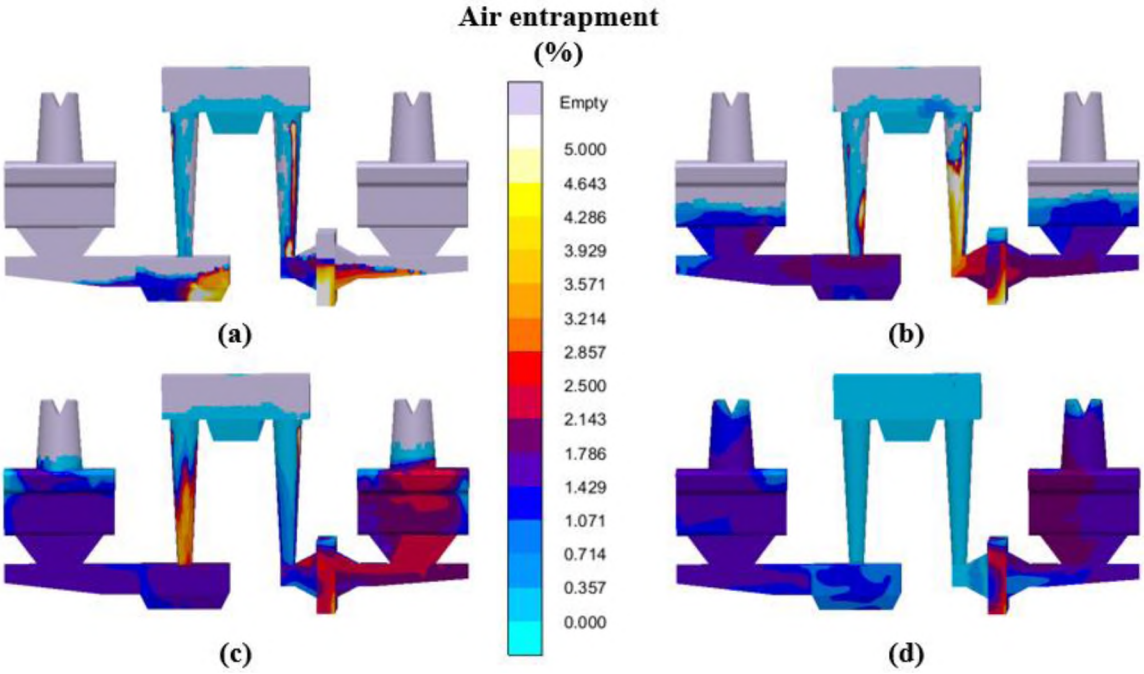

Figure 4. Air entrapment of the steel melt at: (a) 25% (b) 50% (c) 75% and (d) 100% filling of mold.

Lowering the pouring rate or increasing the pouring time to greater than 10.3s gives lower velocities inside the mold cavity. However, longer filling time can also cause air entrainment into the liquid metal stream during pouring, which would interfere with the experimental objectives. Slow filling can also create a temperature drop and premature solidification inside the mold cavity before completion of filling. This may result in cold shuts or misruns. Therefore, for experimental studies, these two opposing factors were considered, and the pouring time was maintained below 15s while filling velocities were held below the critical value of 0.45m/s to avoid any premature solidification. Rigging systems from both sides were designed to balance the metal flow rate during the filling and to ensure that steel from the ladle reaches and fills both Y-blocks simultaneously. To match the filling times, the gating ratio on the side without the

filter was adjusted to balance the filling velocities. The mold fill simulation results were also confirmed by direct observation during pouring. Tracer particle tracking by the modeling software predicts that minimal vortexing is generated in the mold during filling, as represented in Figure 5.

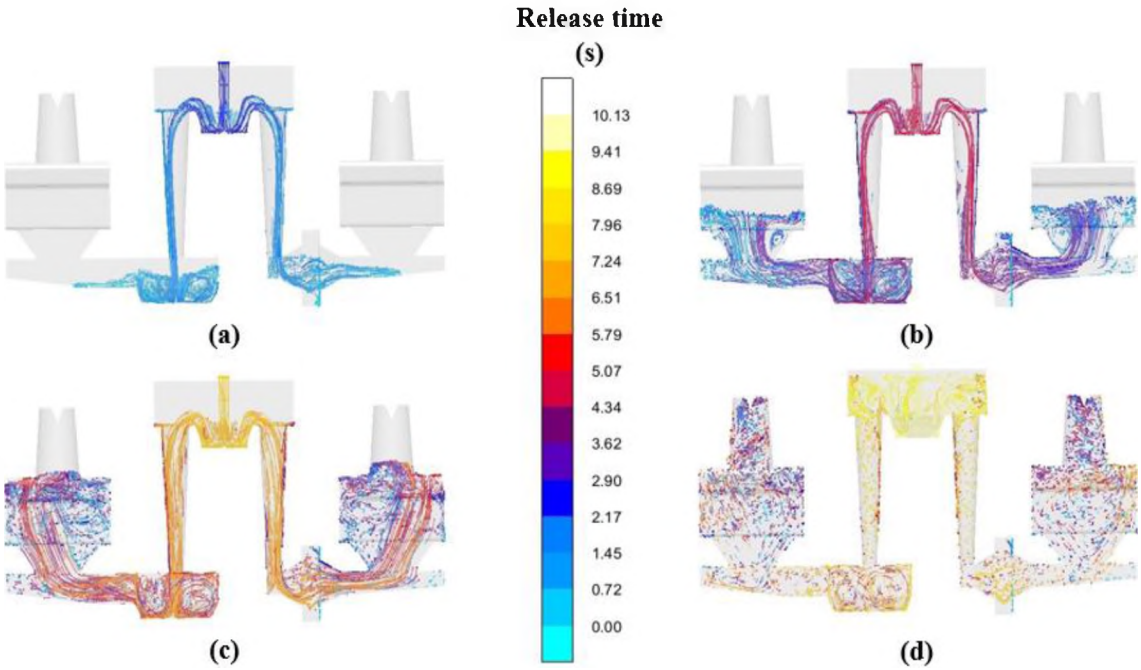

Figure 5. Release time tracer results of the steel melt at: (a) 25% (b) 50% (c) 75% and (d) 100% filling of mold.

The early liquid with higher temperature fills the castings. The pouring temperature was set to 1550°C and the temperature during filling has also been modeled as shown in Figure 6. The minimum steel temperature predicted is 1456°C at the end of filling which is higher than the liquidus temperature of 316 stainless steel, 1407°C, depending on the specific composition of the steel. Liquidus temperature of the 316

stainless steel was calculated using FactSage^{TM} 7.2 [20]. Therefore, no premature solidification was predicted.

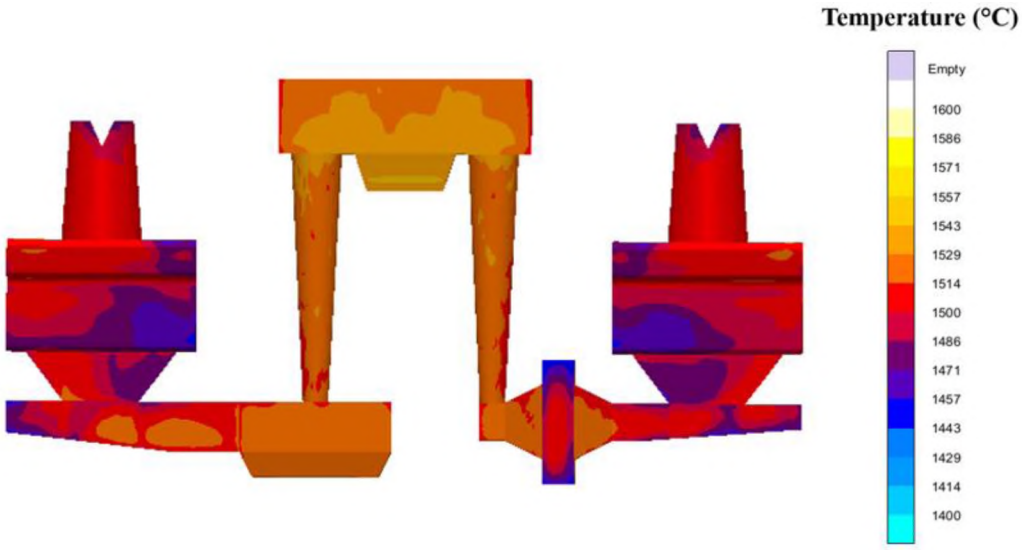

Figure 6. Filling temperature at the end of filling is higher than the liquidus temperature of the steel composition.

Solidification parameters were also evaluated by the modeling software to ensure that both the castings were sound. The castings were predicted to be having Niyama criterion >3.0(°C.s)$^{0.5}$/mm and microporosity <0.1%, as shown in Figure 7, which are the criteria for sound castings [21-24].

3. EXPERIMENTAL PROCEDURE

Three molds were prepared from a 3D-printed pattern as shown in Figure 8 (a). The patterns for the design were printed with an acrylonitrile butadiene styrene polymer.

All the parts were finish sanded with emery paper and glued into the mold box. To fit the risers into the mold cavity, cylindrical cores were added. Before molding, the mold box along with the 3D-printed parts are coated with a release agent, ZIP-SLIP® LP 78 and then allowed to dry for 24 hours. Using these patterns, no-bake sand molds were constructed to carry out the experiments as shown in Figure 8 (b).

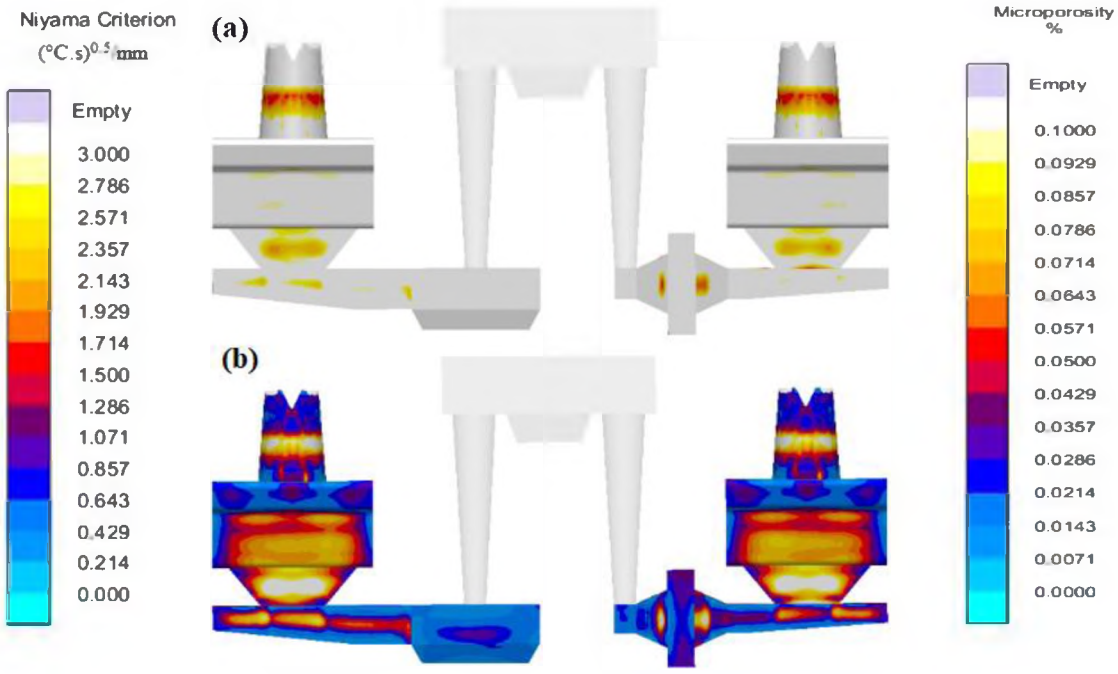

Figure 7. (a) Niyama criterion showed a value >3.0 for both castings and (b) microporosity levels showed <0.1% for both the castings.

MORCO MAG RAM 98 DV was used for furnace relining and MORCORAM 99D was used for ladle relining. Both were purchased from Missouri Refractories Company, Inc. Steel heats were prepared in a 200lb (~90kg) coreless induction furnace under argon cover. Figure 9 (a) shows a photograph of the induction furnace and three vertically parted molds prior to casting. 80kg of 316 stainless steel charge stock was

induction melted under a continuous argon gas flow ($1.18X10^5 mm^3/s$). At 1548°C, a chemistry sample was taken. At 1644°C the steel melt was tapped into a preheated teapot-style ladle as shown in Figure 9 (b). Aluminum was used as the deoxidizer (0.1wt% of the melt) to form solid alumina inclusions. The deoxidizer was added to the tap stream from furnace to submerge the addition into the ladle and the melt was then stirred vigorously with a steel rod. After the addition of deoxidizer, a chemistry sample was taken from the ladle before pouring into molds. Finally, the molten metal was poured from the ladle into three molds at 1554°C. All three molds were filled from a single teapot-style ladle. Consequently, the metal from the bottom of the ladle filled the first mold, melt from the middle of the ladle filled up the second mold, and melt from the top part of the ladle filled the third mold.

4. SAMPLE PREPARATION

Chemical analysis of the samples taken during experiments was carried out using optical emission arc spectroscopy (FOUNDRY MASTER-OXFORD INSTRUMENTS) and LECO combustion methods (CS 600 and TC 500). To characterize the inclusion area fractions, samples were taken from different positions in the casting assembly as shown in Figure 10 (a). A scanning electron microscope (ASPEX PICA 1020) with energy dispersive X-Ray spectroscopy, and automated feature analysis (AFA) was utilized to characterize the composition, size, and distribution of inclusions. Samples were sectioned to be equidistant from the surfaces at the entry and exit sides of the filter (10mm from the filter surfaces) and identified as 'inlet' and 'outlet' respectively, as represented in Figure

10 (b). The inclusion area fractions measured by AFA at these two surfaces were utilized to calculate the filtration efficiency (η) by using Equation (4), where A_i and A_o are the inclusion area fractions at filter inlet and outlet respectively.

$$\eta = \left(\frac{A_i - A_o}{A_i}\right) \times 100\% \quad (4)$$

(a)

(b)

Figure 8. (a) 3D-printed patterns in a wooden flask and (b) corresponding half of a vertically parted no-bake sand mold.

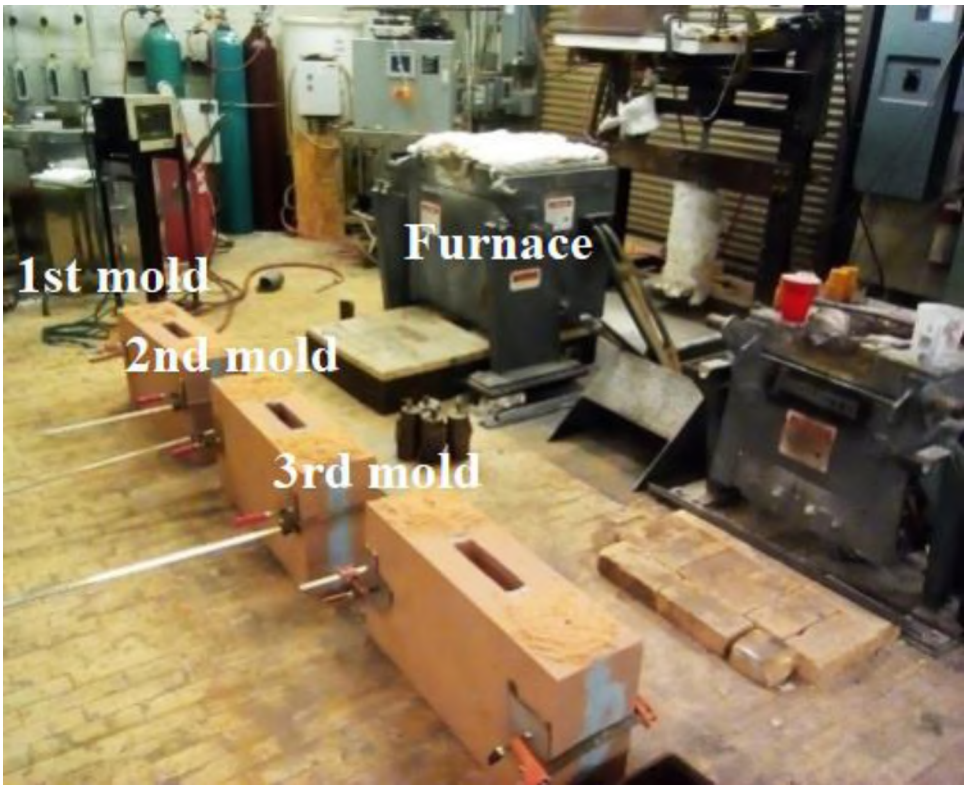

(a)

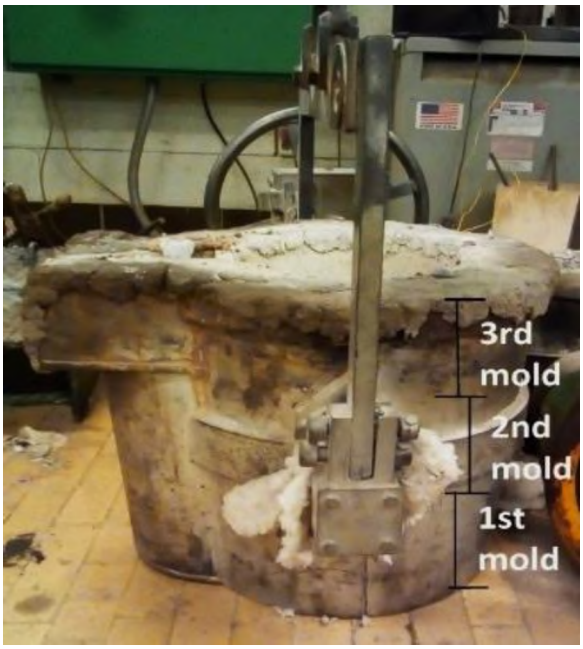

(b)

Figure 9. (a) Three mold sets with induction furnace and (b) teapot style ladle used in the experiment.

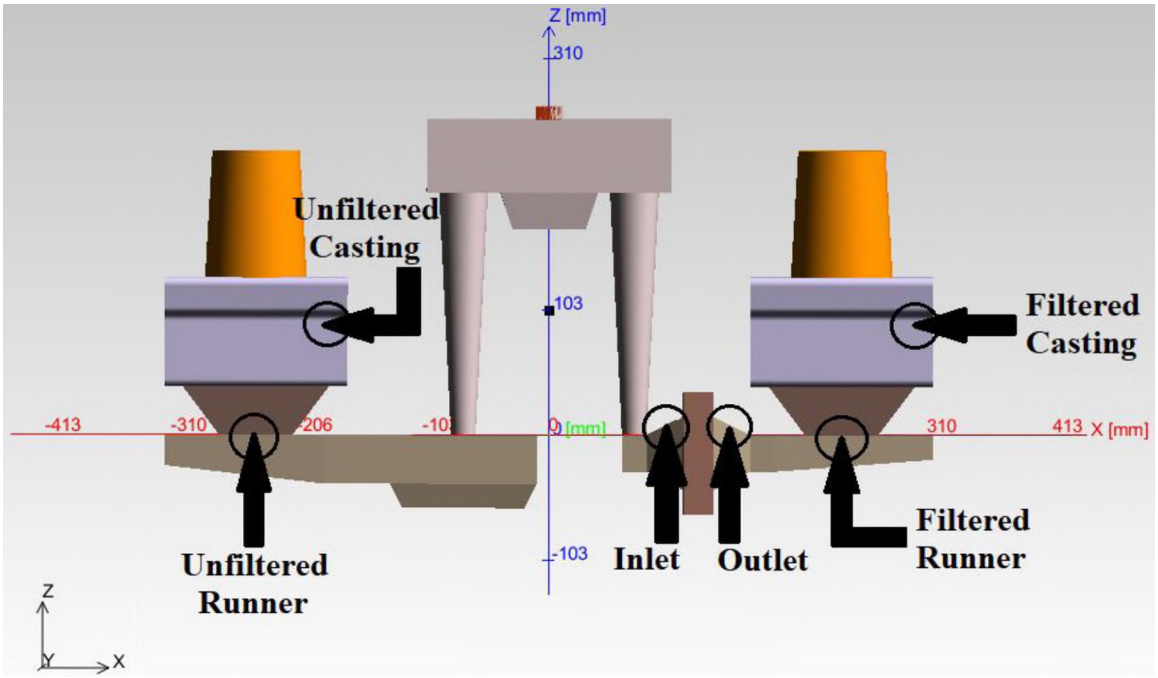

(a)

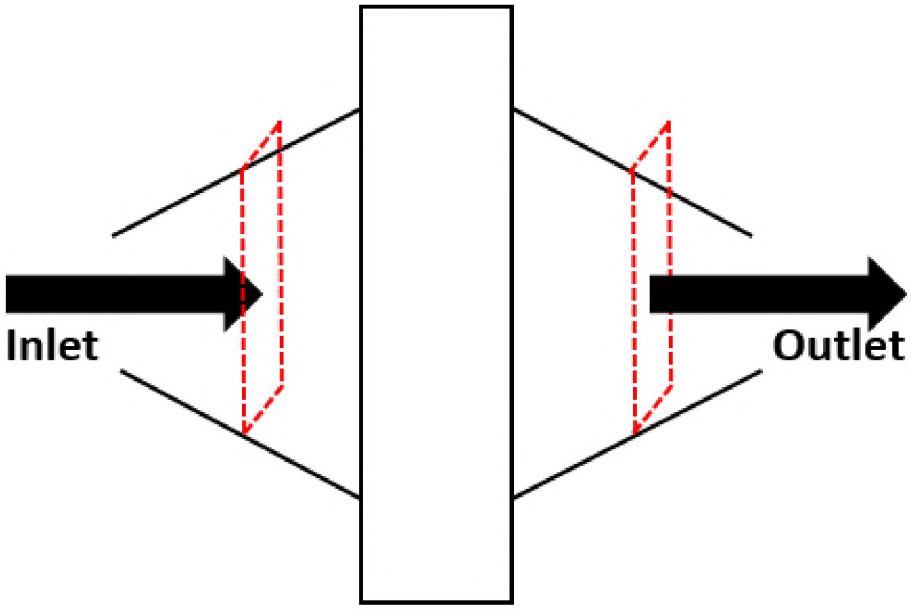

(b)

Figure 10. (a) Sampling positions for automated feature analysis of inclusions and (b) filtration efficiencies of three molds were calculated from the surfaces at filter inlet and outlet.

Two samples were also sectioned from the upper part of modified Y-blocks, identified as 'filtered casting' and 'unfiltered casting'. The decrease in inclusion area fractions in the castings can be determined by comparing these two samples. From the two runners, another two samples were prepared and identified as 'filtered runner' and 'unfiltered runner'. The effect of inclusion floatation inside the mold cavity was also determined by comparing the samples taken from the runners and the castings. Metallographic specimens were prepared by sectioning and polishing epoxy impregnated specimens utilizing standard metallographic preparation techniques. For each sample, automated feature analysis was carried out at two different magnifications (500X and 1000X) and these two data sets were combined to more accurately measure a wider inclusion size distribution (0.5-30.0μm).

Selected scanning area for each sample was ~120mm^2, which is considered as a large sample size for inclusion analysis. A completely randomized statistical method, in-built in the SEM/EDS (ASPEX PICA 1020) software, was utilized for all the sample analyses for both 500X and 1000X magnifications. A large and very significant number of inclusions were scanned from the selected area (~2000 particles on average for 500X magnification and ~6000 particles on average for 1000X magnification) for all the samples. The size distribution analyses, and other calculations were performed based on these statistical measurements. Hence, the data were obtained from statistical measurement of inclusion area fractions from the whole sample, and not an average value obtained from some small areas only. No error bars were therefore included.

Samples were directly prepared from all three filters. To investigate the distribution of the captured inclusions through the filter thickness, the central area of each

filter (area marked in red) was sectioned as shown in Figure 11 (a) and epoxy impregnated under vacuum to avoid air bubble formation, to penetrate any pores in the sample and to preserve any deposits on the filter. After impregnation and curing, these samples were again cut into five pieces (~5mm wide) using a diamond sectioning blade. The filter samples (S1-5) were then re-mounted in epoxy and polished. Each specimen was coated with Au/Pd for SEM analysis. Elemental maps of the metal-filter interface regions were generated at 10 separate randomly selected locations at 1000X magnification for each sample using the energy dispersive X-ray analysis as represented in Figure 11 (b).

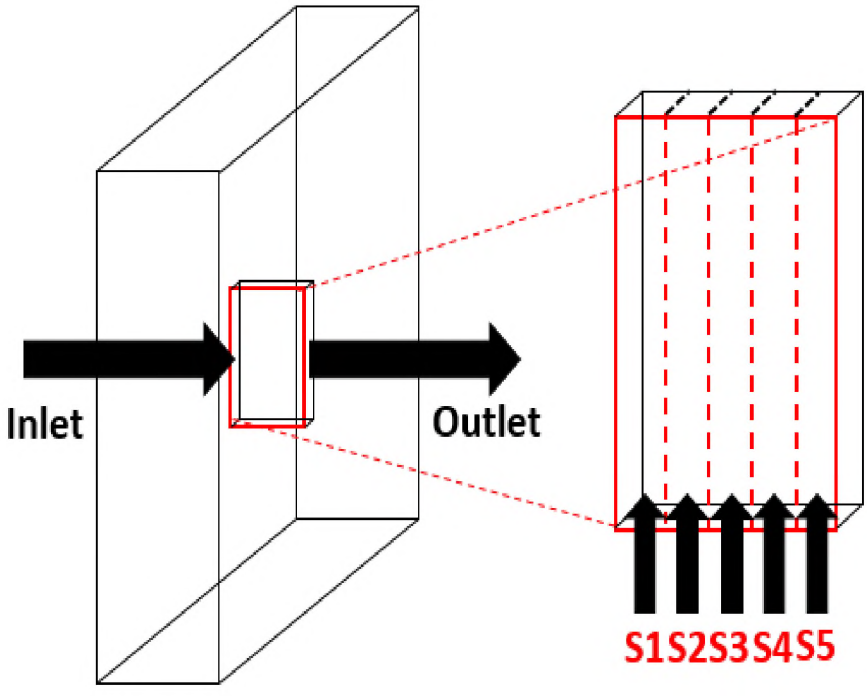

(a)

Figure 11. (a) Samples prepared directly from the filter to investigate the distribution of captured inclusion through the filter thickness and (b) characterization method for EDS mapping to investigate amount of captured inclusions by ceramic foam filter.

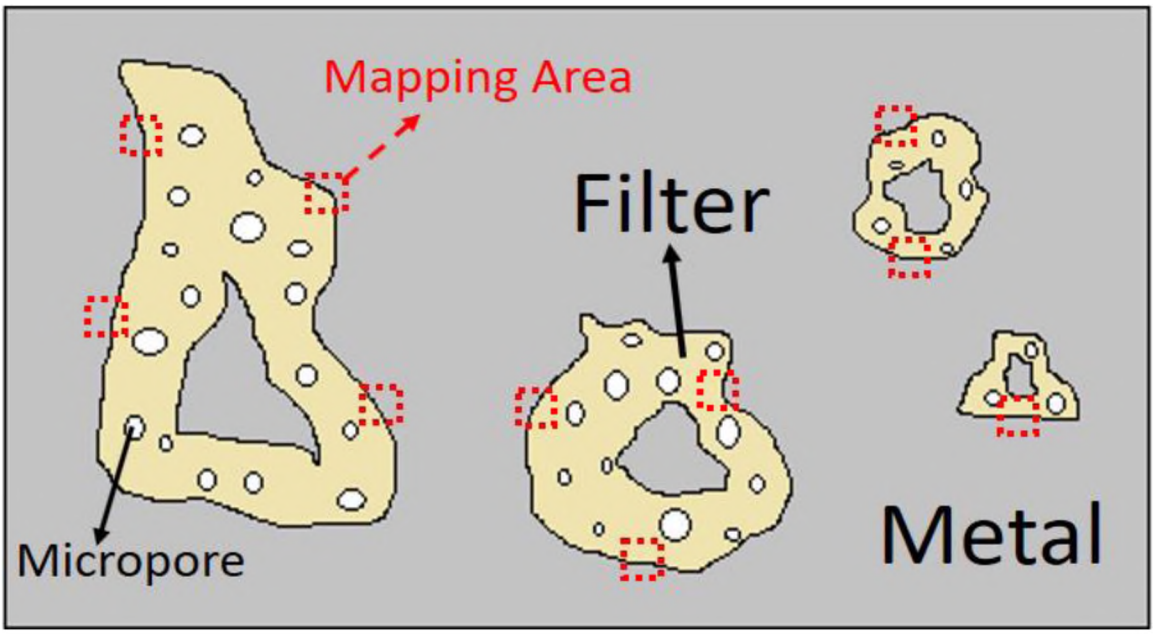

(b)

Figure 11. (a) Samples prepared directly from the filter to investigate the distribution of captured inclusion through the filter thickness and (b) characterization method for EDS mapping to investigate amount of captured inclusions by ceramic foam filter (cont.).

5. RESULTS

Filling time of the molds were 13s each for mold 1 and mold 2, whereas 15s for mold 3. Therefore, the actual filling velocity was even less than the estimated filling velocity from CFD simulation. This difference from the simulated filling time (10.3s) is due to the variable metal stream diameter during manually controlled pouring. Further temperature profile calculations with these actual mold filling conditions did not show any chance of premature solidification inside the mold cavity. Both filtered and unfiltered castings from three different mold sets were examined and found to be free of blow-holes, pin-holes, surface cracks, misruns or cold shuts. No differences were observed

during visual inspection. The chemistries of the melt before and after deoxidation are shown in Table 1. It can be the observed that aluminum content in the ladle is increased by ~0.1% due to the addition of Al deoxidizer to the melt.

Table 1. Melt composition before and after Al addition.

Sampling sequences	C	Si	Mn	Al	Cr	Ni	Mo	Cu	Ti	N	S	O	Fe
Before deoxidization	0.063	1.37	0.51	0.013	18.57	9.03	2.47	0.24	0.012	0.063	0.0039	0.0354	Bal.
After deoxidization	0.084	1.40	0.52	0.120	18.67	9.00	2.47	0.23	0.014	0.085	0.0044	0.0188	Bal.

The area fraction of the inclusion population was measured by SEM-AFA analysis for the six samples prepared from different positions in each casting assembly along with the chemistry, position, and size of the inclusions. Alumina (Al_2O_3), manganese sulfide (MnS) and complex inclusions (mainly MnS that heterogeneously precipitated on preexisting Al_2O_3) were the primary inclusions observed, as shown in Figure 12. A representative joint ternary diagram for the sample at filter inlet of mold 1 shows the chemistry and size distribution of the types of inclusions typically observed.

It should be noted that the manganese sulfide inclusions observed here were formed during solidification and are not actually present in the liquid steel during mold filling and therefore are not relevant to this study. Some MnS inclusions were associated with alumina inclusions, forming complex inclusions which might interfere with the statistical analysis of the oxide inclusions of interest in the melt. A composition threshold of Al>90%, S<10% and Si<10% was applied to each inclusion to consider only the alumina inclusions of interest. Using this method of inclusion classification, the area

fraction of alumina inclusions (in ppm) was calculated for each sample. These results are presented in Figure 13 (a). Total oxygen contents estimated by LECO combustion method at filter inlets and outlets showed a similar trend with the area fractions of alumina inclusions for the same positions as shown in Figure 13 (b).

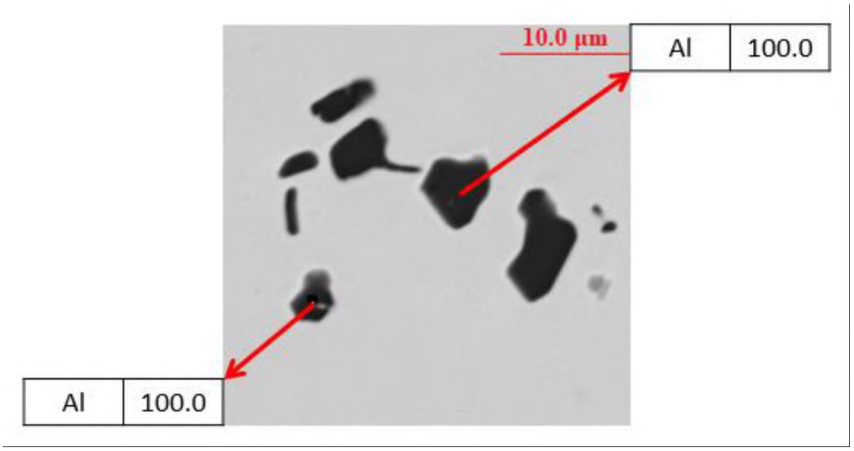

(a)

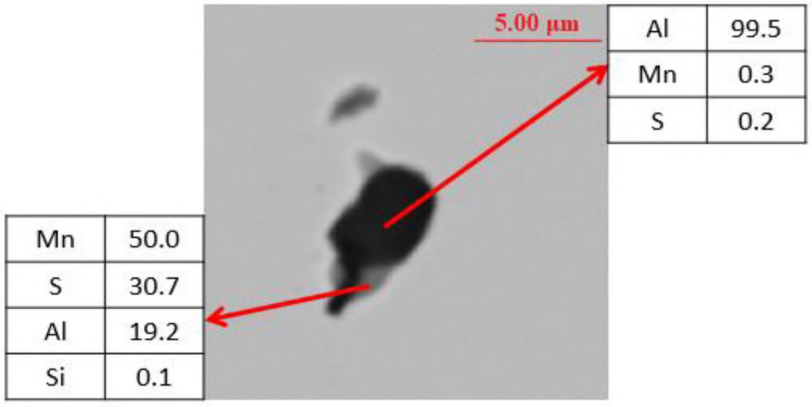

(b)

Figure 12. (a) Alumina cluster and (b) manganese sulfide heterogeneously precipitated on alumina (complex inclusions) observed by backscattered electron imaging during the analysis, and (c) joint ternary diagram of the inclusions observed at filter inlet of mold 3 indicates the formation of alumina, manganese sulfide and complex inclusions.

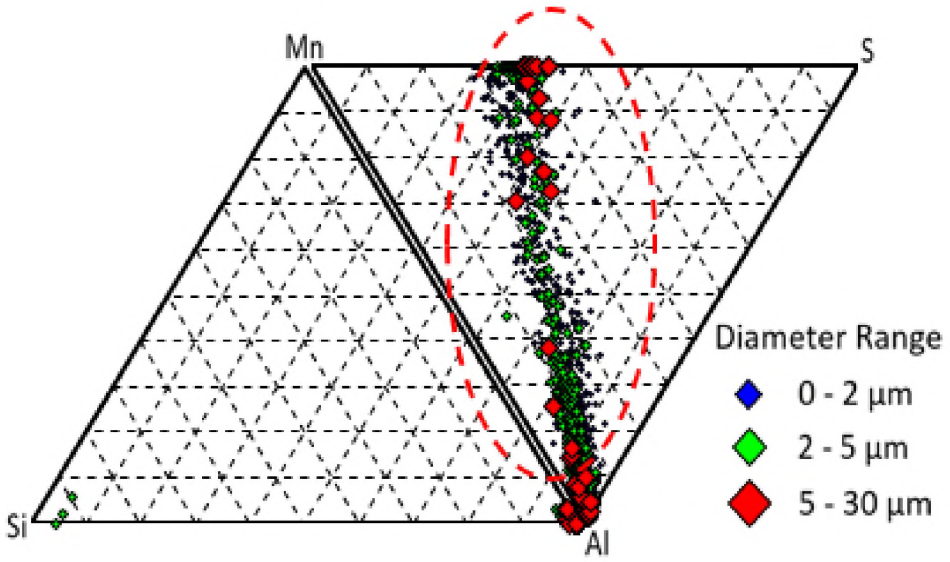

(c)

Figure 12. (a) Alumina cluster and (b) manganese sulfide heterogeneously precipitated on alumina (complex inclusions) observed by backscattered electron imaging during the analysis, and (c) joint ternary diagram of the inclusions observed at filter inlet of mold 3 indicates the formation of alumina, manganese sulfide and complex inclusions (cont.).

Filtration efficiency was calculated comparing inclusion area fractions from filter inlet to outlet. In both sides, the geometries of the rigging systems are not the same and hence it was not expected to see the same filtration efficiency if the inclusion area fractions of unfiltered and filtered castings were considered. Rigging systems from both sides were designed to balance the metal flow rate during the filling and to ensure that steel from the ladle reaches and fills both Y-blocks simultaneously. Otherwise, vortex formation due to unsymmetrical filling was unavoidable. The purpose of comparing the filtered casting to unfiltered casting was only to verify any reduction of inclusion area fractions before performing Charpy V-notch impact testing, which is not included in the current study.

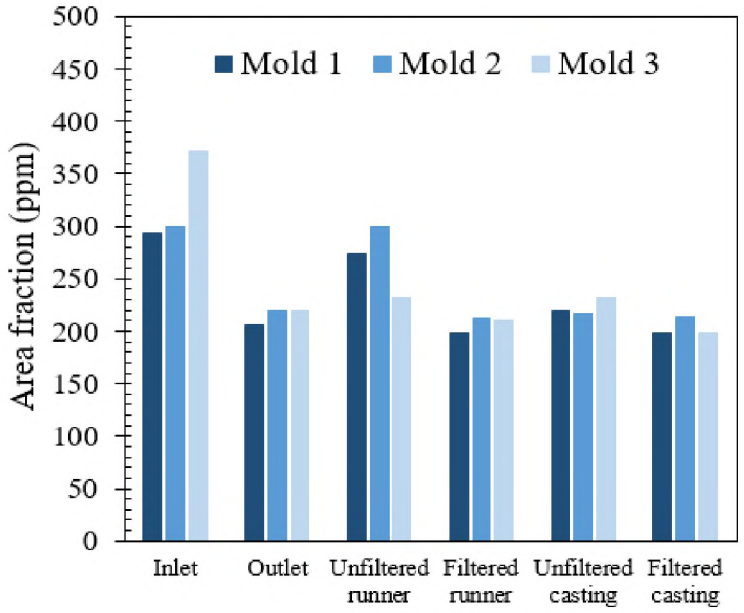

(a)

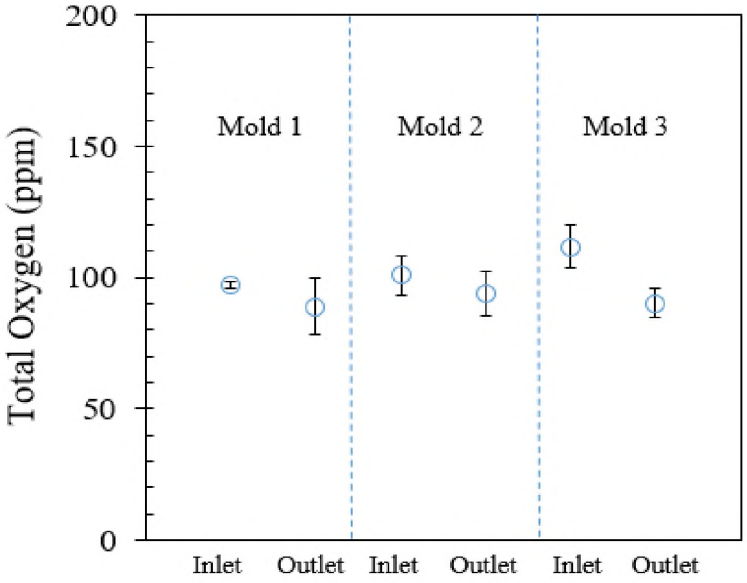

(b)

Figure 13. (a) Area fraction of the alumina inclusions for all the six samples prepared from the castings for all three molds and (b) total oxygen contents of inlet and outlet positions of the filters for all three molds.

In deep bed filtration, alumina inclusions are expected to be captured on the surfaces of the internal filter web structure of the filter and distribute through the filter interior. As expected, the alumina inclusion deposits observed in this study were present at the metal-filter interface and distributed throughout the filter interior. To determine the distribution of the captured inclusions through the filter thickness, the sectioned filter samples were analyzed at five locations from the entry to exit side of all three filters as shown in Figure 11. Elemental maps were created as shown in Figure 14 to quantify the amount of alumina deposited on the filter web surface, using the area fraction of Al and the filter interface cord length. The average thickness of the alumina inclusion build-up (T) at the interface was calculated from these measurements using Equation (5).

$$T = \frac{A_{inclusions}}{l_{interface}} \tag{5}$$

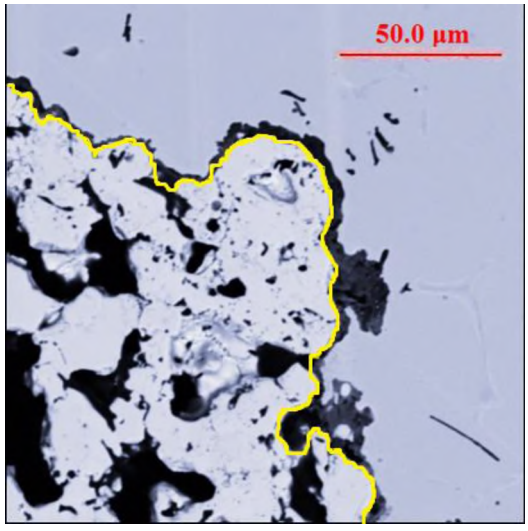

(a)

Figure 14. (a) Measurement of metal-filter interfacial chord length (marked in yellow), (b) elemental mapping showed the presence of alumina inclusions at the interface and (c) area calculation of alumina inclusions at the metal-filter interface using ImageJ thresholding.

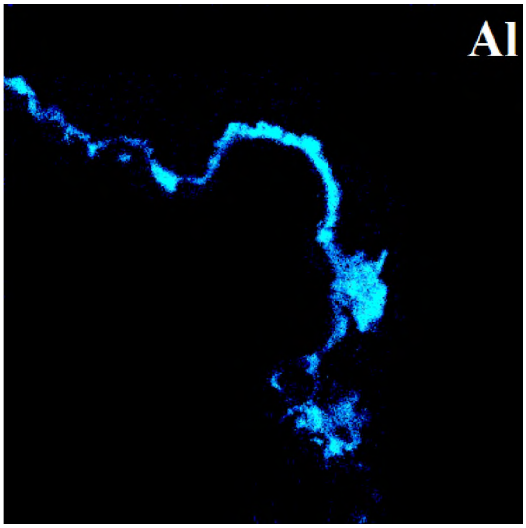

(b)

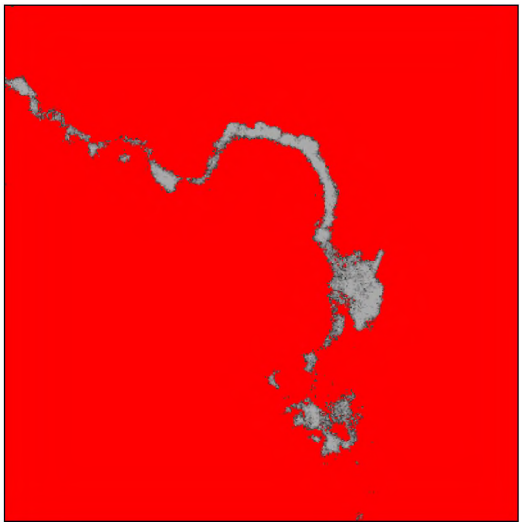

(c)

Figure 14. (a) Measurement of metal-filter interfacial chord length (marked in yellow), (b) elemental mapping showed the presence of alumina inclusions at the interface and (c) area calculation of alumina inclusions at the metal-filter interface using ImageJ thresholding (cont.).

The distribution of the inclusion build-up through the filter thickness is plotted for all the three mold sets in Figure 15. In all cases, inclusions were more likely to be

captured in the entry side of the filter interior (S1) and the inclusion capture decreased exponentially from the entry to the exit side of the filter. This trend was observed for all three filters sectioned from three different molds. The entry side deposit thickness was obseved to be thickest for the third mold and thinnest for the first mold. These results indicate that the incoming steel melt with the highest inclusion content, mold 3, Figure 13, had the highest inclusion capture efficiency.

6. DISCUSSION

Comparing all the six samples sectioned from the castings for the three mold sets, it can be observed that solid alumina inclusions can be removed effectively by filtration, as shown in Figure 13. It can also be observed that the incoming steel (filter inlet) contained a greater number of alumina inclusions compared to the samples collected from the filter outlet. The area fraction for inlet sample of third mold showed the highest value (371ppm) followed by second mold (299ppm) and first mold (293ppm). This is to be expected, as the third mold was poured with the molten steel exposed to atmosphere for a longer time than the first mold. The second mold also showed a slightly higher amount of incoming inclusions than the first mold. From Figure 16 (a) it can also be shown that the short time between successive ladle pours provided little chance of inclusion floatation in the ladle for the inclusions sizes in this experiment. Size distributions of alumina inclusions at filter inlet for all mold sets are plotted in Figure 16 (b).

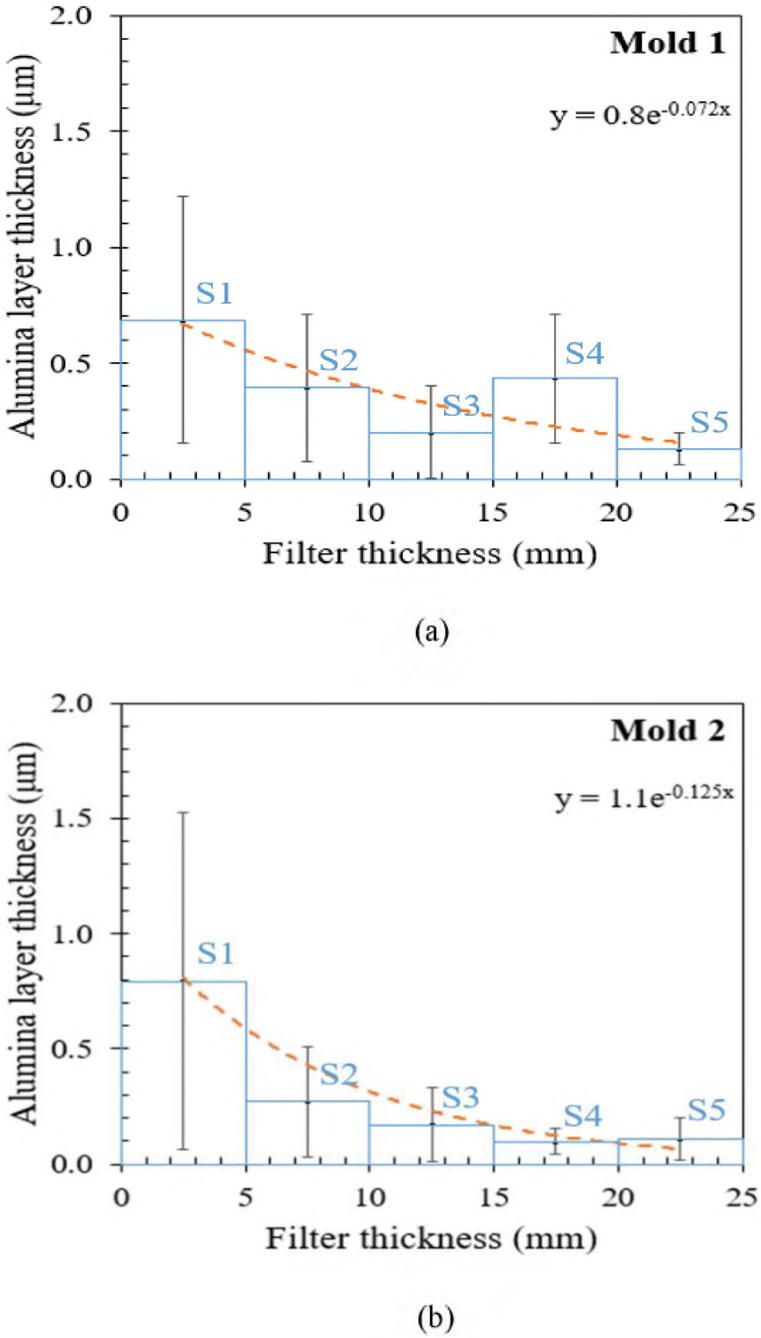

Figure 15. Distributions of captured alumina layer through the filter thickness for (a) mold 1, (b) mold 2 and (c) mold 3.

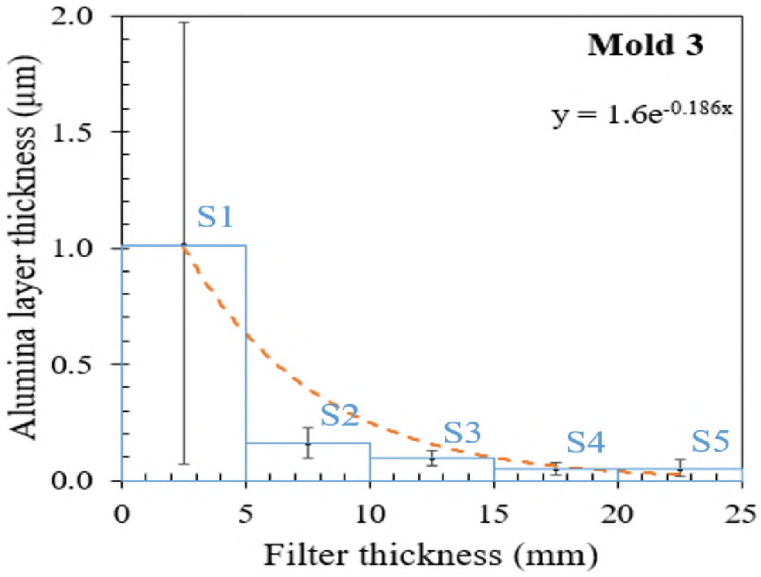

(c)

Figure 15. Distributions of captured alumina layer through the filter thickness for (a) mold 1, (b) mold 2 and (c) mold 3 (cont.).

The size distribution of alumina inclusions at filter inlet and outlet are shown in Figure 17 for the three molds that were cast. Inclusions of all size ranges were observed to be removed by filtration process.

Comparing the area fractions of filter inlet and outlet for all three molds (Figure 18(a)), it can be seen that for mold 3, the inclusion removal efficiency by filtration is 41%, whereas for mold 1 and mold 2, the filtration efficiencies were lower (30% and 26% respectively). The filtration efficiency improves with increased incoming inclusion content, due to the higher probability of capturing these inclusions by the filter. Also, it appears that the top of the ladle contains a higher concentration of slightly larger alumina inclusions (Figure 16), which are expected to have a better chance of being captured by the filter and removed. The filtration efficiency numbers reported in this study are

somewhat lower than the 68% efficiency reported in a previous study by Raiber et. al. [4]. However, Raiber calculated the efficiency using measurements of total oxygen content. Differences in mold setup, orientation of the filter, composition of the filter, alloy composition, sampling location and the initial inclusion concentration may also explain the differences in observed filtration efficiency. Inclusions area fractions between filtered casting and unfiltered casting samples were compared and the third mold showed maximum inclusion removal efficiency as well (Figure 18(b)).

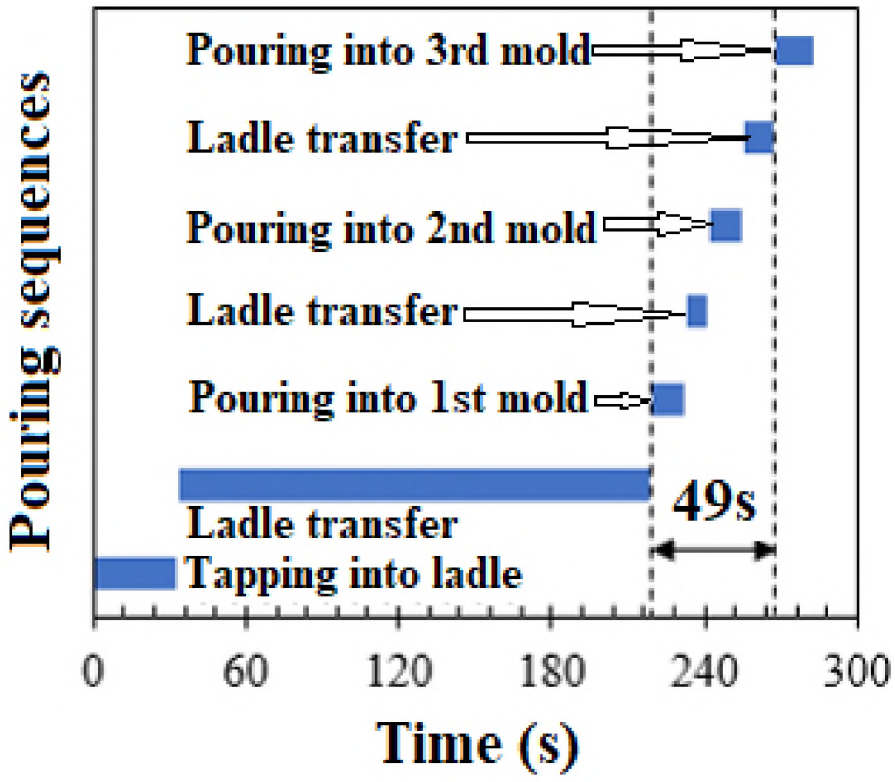

(a)

Figure 16. (a) Pouring sequences indicate that the steel melt at the top of the teapot ladle was reoxidized due to air contact and that metal was poured into the third mold showing maximum inclusion area fraction and (b) size distribution of the alumina inclusions at filter inlet for all three mold sets confirm this observation.

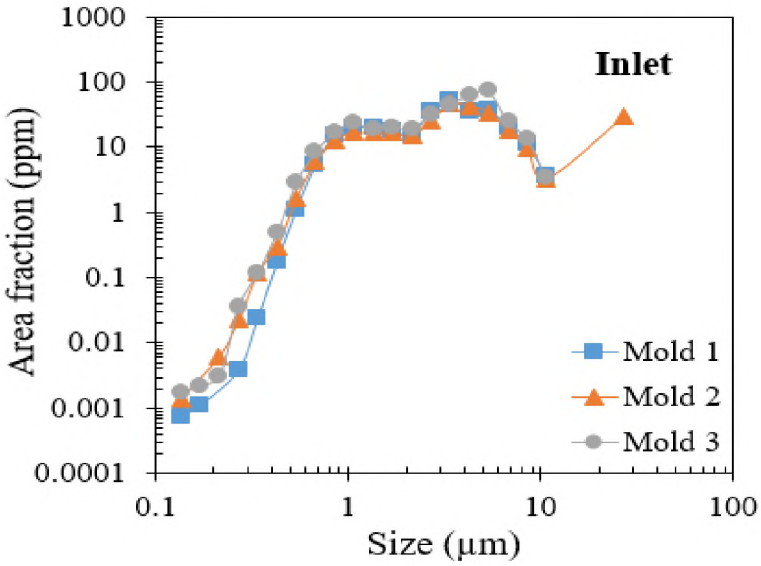

(b)

Figure 16. (a) Pouring sequences indicate that the steel melt at the top of the teapot ladle was reoxidized due to air contact and that metal was poured into the third mold showing maximum inclusion area fraction and (b) size distribution of the alumina inclusions at filter inlet for all three mold sets confirm this observation (cont.).

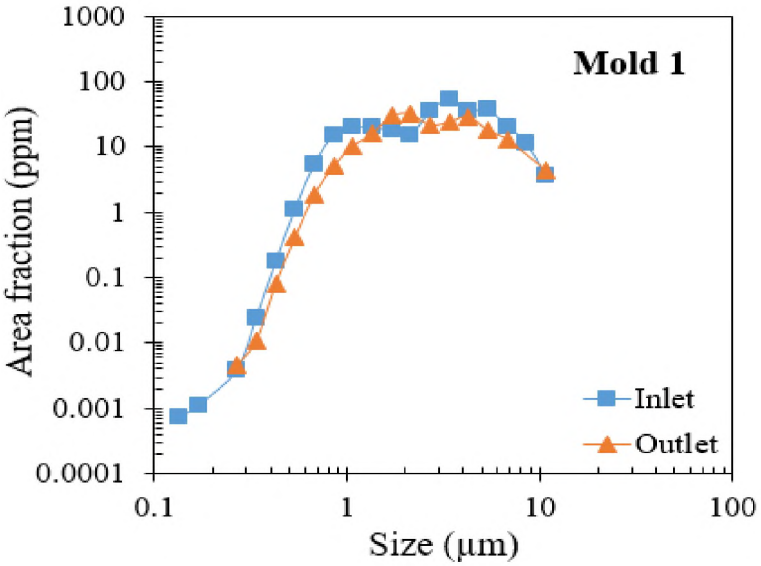

(a)

Figure 17. Comparison of alumina inclusions size distribution between samples at filter inlet and outlet for (a) mold 1, (b) mold 2 and (c) mold 3.

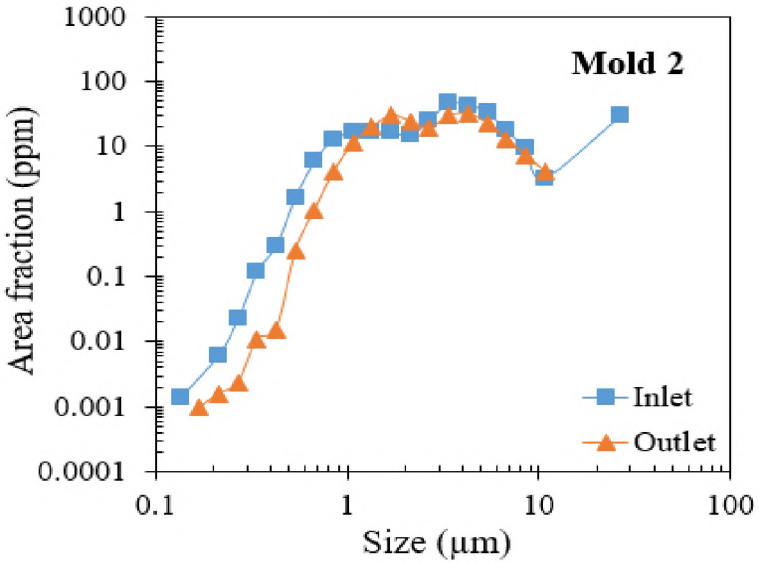

(b)

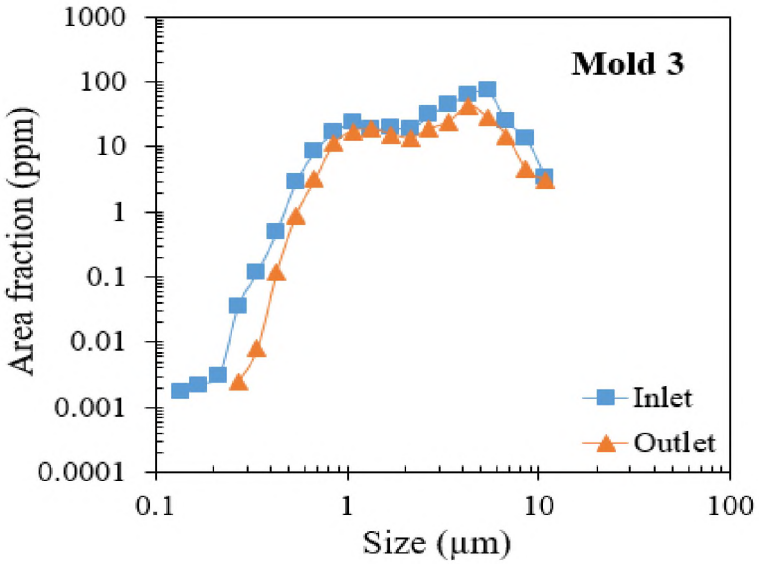

(c)

Figure 17. Comparison of alumina inclusions size distribution between samples at filter inlet and outlet for (a) mold 1, (b) mold 2 and (c) mold 3 (cont.).

The change in inclusion area fraction from the filter outlet to the runner section of the mold was generally small; within 4% for all three molds. However, these variations

are within the experimental error of the inclusion analysis. For all three molds, a drop in the area fraction of the inclusions was observed in samples from the filtered runner to the filtered casting. This is likely due to the floatation of the larger inclusions towards the risers during filling. The overall inclusion removal was determined by comparing the inclusion area fraction of filter inlet with the inclusion area fraction for the filtered casting. It can also be observed that the area fraction of the inclusions decreased by 32%, 29% and 47%, respectively for mold 1, mold 2 and mold 3 (Figure 18(a)). This observation indicates that the overall decrease in inclusion content is the result of a combination of filtration and floatation of the inclusions inside the mold cavity. It also suggests that the larger inclusions are more likely to be removed by the combination of filtration and floatation.

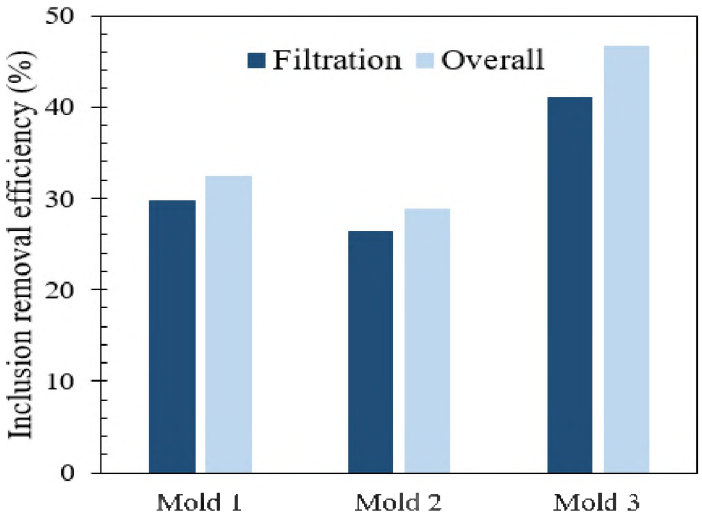

(a)

Figure 18. (a) Inclusion removal efficiency by filtration, floatation and combined effect and (b) comparison of area fractions of the alumina inclusions for unfiltered and filtered castings for all three molds.

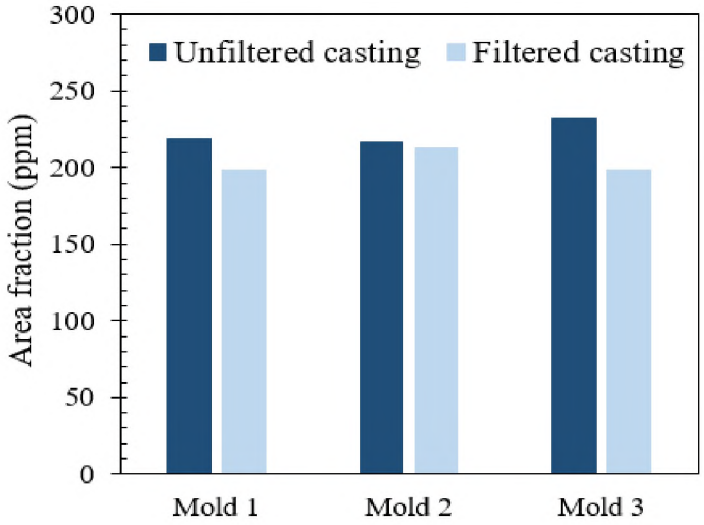

(b)

Figure 18. (a) Inclusion removal efficiency by filtration, floatation and combined effect and (b) comparison of area fractions of the alumina inclusions for unfiltered and filtered castings for all three molds (cont.).

Thickness of alumina layer captured by the filter can be converted into a volume fraction of inclusions captured by filter using the principals of stereology [25]. Volume of the filter section ($V_{section}$) divided by volume of steel within the filter (V_{steel}) is equivalent to thickness of the filter section ($T_{section}$) divided by thickness of steel within the filter (T_{steel}).The volume of steel is equal to the porous volume of the filter (~85% of total volume), which was filled by molten steel after filtration. Using Equation 6, the ratio of $T_{section}$ to T_{steel} can be calculated.

$$\frac{V_{section}}{V_{steel}} = \frac{T_{section}}{T_{steel}} = \frac{1}{0.85} \tag{6}$$

Inclusion area fraction (A_A) can be easily determined by normalizing alumina layer thickness (T) with the thickness of each of the sectioned filtration sample ($T_{section}$ =5mm or 5000μm), multiplied by the ratio of $T_{section}$ to T_{steel} as given by Equation 7.

Area fractions of the captured inclusions were measured and plotted at five positions through the filter thickness for all three mold sets. The results indicate that the entry side of mold 3 filter captured the highest amount of inclusions (240ppm), followed by mold 2 (187ppm) and mold 1 (161ppm) filters as shown in Figure 19. If the probability of inclusion capture is proportional to the local inclusion concentration entering each section of the filter element, as suggested, by Equation 3, then an exponential drop in the volume fraction of inclusions through the filter thickness should be observed. Our measurements appear to confirm this prediction.

$$A_A = \frac{T}{T_{section}} \times \frac{T_{section}}{T_{steel}} \times 10^6 ppm = 235.3 T ppm \tag{7}$$

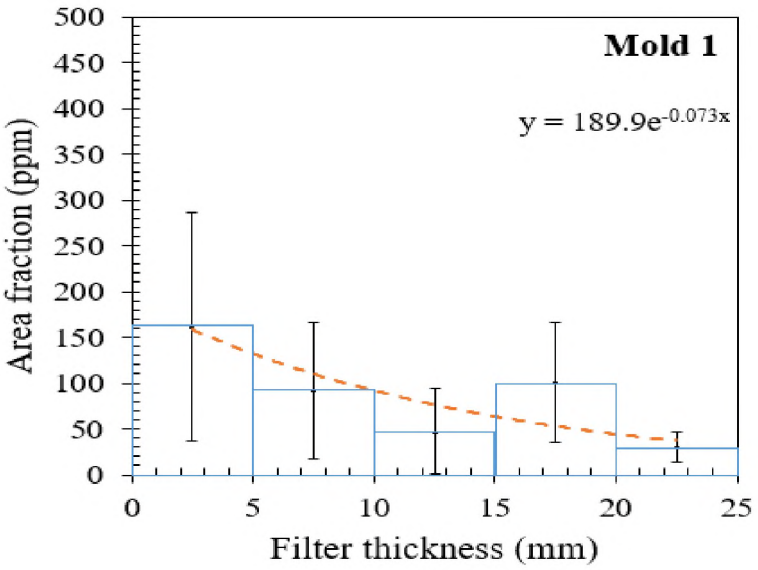

(a)

Figure 19. Distributions of volume fraction of captured alumina inclusions through the filter thickness for (a) mold 1, (b) mold 2 and (c) mold 3.

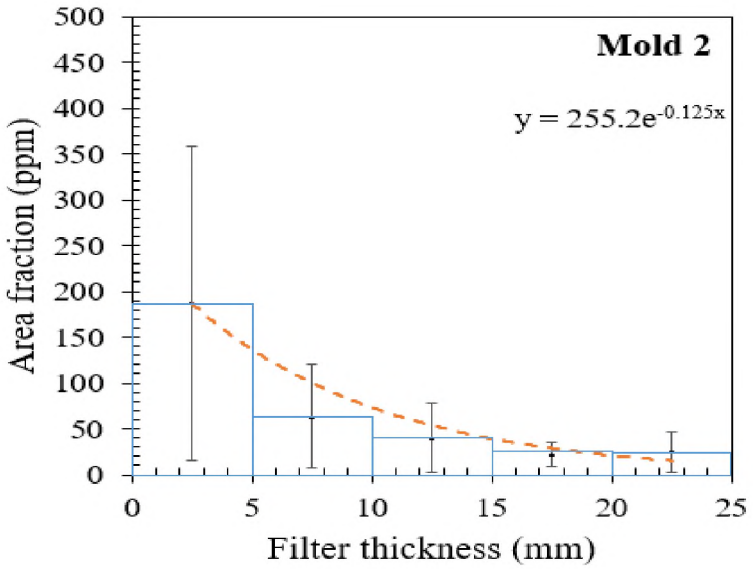

(b)

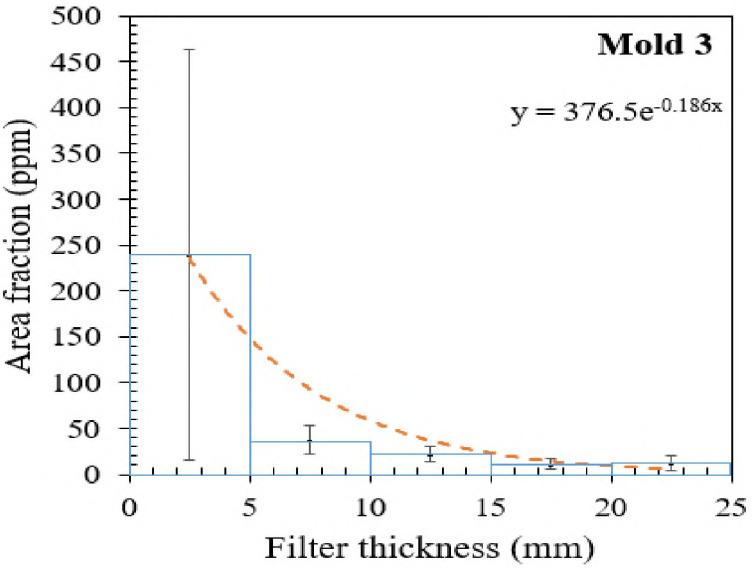

(c)

Figure 19. Distributions of volume fraction of captured alumina inclusions through the filter thickness for (a) mold 1, (b) mold 2 and (c) mold 3 (cont.).

7. CONCLUSIONS

A mold assembly with a special rigging system was designed using MAGMASOFT® 5.3.1 to study the efficiency of solid alumina inclusion removal by ceramic foam filtration. The design employs two Y-block castings in a single mold assembly, one with a filter in the runner and one without a filter. An experiment was carried out using three molds that were filled from a single ladle to observe the effects of varying amounts of incoming inclusions on filtration efficiency in a single heat. From this experiment, the following conclusions can be drawn:

1. Successively teemed molds using a bottom pour teapot-style ladle were observed to have increasing incoming inclusion concentrations. This is likely due to the reoxidation in the ladle during holding and pouring.
2. Zirconia (10ppi) foam filters successfully removed alumina inclusions from steel melt. In this experiment, the last mold poured (mold 3) had the highest incoming concentration of inclusions (371ppm) and also the highest inclusion removal efficiency by filtration (41%).
3. Floatation of some of the inclusions inside the mold cavity also contributed to inclusion removal. Filtered casting side of all three molds showed inclusion removal due to floatation in the mold cavity.
4. Both filtration and floatation mechanisms appear to play an important role for inclusion removal. The combined effect is larger than filtration alone. In this study, the highest combined inclusion removal efficiency observed in mold 3 was 47%, with filtration accounting for 41% of the removal efficiency.

5. Inclusions were captured within the filter element by deep bed filtration and accumulated on the steel-web interface within the filter. The entry side volume of the filter captured more inclusions than the exit side, and the amount captured decayed exponentially towards the exit side of the filter. The inclusion distribution through the filter followed a first order capture mechanism, in agreement with the predictions of Apelian et.al. [13].
6. SEM-EDS elemental mapping combined with quantitative metallography and AFA analysis appear to useful tools for quantifying inclusion removal efficiency and inclusion capture during molten metal filtration.

ACKNOWLEDGMENTS

The authors wish to gratefully acknowledge the support and guidance from the industry mentoring committee of Peaslee Steel Manufacturing Research Center. Special thanks go to MetalTek International and Foseco for their donation of materials to carry out these experiments. The authors would also like to greatly acknowledge Dr. Von Richards, Dr. Jeffrey Smith and Dr. Simon Lekakh for their technical support, and Logan Huddleston for helping with sample preparation.

REFERENCES

1. W. Simmons, "Influence of Metal Filtration on the Production of High Integrity Cast Products", *Foundry Trade Journal*, January, p. 24. (1985)
2. D. Apelian, R. Mutharasan and S. Ali, "Removal of Inclusions from Steel Melts by Filtration", *Journal of Materials Science*, 20, p. 3501 (1985).

3. K. Janiszewski and Z. Kudlinski, "The Influence of Non-Metallic Inclusions Physical State on Effectiveness of the Steel Filtration Process", *Steel Research International*, 77(3), p. 169 (2006).

4. K. Raiber, P. Hammerschmid and D. Janke, "Experimental Studies on Al_2O_3 Inclusions Removal from Steel Melts Using Ceramic Filters", *ISIJ International*, 35(4), p. 380 (1995).

5. L. Aubrey, J. Brockmeyer, P. Wieser, I. Dutta and A. Ilhan, "Cast Steel Quality Improvement by Filtration with Ceramic Foam Filters", *AFS Transactions*, 93, p. 177 (1985).

6. L. Aubrey, J. Schmahl and M. Cummings, "Application of Advanced Reticulated Ceramic Foam Filter Technology to Produce Clean Steel Castings", *AFS Transactions*, 101, p. 59 (1993).

7. J. Stamper, "Filtration of Steel Castings with Ceramic Foam Filters", *AFS Transactions*, 93, p. 867 (1985).

8. W. Su, T. Johnson, J. Day, J. Wallace and F. Li, "The Development and Characterization of Extruded Cellular-Ceramic Filters for Steel Foundry Applications", *AFS Transactions*, 96, p. 161 (1988).

9. T. Johnson, H. Kind, J. Wallace, C. Nieh and H. Kim, "Laboratory and Foundry Performance Characterization of Extruded Cellular Ceramic Filters for Steel Foundry Applications", *AFS Transactions*, 97, p. 879 (1989).

10. S. Ali, R. Mutharasan and D. Apelian, "Physical Refining of Steel Melts by Filtration", *Metallurgical Transaction B*, 16B, p. 725 (1985).

11. C. Tian, "On the Removal of Non-Metallic Inclusions from Molten Steel through Filtration", PhD Dissertation: McGill University, Montreal, Quebec, Canada (1990).

12. K. Janiszewski, "Influence of Slenderness Ratios of a Multi-Hole Ceramic Filters at the Effectiveness of Process of Filtration of Non-Metallic Inclusions from Liquid Steel", *Archives of Metallurgy and Materials*, 57(1), p. 135 (2012).

13. D. Apelian and R. Mutharasan, "Filtration: A Melt Refining Method", *Journal of Metals*, p. 14 (1980).

14. MAGMASOFT® 5.3.1: https://www.magmasoft.com/en/

15. S. Chakraborty, R. O'Malley, L. Bartlett and M. Xu, "Efficiency of Solid Inclusion Removal from the Steel Melt by Ceramic Foam Filter: Design and Experimental Validation", *AFS Transactions*, 126, p. 325 (2018).

16. S. Chakraborty, R. O'Malley, L. Bartlett and L. Huddleston, "Effect of Physical State of Non-metallic Inclusions on the Accumulation within Magnesia Stabilized Zirconia Foam Filters", *Proceedings of the Iron & Steel Technology Conference*, Pittsburgh, PA, USA, p. 1029 (2019).

17. J. Campbell, "Complete Casting Handbook", Elsevier Ltd.: Oxford, UK (2011).

18. S. Majidi and C. Beckermann, "Effect of Pouring Conditions and Gating System Design on Air Entrainment during Mold Filling", *International Journal of Metalcasting*, 13, p. 255 (2019).

19. K. Metzloff, K. Mageza and D. Sekotlong, "Velocity Measurement and Verification with Modeling of Naturally Pressurized Gating Systems", *International Journal of Metalcasting*, 14, p. 610 (2020).

20. FactSage™ 7.2: www.factsage.com

21. M. Heidarzadeh and H. Keshmiri, "Influence of Mould and Insulation Design on Soundness of Tool Steel Ingot by Numerical Simulation", *Journal of Iron and Steel Research International,* 20 (7), p. 78 (2013).

22. K. Carlson and C. Beckermann, "Use of the Niyama Criterion to Predict Shrinkage-Related Leaks in High-Nickel Steel and Nickel-Based Alloy Castings", *Proceedings of the 62nd SFSA Technical and Operating Conference*, Chicago, IL, USA (2008).

23. M. Kang, H. Gao, J. Wang, L. Ling and B. Sun, "Prediction of Microporosity in Complex Thin-Wall Castings with the Dimensionless Niyama Criterion", *Materials,* 6, p. 1789 (2013).

24. K. Carlson, S. Ou, R. Hardin and C. Beckermann, "Development of a Methodology to Predict and Prevent Leaks Caused by Microporosity in Steel Castings", *Proceedings of the 55th SFSA Technical and Operating Conference*, Chicago, IL, USA (2001).

25. E. Underwood, "Quantitative Stereology", Addison-Wesley Publ. Co.: Massachusetts, USA (1970).

II. EFFECT OF PHYSICAL STATE OF NON-METALLIC INCLUSIONS ON THE ACCUMULATION WITHIN MAGNESIA STABILIZED ZIRCONIA FOAM FILTERS

Soumava Chakraborty, Ronald J. O'Malley, Laura Bartlett and Logan Huddleston

Peaslee Steel Manufacturing Research Center, Department of Materials Science and Engineering, Missouri University of Science and Technology, 1400 North Bishop Avenue, Rolla, MO, USA, 65409-0340

ABSTRACT

Ceramic foam filters are routinely used in steel foundries to remove inclusions. Experiments were carried out to filter both aluminum and silicomanganese deoxidized AISI 316 stainless steel utilizing 10ppi magnesia stabilized zirconia foam filters. The objective was to determine the attachment mechanisms of solid versus liquid inclusions. The results documented the removal of inclusions for both conditions. Samples were prepared directly from the filter to investigate the inclusion attachment mechanism during deep bed filtration using optical, cathodoluminescence and electron microscopy. Energy dispersive X-ray spectroscopy was utilized to evaluate the change in filter micropore saturation by liquid inclusions through the thickness of the filter.

Keywords: Steel, Non-metallic inclusions, Ceramic foam filter, Filtration mechanism, Filter micropore saturation

1. INTRODUCTION

In foundry steelmaking, filtration is a common practice to lower the concentration of non-metallic inclusions in steel castings. Removal of non-metallic inclusions reduces the scrap rate and improves machinability, casting appearance and mechanical properties [1]. Non-metallic inclusions are captured by different types of ceramic filters, the choice of which depends on the specific application and location in the process. Ceramic foam filters are commonly utilized in multiple positions in the gating system of sand molds and are effective by a deep bed filtration mechanism [2]. Inclusions can be formed during the melting, pouring and casting and are separated into two main categories of endogenous and exogenous inclusions. Exogenous inclusions come from sources outside the refining process, such as worn refractories, slag, sand, or by reoxidation of the melt and are often much larger than endogenous inclusions. Endogenous inclusions are formed as consequence of the steelmaking and refining process and can be modified at different stages of steelmaking operation for effective removal. Depending on the deoxidizer used, the physical state of the inclusions can be both solid and liquid. Filtration of both solid (alumina) and liquid (manganese silicate) inclusions have been reported by several authors [2-5], however, the differences in the capture method have not been well documented. The equilibrium reactions during deoxidization of molten steel using aluminum and silicomanganese can be represented by Equation (1) and (2).

$$2[Al] + 3[O] = (Al_2O_3)_{solid} \quad (1)$$

$$x[Mn] + y[Si] + (x+2y)[O] = (xMnO, ySiO_2)_{liquid} \quad (2)$$

Several studies have been performed to understand the role of ceramic filters in the capture of non-metallic inclusions. In a previous study, a thermodynamic model was developed to predict the spontaneous adsorption of non-metallic liquid inclusions on ceramic filter. The surface area of the inclusions, the contact angle and interfacial tension between inclusion and filter were directly proportional to the Gibbs free energy change during filtration [4]. The adsorption force between a ceramic loop or monolithic filter and a spherical inclusion particle was determined to be higher than for two spherical inclusion particles, which helped the non-metallic inclusions to attach to the filter surface [6]. The rate determining step of alumina inclusion filtration by a ceramic loop filter, which is effective for high filtration efficiency, is the transport of inclusions from molten steel to filter surface. This transport of inclusions depends on several parameters such as effective turbulent diffusivity in molten steel, radii of alumina inclusions, diameter and total surface area of loop filter string, temperature, volume, velocity and viscosity of molten steel, filter void ratio etc. [7]. The efficiency of the deep bed filtration mechanism is also a strong function of the approach velocity of metal (U_m) and can be represented with Equation (3), where K_0 is a function of the characteristics of the filter, such as pore structure, tortuosity, etc. Z is the distance from the filter entrance, C_i and C(Z) are the inclusion concentrations at the filter inlet and a distance, Z, from the filter inlet respectively [8].

$$\frac{C(Z)}{C_i} = exp(\frac{-K_0 Z}{U_m}) \tag{3}$$

One of the major issues with using a ceramic filter is to prime it properly. At the beginning of pouring, the liquid steel must pass through the filter without solidifying in

the filter webs. This can be achieved by supplying enough heat from the incoming metal and designing a proper rigging system [9].

In this current study, a mold design was utilized based on a computational fluid dynamics model to study solid and liquid inclusions filtration mechanism for a cast 316 stainless steel. To compare the different filtration mechanisms of solid and liquid inclusions, two separate experimental heats were carried out with similar process conditions using aluminum (Al) and silicomanganese (SiMn) deoxidizers to form solid alumina (Al_2O_3) and liquid manganese silicate ($xMnO.ySiO_2$) inclusions in the steel melt.

2. MOLD DESIGN

Mold design was optimized by solving the transient continuity, momentum transfer, and heat transfer equations for the 3D geometry numerically using the computational fluid dynamics software MAGMASOFT® 5.3.0 [10]. In this design, two Y-block castings were filled using a common pouring basin to maintain the same chemistry and temperature of the steel melt for both castings. These blocks were filled using two separated rigging systems to minimize the back pressure generated inside the mold cavity. Commercially available magnesia stabilized zirconia 10ppi foam filters with dimensions of 100mm X 100mm X 25mm were attached with one of the rigging systems while the other system remained unfiltered. The Y-block castings, rigging, and feeding system are shown in Figure 1.

Three of these molds were poured from a single 80kg heat. The purpose of pouring three molds was to see the filtration efficiency for different inclusion

concentrations for same composition of the steel melt. The metal velocity was kept below a critical value of 0.45m/s [11] to bottom fill the Y-blocks to minimize the surface turbulence and reoxidation. Both Y-block castings were designed to fill at the same rate. The effect of inclusion removal on mechanical properties can be evaluated in a subsequent study and to support this, the microporosity levels of the Y-blocks were kept very low (<0.15%) to make sound castings. The details of the design and mathematical simulation were discussed in a previous work of the authors [12].

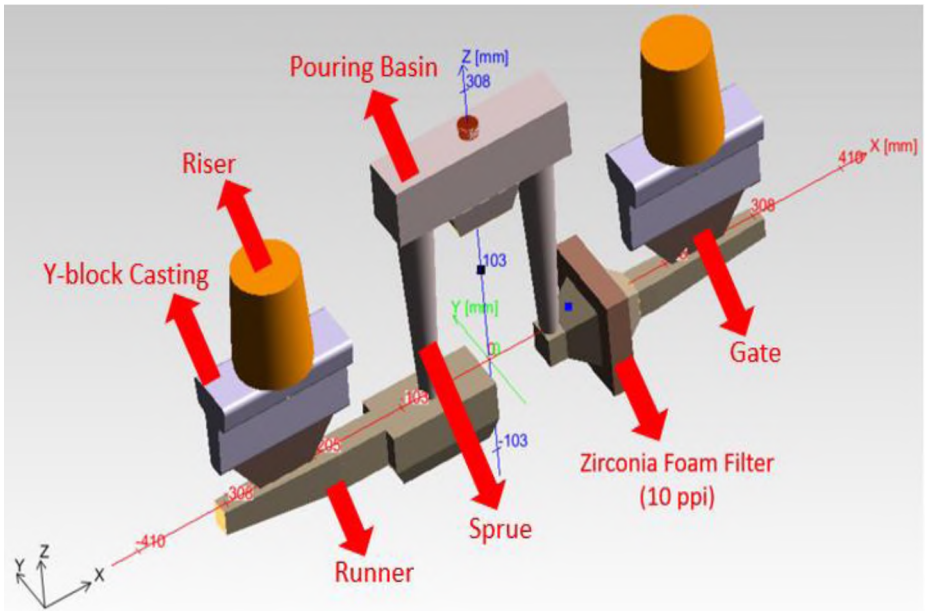

Figure 1. Casting and rigging system designed with the computational fluid dynamics software and used for the experiments.

The computational fluid dynamics software that was utilized to examine the temperature profile inside the filter at different stages of mold filling confirmed that there was no premature solidification. The temperature profiles for the filter as a function of total amount of metal volume poured are shown in Figure 2 (a). The results showed that

almost every portion of the filter, except the upper corner at very late stage of mold filling, had temperature higher than liquidus temperature (1454°C). Therefore, the center of the filter can be used to evaluate the inclusion attachment mechanisms.

The velocity profiles through the filter at different stages of mold filling were also calculated using this model and shown in Figure 2 (b). The filter opposes the momentum of the molten metal and decreases the velocity of the metal passing through it. As the velocity decreases, it increases the probability that an inclusion will have enough residence time to attach to the filter. In this model, a 10ppi foam filter was used (FOSECO STELEX ZR™) from the software database. The residence time ($t_{residence}$) of the inclusions inside the filter is given by Equation 4, where T_{filter} is the filter thickness, and V_{steel} is the mean velocity of the steel melt through the porous area of filter. Thus, the lower the velocity and the thicker the filter, the higher the residence time of the inclusion and the higher the likelihood of inclusion attachment [13, 14]. In this model, the velocity at each location of the mold cavity at every time step was kept low (<0.45m/s) also to minimize the surface turbulence and hence reoxidation after filtration.

$$t_{residence} = \frac{T_{filter}}{V_{steel}} \tag{4}$$

3. EXPERIMENTAL PROCEDURE

Patterns were 3D printed using acrylonitrile butadiene styrene polymer and glued inside a wooden mold flask. This mold flask was used to prepare no-bake sand molds. The dimension of the mold was 700mm X 200mm X 350mm and they were vertically

parted into two halves. For the experimental heats, magnesia stabilized zirconia 10ppi square foam filters were used. A scanned image of the cross-section of an unused filter specimen is shown in Figure 3. The image shows that the filter has two types of pore structures: macropores and micropores. The macropores allow the liquid metal to pass through the filter element during mold filling. The volume fraction of these macropores was determined to be approximately 85% of the total filter volume. The micropores were present within the web structure of the filter element, which was not penetrated by liquid steel.

Two different experimental heats were carried out to produce Al-killed and SiMn-killed SS 316, to generate solid alumina (Al_2O_3) and liquid manganese silicate ($xMnO.ySiO_2$) inclusions respectively. For both of these experiments, the charge materials were melted in a 90kg (200lb) induction furnace under argon cover. Melts were tapped in a preheated 90kg (200lb) teapot style ladle for both experiments. In experiment 1, Al deoxidizer was added into the metal stream during tapping, whereas in experiment 2, SiMn deoxidizer was added as a mixture of FeSi and FeMn. Due to the large quantity of ferroalloys used in experiment 2, 90wt.% of it was added into the furnace and rest into the metal stream to ensure a proper mixing with the steel melt. After deoxidization, three molds were poured consecutively for each experiment. Due to variation in metal residence time in the ladle for pouring these three molds, amount of inclusions in the steel melt was expected to vary. The molds were shaken out after the castings were completely solidified and cooled down to room temperature. Experimental parameters for both heats are summarized in Table 1.

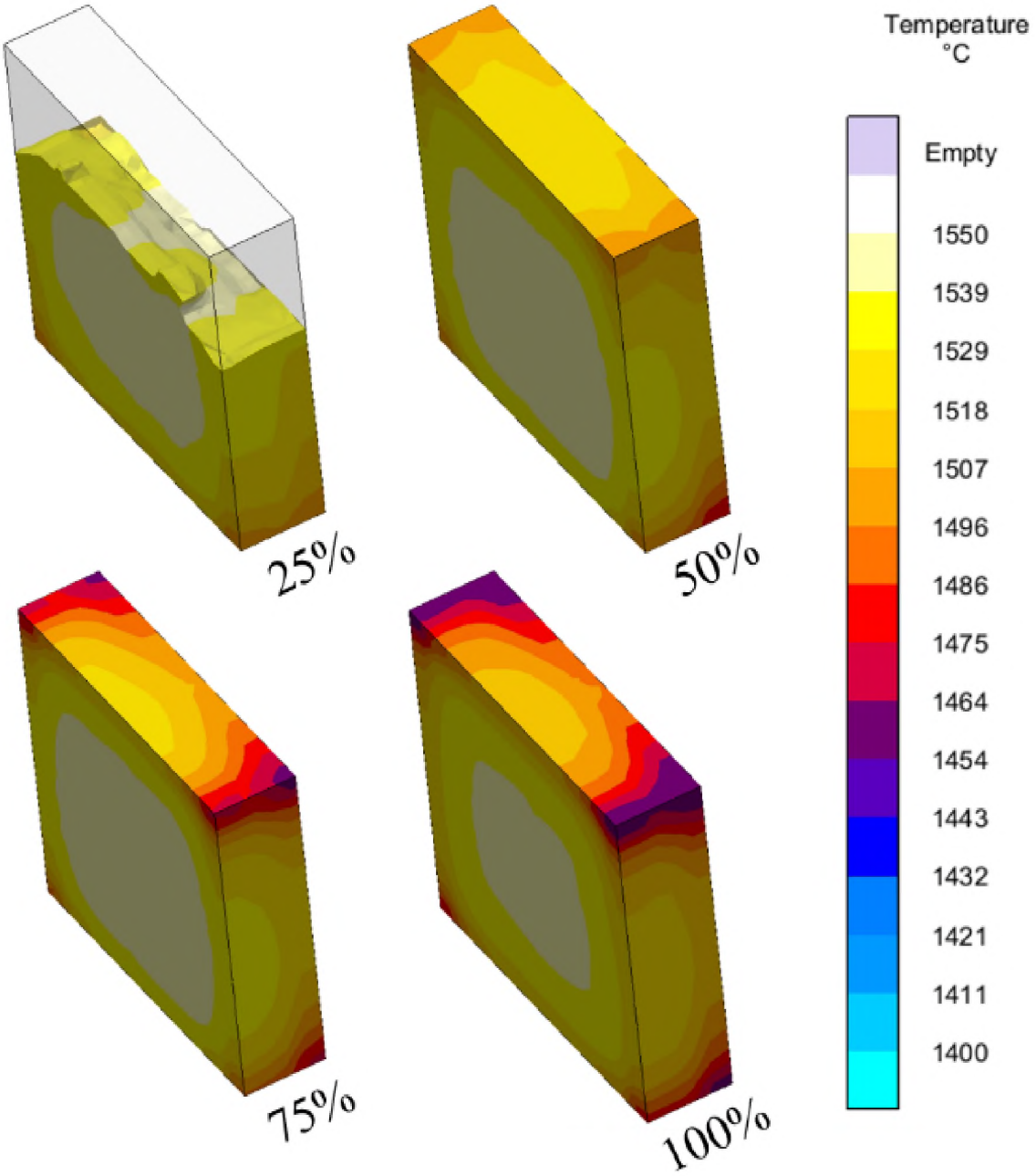

(a)

Figure 2. (a) Temperature profiles and (b) velocity profiles of the steel melt inside the foam filter after 25, 50, 75 and 100% of the total casting volume filled (inlet and outlet orientations of the filter are same as Figure 1).

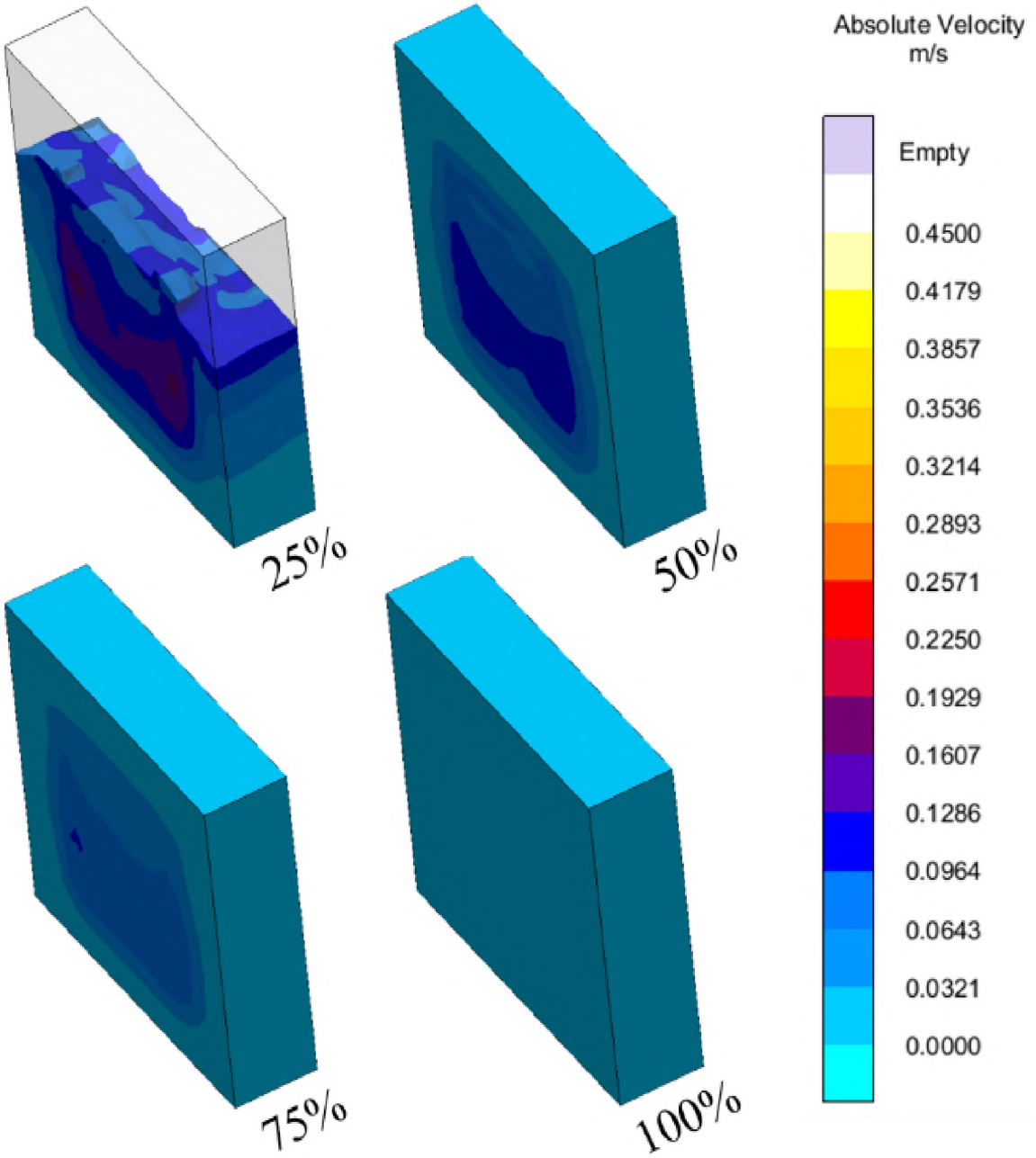

(b)

Figure 2. (a) Temperature profiles and (b) velocity profiles of the steel melt inside the foam filter after 25, 50, 75 and 100% of the total casting volume filled (inlet and outlet orientations of the filter are same as Figure 1) (cont.).

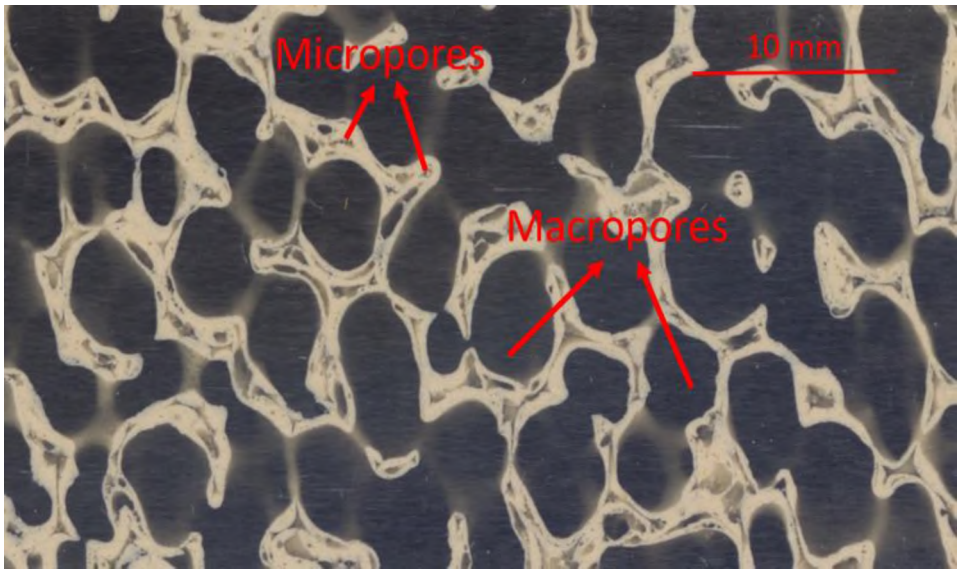

Figure 3. Scanned image of an unused filter specimen showed both macropores and micropores.

Table 1. Experimental parameters for Al deoxidized and SiMn deoxidized SS 316 castings.

Experiment	**Deoxidizer used**	**Deoxidization sequence**	**Tapping temperature (°C)**	**Pouring temperature (°C)**
1	Al	100% in tapping stream	1644	1554
2	FeSi + FeMn	90% in furnace + 10% in tapping stream	1643	1550

The chemistry samples were collected from ladle for both experiments and were analyzed using an Optical Emission Arc Spectrometer (FOUNDRY-MASTER, OXFORD INSTRUMENTS). For accurate measurement of O and N, LECO TC 500 and for C and S, LECO CS 600 combustion methods were utilized.

The filters were sectioned from all of the castings. A schematic of sample preparation method from the filters is shown in Figure 4. To examine the inclusion attachment at the center of the filters (area marked in red), the filters were cut into smaller pieces and then impregnated with epoxy resin under vacuum to avoid air bubble formation and allowed to cure. After curing, filter samples were further cut into five pieces that were approximately 5mm wide using a diamond sectioning blade to evaluate any changes in attachment mechanism through the filter thickness. These samples were again mounted with epoxy under vacuum and polished using standard metallographic polishing procedures.

The resulting samples were analyzed by optical microscopy and cathodoluminescence imaging using Nikon Labophot-2 Pol. Specimens were then coated with Au/Pd using Hummer VI Sputtering System at 5-8mA under vacuum for 3minutes (~80Å/minute) to prevent overcharging of the sample during subsequent electron microscopy examination. Elemental maps and line scans of the filtration samples were created utilizing a scanning electron microscope with energy dispersive X-ray spectroscope attachment (ASPEX PICA 1020).

To determine the details of 3D inclusion attachment, selected samples were sectioned from different portions of the filters from both experiments. The filter sections were partially dissolved in a solution of triethanolamine (2vol./vol.%) and tetramethylammonium chloride (1wt./vol.%) in methanol as described in previous studies [15-17]. Samples were electrolytically etched for 5-6hours with an anode current density of ~50mA/cm^2. This solution etched away the selected steel surface by about 0.5-1mm, depending on the metal to filter ratio present in each sample. The etched samples were

then washed with methanol, dried, and then coated with Au/Pd using same procedure as previously mentioned.

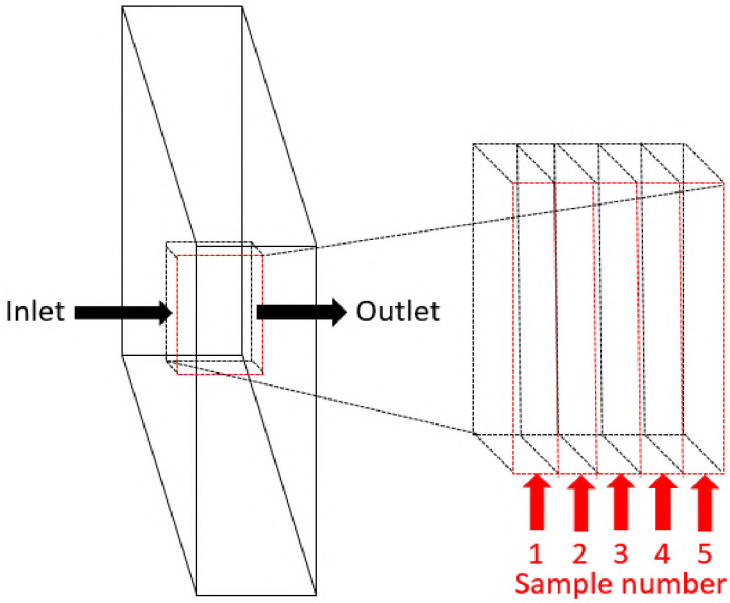

Figure 4. Schematic diagram of filter sectioning method.

4. RESULTS AND DISCUSSION

4.1. THERMODYNAMIC CALCULATION

The final compositions of the steel after deoxidization are documented in Table 2. The oxygen contents shown here represented the total oxygen content.

These chemistries were fed into thermodynamic software package FactSage™ 7.2 [18] and the presence of solid alumina and liquid manganese silicate inclusions were confirmed at the pouring temperatures for Al deoxidized and SiMn deoxidized steel melts. Al acts as a strong deoxidizer and with a high Al content (0.120%) in the steel

melt, mostly Al_2O_3 inclusions were formed during Al deoxidization practice. In contrast to this, for SiMn deoxidized steel, a mixture of liquid inclusions were observed, where $xMnO.ySiO_2$ were the major constituent (~65wt.% at 1550°C) and hence this inclusions were regarded as manganese silicate inclusions for the following analysis. The composition of the liquid inclusions for experiment 2 is shown in Figure 5(a). Formation of other oxides like Al_2O_3, Cr_2O_3, TiO_2 etc. in the liquid inclusions, was also evident for the current SiMn deoxidized SS 316 composition due to the strong affinity of Al, Cr and Ti towards O. Scanning electron microscopic images of alumina cluster and manganese silicate inclusions from these two experiments are represented in Figure 5(b). Spherical shape of the manganese silicate inclusions also indicate that the inclusions were in the liquid state.

Table 2. Compositions of Al deoxidized steel (experiment 1) and SiMn deoxidized steel (experiment 2).

Experiment	C	Si	Mn	Mo	Cr	Ni	Al	Cu	Ti	N	S	O	Fe
1	0.084	1.40	0.52	2.47	18.67	9.00	0.120	0.23	0.014	0.0846	0.0044	0.0188	Bal.
2	0.018	0.57	1.29	2.41	17.41	8.20	0.003	0.01	<0.002	0.0149	0.0008	0.0237	Bal.

4.2. CATHODOLUMINESCENCE IMAGING

In cathodoluminescence (CL) microscopy, electrons are used to excite a material that has discrete band gaps, which causes the material to emit photons in the visible spectrum that can be observed by optical microscopy. In this study, magnesia (MgO) stabilized zirconia (ZrO_2) foam filters were used to capture alumina (Al_2O_3) and

manganese silicate ($xMnO.ySiO_2$) inclusions in two different experiments. These filter samples contain some oxides are expected emit different colors under CL imaging.

CL imaging was carried out under vacuum using an optical microscope equipped with a PAXcam2+3.1 megapixel low light CCD camera. In filter samples from experiment 1, clusters of alumina particles were observed along with zirconia filter web interface, as shown in Figure 6(a). In the filter samples from experiment 2, Figure 6(b), only the zirconia filter was observed by CL imaging. This is likely due to the fact that MnO in the manganese silicate inclusions is a transition metal oxide that suppresses the emission visible photons under CL excitation [19].

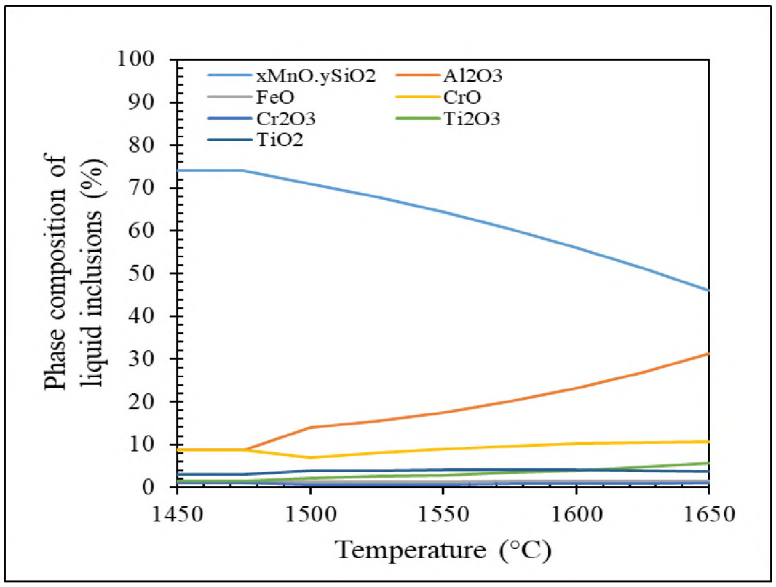

(a)

Figure 5. (a) Phase composition of liquid inclusions in SiMn deoxidized steel showed mixture of oxides and (b) scanning electron microscopic images of alumina cluster and manganese silicate inclusions formed in Al deoxidized and SiMn deoxidized steels respectively.

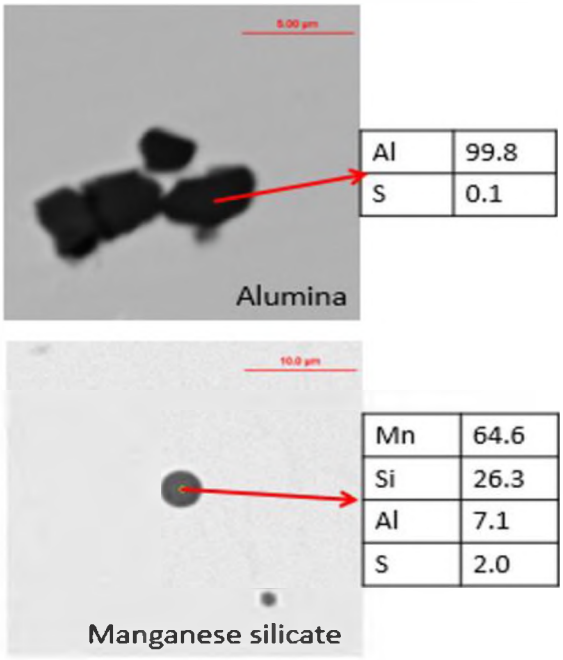

(b)

Figure 5. (a) Phase composition of liquid inclusions in SiMn deoxidized steel showed mixture of oxides and (b) scanning electron microscopic images of alumina cluster and manganese silicate inclusions formed in Al deoxidized and SiMn deoxidized steels respectively (cont.).

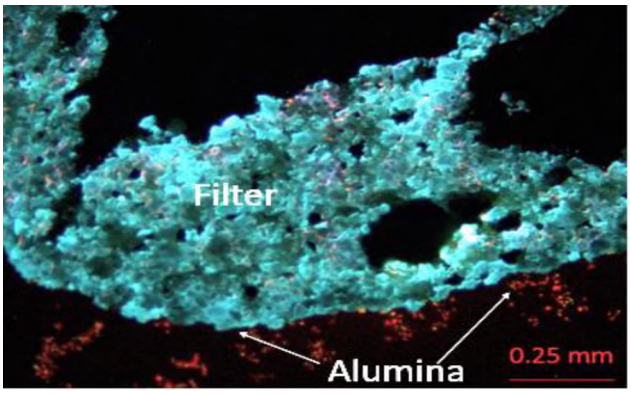

(a)

Figure 6. (a) Cathodoluminescence images showed the presence of alumina clusters (red) attached to the filter samples and (b) manganese silicate inclusions could not be detected by cathodoluminescence.

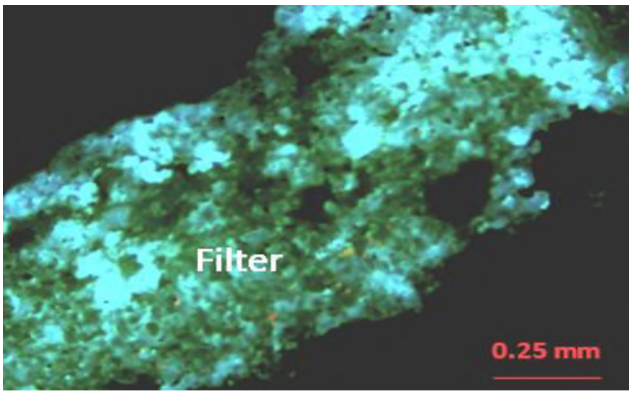

(b)

Figure 6. (a) Cathodoluminescence images showed the presence of alumina clusters (red) attached to the filter samples and (b) manganese silicate inclusions could not be detected by cathodoluminescence (cont.).

4.3. LINE SCANNING AND ELEMENTAL MAPPING

Line scans and elemental maps of the different filter samples from each mold identified the presence of pure alumina inclusions in the metal matrix and identified spinel at the metal-filter interface (Figure 7). Alumina particles near the metal matrix mostly found in clusters due to their strong adhesion forces. Magnesia is used to stabilize the zirconia during fabrication of the filter material and thus at the metal-filter interface this magnesia can react with captured alumina inclusions to form this Mg-Al spinel layer as shown in Equation 5. Therefore, in addition to the physical adsorption forces between the filter and the alumina inclusions, this chemical reaction further helped to improve the inclusion capturing efficiency.

$$(MgO)_{in\,filter} + (Al_2O_3)_{solid} = (MgO.\,Al_2O_3)_{solid} \quad (5)$$

In contrast to alumina inclusions, liquid manganese silicate inclusions were mostly observed within the small micropores of the web structure of the filter, while the

metal-filter macropore interface was devoid of inclusions. The presence of magnesia from the magnesia stabilized zirconia filter component was also observed in the micropores as shown in Figure 8. However, no continuous layer of inclusions was observed at the metal-filter interface in the filters sectioned from SiMn deoxidized steels. Thermodynamic modeling in Figure 5(a) shows that the manganese silicate inclusions are expected to be liquid as they pass through the filter. Our observations suggest that the liquid inclusions that contacted the filter were drawn into these micropores due to surface tension forces. This inclusion capture mechanism has not been discussed before in literature according to authors' knowledge.

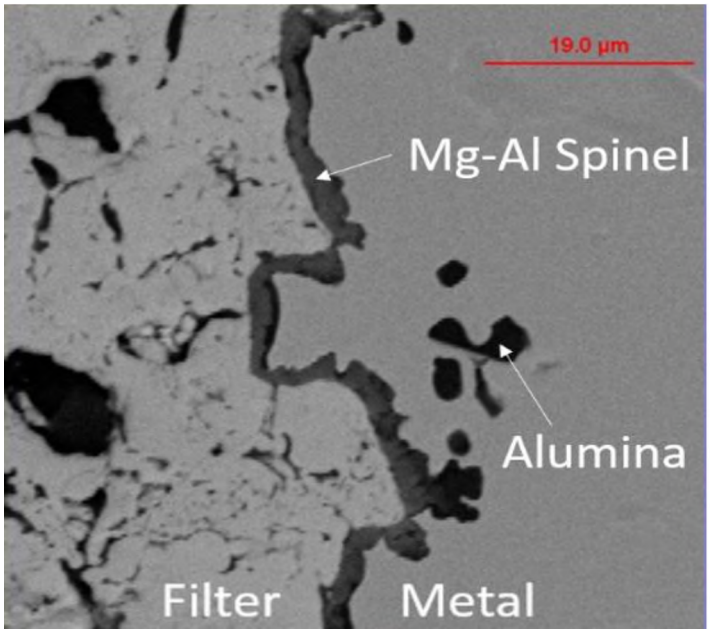

(a)

Figure 7. (a) A scanning electron microscopic image from sample 1 of the first mold of experiment 1 showed solid alumina inclusion and spinel layer, (b) line map of the same image showed the presence of pure alumina inclusions near the metal-filter interface and (c) elemental maps of the same image confirmed the presence of alumina and spinel layer.

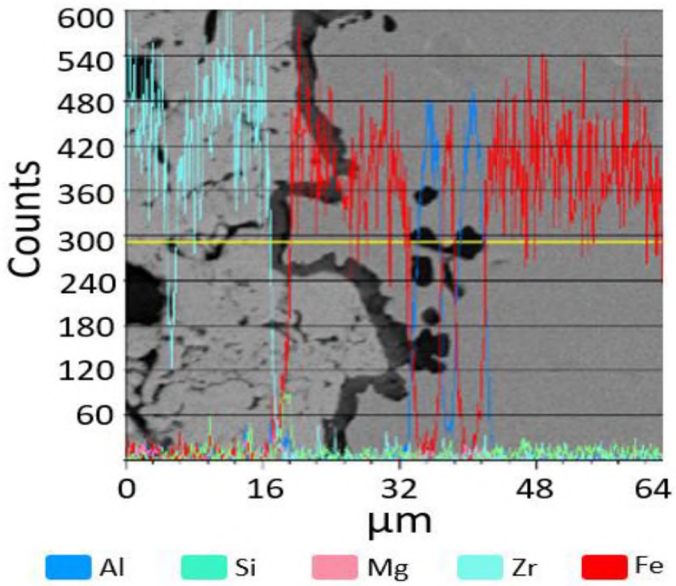

(b)

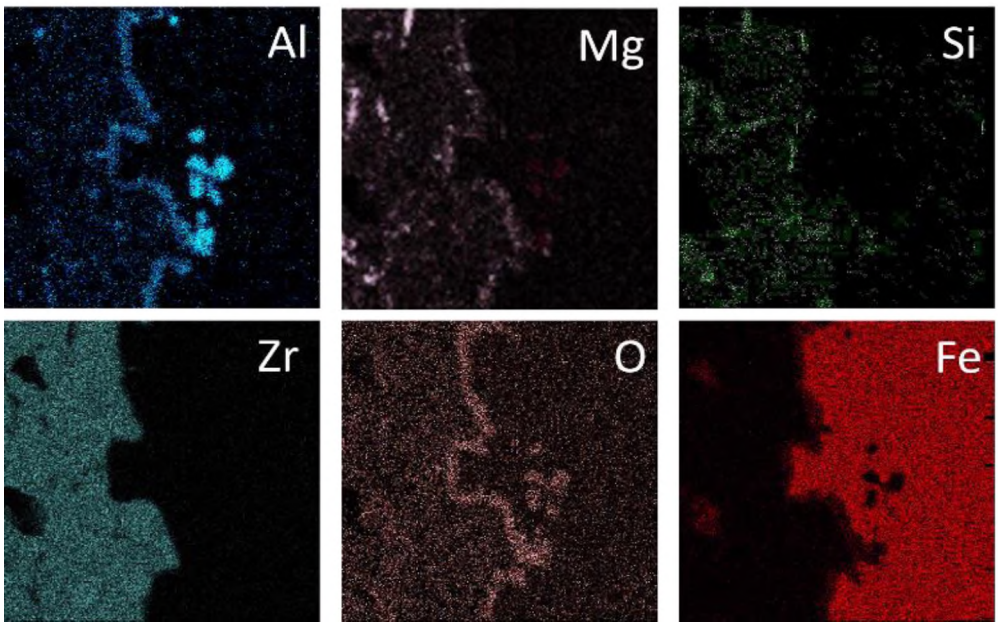

(c)

Figure 7. (a) A scanning electron microscopic image from sample 1 of the first mold of experiment 1 showed solid alumina inclusion and spinel layer, (b) line map of the same image showed the presence of pure alumina inclusions near the metal-filter interface and (c) elemental maps of the same image confirmed the presence of alumina and spinel layer (cont.).

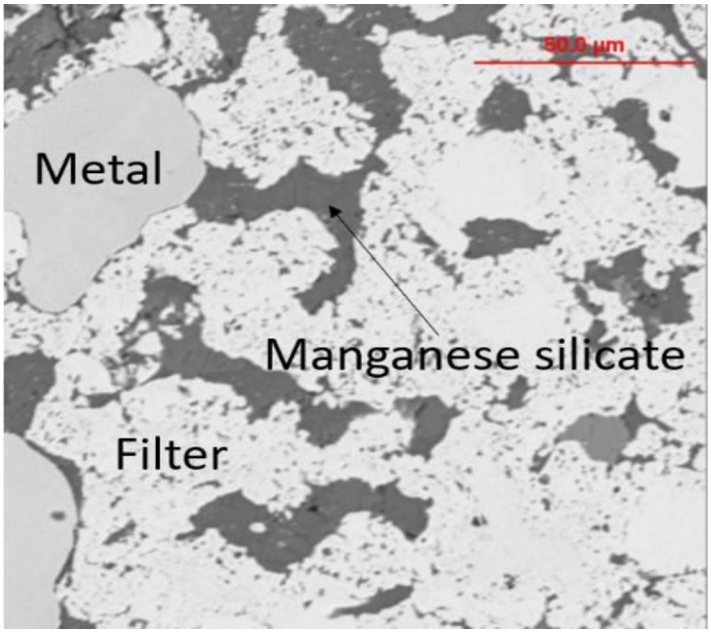

(a)

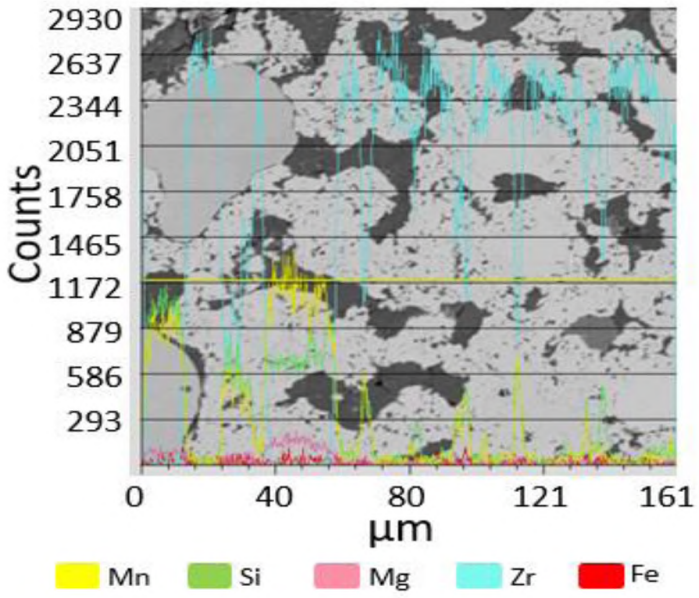

(b)

Figure 8. (a) A scanning electron microscopic image from sample 3 of the third mold of experiment 2 showed liquid manganese silicate inclusion entrapment inside the micropores, (b) line map of the same image showed the presence of manganese silicate inclusions in the micropores and (c) elemental maps of the same image confirmed the presence of both manganese silicate and magnesia in the filter micropores.

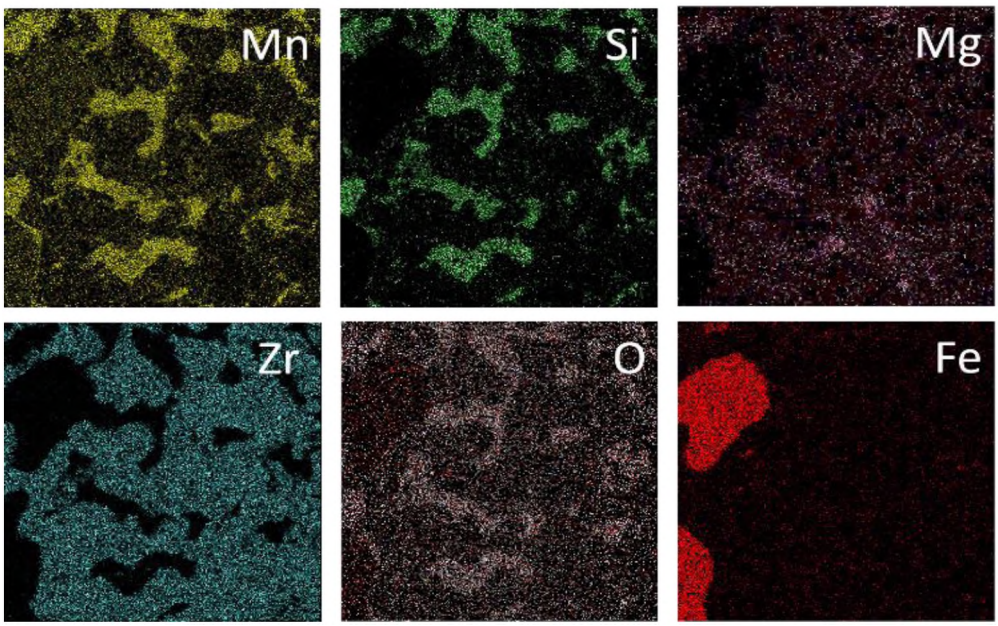

(c)

Figure 8. (a) A scanning electron microscopic image from sample 3 of the third mold of experiment 2 showed liquid manganese silicate inclusion entrapment inside the micropores, (b) line map of the same image showed the presence of manganese silicate inclusions in the micropores and (c) elemental maps of the same image confirmed the presence of both manganese silicate and magnesia in the filter micropores (cont.).

Electrolytic etching was performed with both types of filtration samples. The purpose of using this characterization method was to etch away part of the metal to reveal the metal-filter interface to better observe the inclusion attachment on the filter. Figure 9(a) shows the etched filter sample from the Al deoxidized steel at the metal-filter interface. Presence of spinel inclusions was observed at the metal-filter interface for the filter samples sectioned from the filter entry side of the second mold. Examination of the micropores in the Al deoxidized samples showed that alumina was absent within the micropores. The absence of alumina in the micropore areas confirms that solid alumina inclusions did not penetrate into the micropore area of the filter. In experiment 2, some

large manganese silicate inclusions were observed at the metal-filter interface, as shown in Figure 9(b). Small manganese silicate inclusions were also observed within the filter micropores along with some magnesia that was apparently picked up from the magnesia stabilized zirconia filter. Most of the manganese silicate inclusions that were observed were found within the micropores. These micropores were either partially or completely filled with manganese silicate.

The aim of this study was to understand the attachment mechanism of both solid and liquid inclusions on the filter. Using line scans, elemental maps and scanning electron microscopic images, it was established that the solid inclusions were captured mostly at the metal-filter interface, whereas the liquid inclusions resided mostly within the micropores in the filter web structure. The entrapment of liquid inclusions in filter micropores is a previously unreported filter capture mechanism and therefore, the relative saturation of the filter micropores was measured through the filter thickness to observe how these manganese silicate inclusions are captured and distributed.

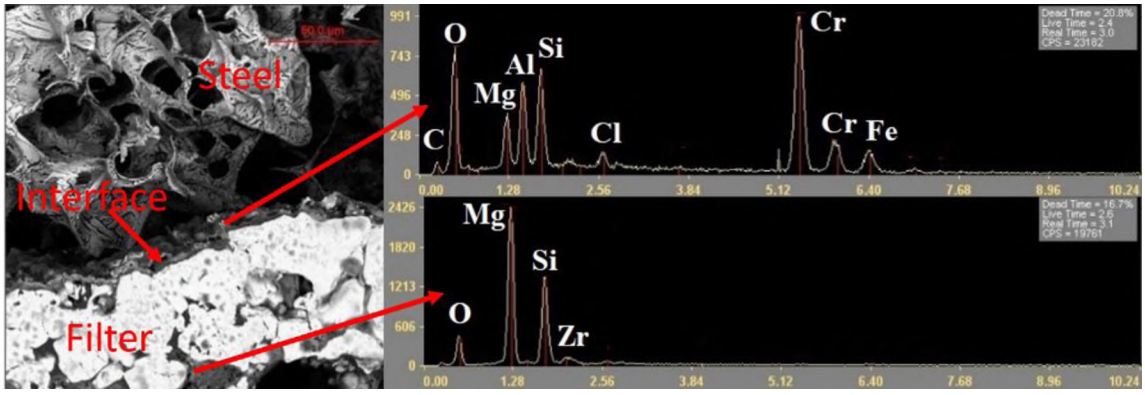

(a)

Figure 9. (a) Single capturing mechanism observed for solid alumina inclusions and (b) dual capturing mechanism observed for liquid manganese silicate inclusions.

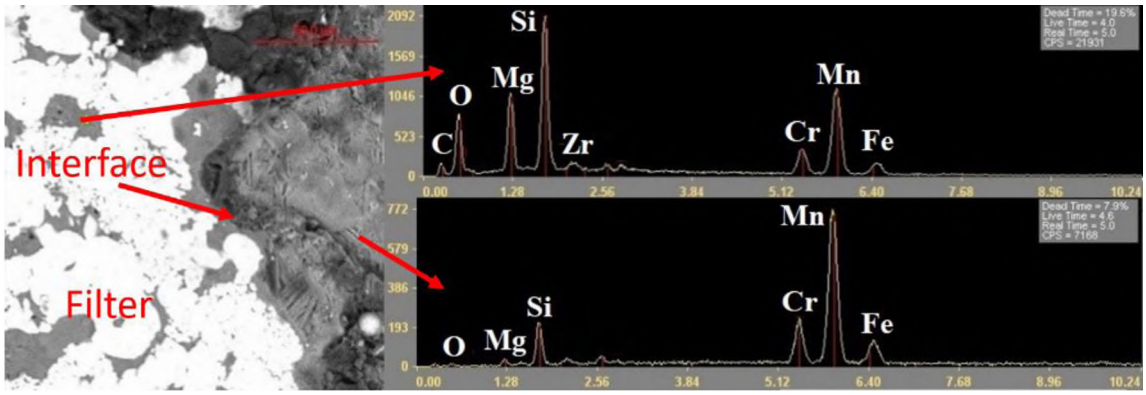

(b)

Figure 9. (a) Single capturing mechanism observed for solid alumina inclusions and (b) dual capturing mechanism observed for liquid manganese silicate inclusions (cont.).

Elemental maps of different areas of an unused filter sample were created to identify the elements present in the filter. During elemental mapping, as shown in Figure 10, presence of Zr, Si, Mg and O were found, which confirmed the presence of ZrO_2, SiO_2 and MgO in the filter. Mn was not detected as a filter element during these mappings and therefore it was mapped along with Zr for the filtration samples obtained from experiment 2 to track the manganese silicate content and distribution within the filter web micropores.

These mapped areas of Mn and Zr were used to determine the area (A) of manganese silicate and zirconia respectively. These areas were utilized to determine the area fraction (AF) of manganese silicate inclusions captured by zirconia filter using Equation 6.

$$AF_{MnO.SiO_2} = \frac{A_{MnO.SiO_2}}{A_{ZrO_2}} \times 100\% \quad (6)$$

During microscopic analysis of different filtration samples, it was noted that some of the micropores were filled with liquid inclusions while the others were empty. Therefore, an overall mapping of each filter web was required to quantify the amount of liquid inclusions captured in each sample. Each filtration sample was subdivided into 3-4 areas for carrying out the overall mapping at 25X magnification to scan individual web separately. All fifteen samples from three filters of experiment 2 were mapped and the area fractions of manganese silicate inclusions captured by the filter element were calculated. The distributions of the inclusion captured through the filter thickness are represented in Figure 11.

The distribution of captured liquid inclusions in the micropores decreased from entry to exit side (sample 1 to 5) for all three molds and distributions were consistent for all three filter samples. In literature, inclusion attachment kinetics are explained by a first order kinetics mechanism as represented in Equation 3 [8]. During the experimental trials, the distributions of the inclusion captured showed the similar exponential trend. Comparing the trend lines obtained from these distributions with Equation 3, the term (K_0Z/U_m) can be obtained. A value 0.6 was estimated for the conditions of our experiment.

The area fractions of liquid manganese silicate inclusions captured can further be utilized to obtain the filter micropore saturation (S) using Equation 7. Several scanning electron microscopic images of the unused filter samples were captured and processed with ImageJ software. It was determined that ~26-31% micropores were present on the zirconia filter element. This value was further used to find out the area fraction of zirconia filter to the micropores as 2.5±0.3, by basic mathematical conversion. The

distributions of filter micropore saturation with liquid inclusions for three molds are represented in Figure 12.

$$S = AF_{MnO.SiO_2} \times \frac{A_{ZrO_2}}{A_{micropores}} \quad (7)$$

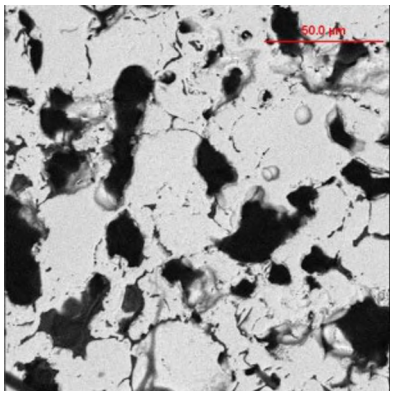

(a)

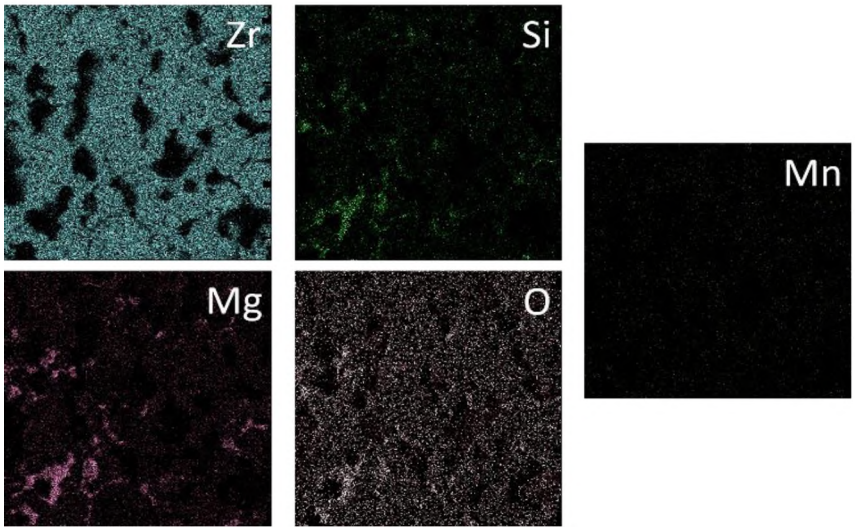

(b)

Figure 10. (a) A scanning electron microscopic image of an area of unused filter and (b) elemental maps of the same area showed the presence of Zr, Si, Mg and O as the filter elements.

Area fraction of the zirconia filter to the micropores was constant and therefore the filter micropore saturation was directly proportional to the area fraction of the manganese silicate inclusions captured by zirconia foam filter. As a result, a similar exponential trend was observed through the filter thickness. These distributions revealed that entry side of the filter micropores were filled more than at the exit side. However, a large portion of the micropore area in the filters was still empty after complete mold filling in this study. A higher inclusion loading or increased amount of metal can be filtered with the same magnesia stabilized zirconia filter used for this study. Future work is planned to determine the saturation level of these filter elements and to observe what occurs at 100% saturation.

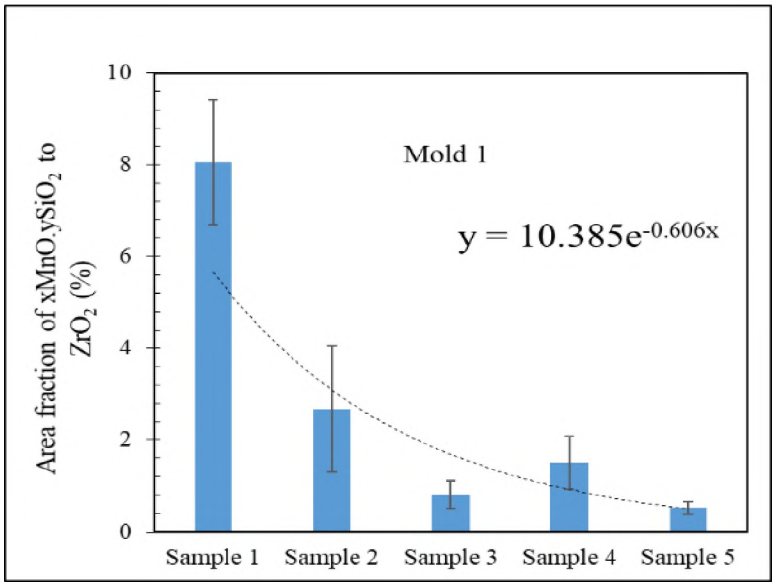

(a)

Figure 11. Distributions of area fraction of $xMnO.ySiO_2$ to ZrO_2 through the filter thickness for (a) mold 1, (b) mold 2 and (c) mold 3.

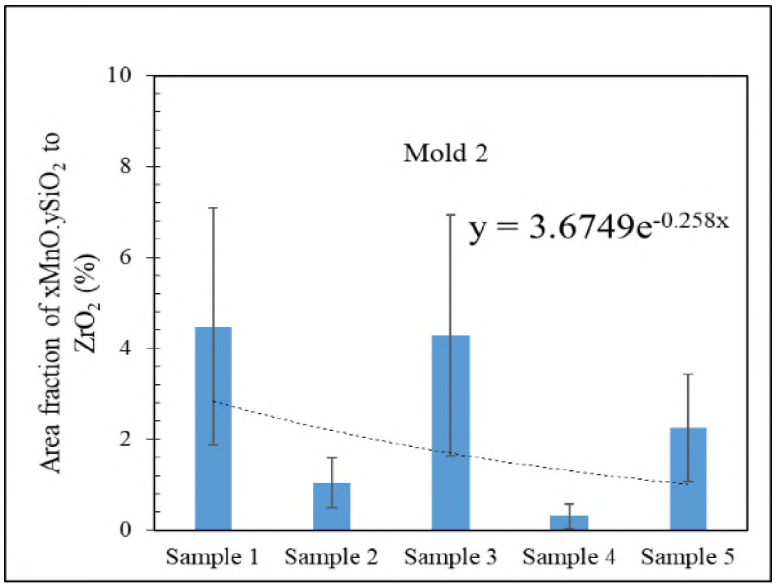

(b)

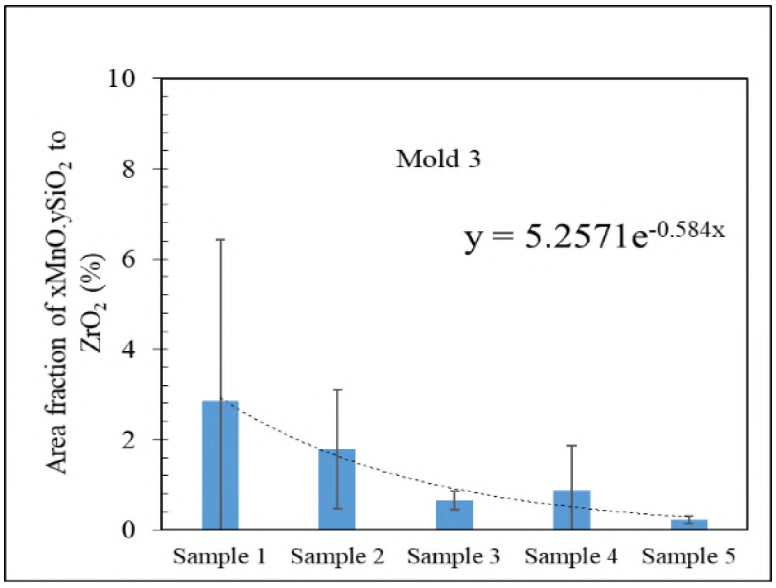

(c)

Figure 11. Distributions of area fraction of $xMnO.ySiO_2$ to ZrO_2 through the filter thickness for (a) mold 1, (b) mold 2 and (c) mold 3 (cont.).

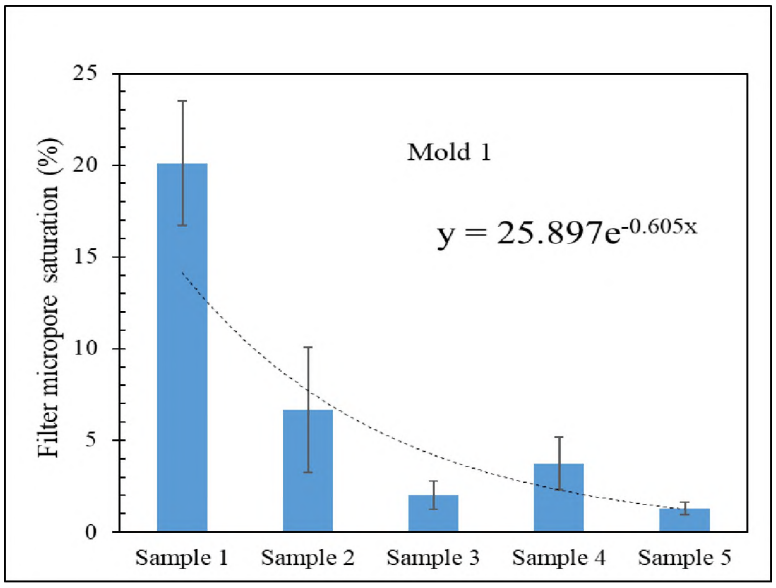

(a)

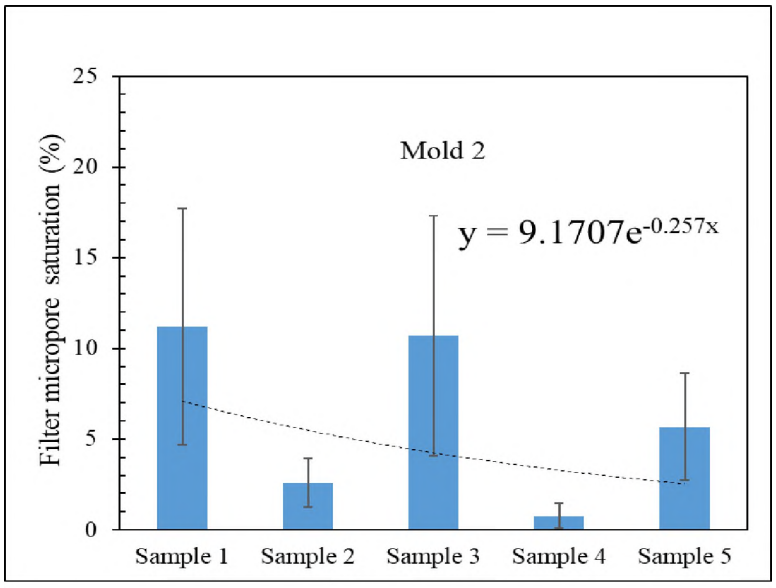

(b)

Figure 12. Distributions of filter micropore saturation with liquid inclusions through the filter thickness for (a) mold 1, (b) mold 2 and (c) mold 3.

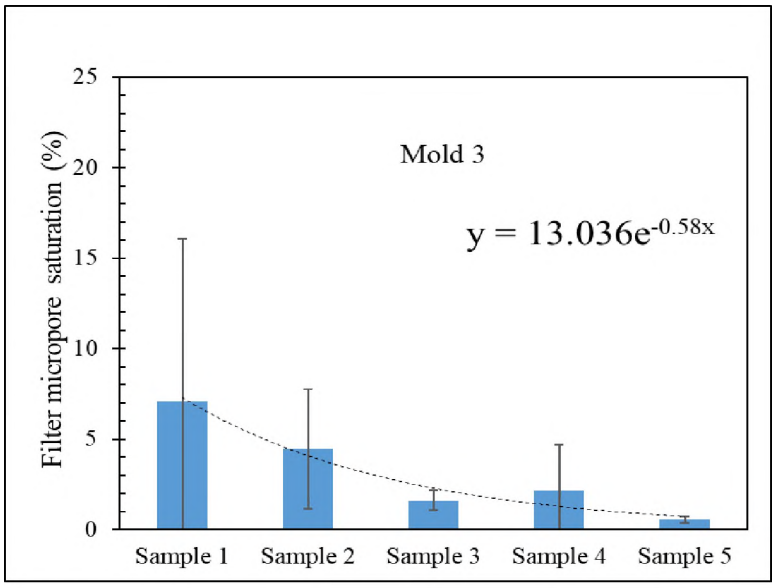

(c)

Figure 12. Distributions of filter micropore saturation with liquid inclusions through the filter thickness for (a) mold 1, (b) mold 2 and (c) mold 3 (cont.).

5. CONCLUSIONS

It is evident from this study that both solid and liquid inclusions are captured effectively by magnesia stabilized zirconia foam filters. The current study identified different capturing mechanisms for solid and liquid inclusions. From this study, the following conclusions can be drawn:

1. Solid alumina inclusions were captured mostly at the metal-filter interface and hence can be found at the close proximity of the interface region. However, liquid manganese silicate inclusions were mostly captured and held within the web micropore structure of the filter. The presence of liquid manganese silicate inclusions was also observed at the metal-filter interface in some samples.

2. Magnesia used to stabilize the zirconia in the filter reacted with the alumina inclusions present in the steel melt to form Mg-Al spinel and this further helped to capture the solid alumina inclusions.
3. The concentration of liquid inclusions in the filter micropores decreased from the entry side to the exit side of the filter. This distribution appears to obey first order kinetics and the value of the kinetic parameter was determined for the filter used in this study with liquid manganese silicate inclusions.
4. Cathodoluminescence can be a useful tool to identify and quantify the alumina inclusions captured by zirconia filters, and the interactions that occur between the filter and capture inclusions.

ACKNOWLEDGEMENT

Authors like to show their gratitude to the industry members of Peaslee Steel Manufacturing Research Center for the technical advice and financial support. Specials thanks go to Foseco and MetalTek International for providing materials to carry out the experiments. Authors also like to thank Todd Sander and Caelen Johnson for their help in sample preparation and acknowledge the suggestions from Dr. Jeffrey Smith, Dr. Simon Lekakh and Dr. Mingzhi Xu.

REFERENCES

1. W. Simmons, "Influence of Metal Filtration on the Production of High Integrity Cast Products", *Foundry Trade Journal*, January, p. 24 (1985).

2. D. Apelian, R. Mutharasan and S. Ali, "Removal of Inclusions from Steel Melts by Filtration", *Journal of Materials Science*, 20, p. 3501 (1985).

3. K. Raiber, P. Hammerschmid and D. Janke, "Experimental Studies on Al_2O_3 Inclusions Removal from Steel Melts Using Ceramic Filters", *ISIJ International*, 35(4), p. 380 (1995).

4. K. Janiszewski and Z. Kudlinski, "The Influence of Non-Metallic Inclusions Physical State on Effectiveness of the Steel Filtration Process", *Steel Research International*, 77(3), p. 169 (2006).

5. L. Aubrey, J. Schmahl and M. Cummings, "Application of Advanced Reticulated Ceramic foam filter Technology to Produce Clean steel Castings", *AFS Transactions*, 101, p. 59 (1993).

6. E. Kawecka-Cebula, Z. Kalicka and J. Wypartowicz, "Filtration of Nonmetallic Inclusions in Steel", *Archives of Metallurgy and Materials*, 51(2), p.261 (2006).

7. K. Uemura, M. Takahashi, S. Koyama and M. Nitta, "Filtration Mechanism of Non-metallic Inclusions in Steel by Ceramic Loop Filter", *ISIJ International*, 32(1), p. 150 (1992).

8. D. Apelian and R. Mutharasan, "Filtration: A Melt Refining Method", *Journal of Metals*, p. 14 (1980).

9. W. Su, T. Johnson, J. Day, J. Wallace and F. Li, "The Development and Characterization of Extruded Cellular-Ceramic Filters for Steel Foundry Applications", *AFS Transactions*, 96, p. 161 (1988).

10. MAGMASOFT® 5.3.0: https://www.magmasoft.com/en/

11. J. Campbell, "Complete Casting Handbook", Elsevier Ltd.: Oxford, UK (2011).

12. S. Chakraborty, R. O'Malley, L. Bartlett and M. Xu, "Efficiency of Solid Inclusion Removal from the Steel Melt by Ceramic Foam Filter: Design and Experimental Validation", *AFS Metalcasting Congress*, Fort Worth, TX, USA, 2018.

13. C. Tian, "On the Removal of Non-metallic Inclusions from Molten Steel through Filtration", PhD Dissertation: McGill University, Montreal, Quebec, Canada (1990).

14. S. Ali, R. Mutharasan and D. Apelian, "Physical Refining of Steel Melts by Filtration", *Metallurgical Transactions B*, 16B, p. 725 (1985).

15. R. Inoue, S. Ueda, T. Ariyama and H. Suito, "Extraction of Nonmetallic Inclusion Particles Containing MgO from Steel", *ISIJ International*, 51(12), p. 2050 (2011).

16. D. Janis, R. Inoue, A. Karasev and P. Jonsson, "Application of Different Extraction Methods for Investigation of Nonmetallic Inclusions and Clusters in Steels and Alloys", *Advances in Material Science and Engineering*, DOI: 10.1155/2014/210486 (2014).

17. O. Adaba, R. O'Malley, M. Xu, L. Bartlett and S. Lekakh, "Three-Dimensional Study of Inclusion Morphology and Size Distribution in Mn-Si Killed Steel", AISTech, Philadelphia, PA, USA, 2018.

18. FactSage™ 7.2: www.factsage.com

19. S. Lany, Band Structure Calculations for the 3d Transition Metal Oxides in GW, *Physical Review B*, 87, p. 085112-1 (2013).

III. CERAMIC FOAM FILTER MICROPORES AS SITES FOR LIQUID INCLUSION RETENTION

Soumava Chakraborty, Ronald J. O'Malley and Laura Bartlett

Peaslee Steel Manufacturing Research Center, Department of Materials Science and Engineering, Missouri University of Science and Technology, Rolla, MO, USA, 65409

ABSTRACT

In steel foundries, ceramic filters are often used to capture non-metallic inclusions. It is well documented that solid inclusions are captured and retained at the metal-filter interface within the filter macropores at the steel-refractory interface. However, liquid inclusions appear to be captured and retained by two mechanisms: one within the filter web micropore structure and another as a liquid film at the metal-filter macropore interface. Experiments were carried out to study the removal of various non-metallic liquid inclusions by magnesia-stabilized zirconia filters. The results documented the effective removal of liquid inclusions in all experiments. Samples were extracted from filter element to investigate the inclusion attachment mechanism during the deep bed filtration. Energy dispersive X-ray spectroscopy (EDS), associated with a scanning electron microscope (SEM), was employed to evaluate the inclusion attachment mechanism with the ceramic filters. Liquid inclusion retention in the filter micropores followed an exponential trend from entry to exit side of the filter, until the micropores became completely saturated. After complete saturation, the retained inclusion distribution remained constant through the thickness of the filter. Open micropores in two different types of filters were found to capture the liquid inclusions drawing them into the

micropores due to inclusion-refractory favorable wetting conditions. Once the accessible micropores were fully saturated, a liquid inclusions film developed at the metal-filter macropore interface, increasing the possibility for the release of large liquid inclusions from the filter.

Keywords: steel, non-metallic inclusions, filter micropores, filtration, removal kinetics, capturing mechanism

1. INTRODUCTION

Molten steel contains varying amount of dissolved oxygen depending on the steel grade and due to the low solubility of the dissolved oxygen, it reacts with the carbon present in steel to form carbon monoxide gas. The formation of carbon monoxide creates blowholes in the casting. These defects are undesirable and reduce the quality of the castings [1-3]. Deoxidation of molten steel is thereby important in steelmaking practices to remove the dissolved oxygen. In the steel industry, different types of deoxidizers, such as, aluminum, silicon, manganese, calcium, titanium, and/or a combination of ferroalloys containing these deoxidants are mostly used [4]. These deoxidizers react with dissolved oxygen present in liquid metal and form oxide inclusions. Removal of these oxide inclusions is essential to the quality and appearance of the castings, as these oxides can reduce mechanical properties, impact machinability, produce surface defects and increase scrap rates [5].

In foundry steelmaking, steel melt filtration is a common practice for removal of primary deoxidation and endogenous oxide inclusions [6-9]. Ceramic filters can be of

different types according to their compositions, but magnesia-stabilized zirconia filters are most commonly employed due to their excellent chemical and mechanical stabilities at steelmaking temperatures [11]. Many types of ceramic filters exist m, such as loop filters, multi-hole filters, monolithic filters, foam filters, etc. [10,12,13]. Removal of both solid and liquid non-metallic inclusions using these filters has been reported by several authors [10, 13-15]. Removal efficiency (η) of these non-metallic inclusions can be defined by Equation (1), where C_i and C_o are the concentrations of inclusions in the steel melt at filter inlet and at filter outlet respectively [10, 13].

$$\eta = \left(\frac{C_i - C_o}{C_i}\right) \times 100\% \quad (1)$$

Non-metallic inclusions are typically much smaller than the ceramic filter pore size and therefore are removed from the steel by a deep bed filtration mechanism [10, 14, 16, 17]. In one publication, the size of the non-metallic liquid inclusions and interfacial energy and wetting angle between the non-metallic liquid inclusions and the ceramic filter were identified as the main contributing factors for inclusion attachment [13]. A previous study by the authors showed that liquid manganese silicate inclusions are captured both in micropores in the web structure of the ceramic filter as well as at the metal-filter macropore interface [18]. However, this observation was not tested for other classes of non-metallic liquid inclusions. In this study, a previously designed mold by the authors was used to study the filtration efficiency, inclusion attachment mechanism, and distribution of non-metallic inclusions through filter thickness for liquid manganese silicate and calcium aluminate inclusions [19]. An industrial scale experiment was also carried out using a larger volume of filtered steel to observe changes in the distribution of

captured liquid inclusions throughout the filter thickness at higher levels of inclusion loading in the filter.

2. EXPERIMENTAL PROCEDURE

Two laboratory-scale experiments were conducted to filter liquid manganese silicate and calcium aluminate inclusions from SS 316 melt using magnesia-stabilized zirconia foam filter. A coreless 200lb (~90kg) induction furnace was used for melting the charge materials (~80kg). After complete melting, the furnace was covered with argon (at $1.1X10^5 mm^3/s$ flow rate). In Experiment 1, a mixture of FeSi and FeMn was used to generate manganese silicate inclusions. 90% of these two ferro-alloys were added to the furnace to allow their melting and generate inclusions. During tapping, the remaining 10% of the deoxidizer addition was added to the metal stream to generate manganese silicate inclusions late in the process. In Experiment 2, Al was directly added to the metal stream during tapping to generate alumina inclusions. These solid alumina inclusions were later treated with Ca wire to generate liquid calcium aluminate inclusions.

A 200lb (~90kg) teapot-style ladle was used to pour steel sequentially into three molds. The purpose of using the same heat to pour three different molds, as shown in Figure 1(a), was to ensure the consistent steel chemistry in those molds at different times after deoxidation. The metal entering the first mold contained the liquid from the bottom of the ladle, metal entering the second mold contained the liquid from the middle and metal entering the third mold contained the liquid from the top of the ladle. Hence, the chance of reoxidation was the maximum for the third mold due to higher ladle holding

time. Final chemistry samples for both experiments were collected and pouring temperatures were measured before pouring the liquid steel into the first mold in each experiment. Table 1 represents the nomenclature and details of the filters used in these experiments and the experimental parameters are represented in Table 2.

Table 1. Filter nomenclature and details.

Experiment Number	Number of molds	Ladle utilized	Filters per mold	Ladle nomenclature	Mold nomenclature	Filter nomenclature
1	3	1	1	Ladle 1	Mold 1.1	Filter 1.1
					Mold 1.2	Filter 1.2
					Mold 1.3	Filter 1.3
2	3	1	1	Ladle 2	Mold 2.1	Filter 2.1
					Mold 2.2	Filter 2.2
					Mold 2.3	Filter 2.3
3	1	2	2	Ladle 3.1	Mold 3	Filter 3.1
				Ladle 3.2		Filter 3.2

During the industrial-scale experiment (Experiment 3), 1633kg of charge material was melted in a 4000lb (1814kg) induction furnace to produce SS 321LC. After melting, liquid steel was tapped into two 2000lb (907kg) ladles. 4.1kg of CaSiBa deoxidizer was kept at the bottom of each teapot-style ladle before pouring the molten steel. From the induction furnace Ladle 3.1 and Ladle 3.2 were poured sequentially. After deoxidation, both ladles were moved to the pouring station, pouring temperatures were measured, and molten steel was poured from two ladles simultaneously into a 3.2m x 1.575m x 1.675m mold. Two pouring cups located at the top surface of the mold, as shown in Figure 1(b),

were connected to two rigging systems. In all these experiments, 100mm x 100mm x 25mm, 10ppi, magnesia-stabilized zirconia foam filters were used, as shown in Figure 1(c). The first ladle (Ladle 3.1) was used to pour molten steel through Filter 3.1 and the second ladle (Ladle 3.2) was used pour molten steel through Filter 3.2. Pouring temperatures were measured from Ladles 3.1 and 3.2 before pouring the liquid steel into the mold.

Table 2. Experimental parameters.

Experiment number	Metal passing through each filter (kg)	Tapping temperature (°C)	Pouring temperature (°C)	Filter used	Pouring time (s)
1	7	1643	1550 (Ladle 1)	Filter 1.1	15
				Filter 1.2	12
				Filter 1.3	14
2	7	1637	1545 (Ladle 2)	Filter 2.1	16
				Filter 2.2	14
				Filter 2.3	17
3	821	1702	1566 (Ladle 3.1)	Filter 3.1	61
			1580 (Ladle 3.2)	Filter 3.2	58

3. SAMPLE PREPARATION

Optical emission arc spectrometer (FOUNDRY MASTER- OXFORD INSTRUMENTS) was utilized to determine the chemistry of the steel samples. To accurately measure C, S, and O, N, LECO combustion methods (CS 600 and TC 500)

were utilized. Samples were prepared equidistant from the entry and exit side surfaces of the filters (10mm from the filter surfaces from entry and exit sides) in the runner, termed as filter inlet and outlet. The total oxygen content of filter inlet and outlet samples were measured using LECO combustion method (TC 500). Based on the total oxygen contents, filtration efficiency for all the filters used can be calculated using Equation (2), where, O_{in} is total oxygen content at filter inlet (%) and O_{out} is total oxygen content at filter outlet (%).

$$\eta = \frac{(O_{in} - O_{out})}{O_{in}} \times 100\% \quad (2)$$

Samples were further sectioned from filter inlets and outlets, bakelite mounted, and polished using standard metallographic methods. Inclusion characterization was carried out using SEM/EDS instrument (ASPEX PICA 1020) with automated feature analysis (AFA). Size, shape and nominal chemistry of the inclusions were recorded for all the samples at 200X and 1000X magnifications, and the results were combined to record the entire inclusion size range (0.5-80.0μm) present in the samples. The entire sample area was scanned (~120mm^2) for each sample at 200X magnification, whereas at 1000X magnification a randomized statistical method (software in-built) was utilized to analyze the entire sample area. The size distribution analyses, and filtration efficiency calculations were performed based on these statistical measurements. Filtration efficiency was calculated using Equation (3), where, A_{in} is inclusion area fraction at filter inlet (ppm) and A_{out} is inclusion area fraction at filter outlet (ppm).

$$\eta = \frac{(A_{in} - A_{out})}{A_{in}} \times 100\% \quad (3)$$

(a)

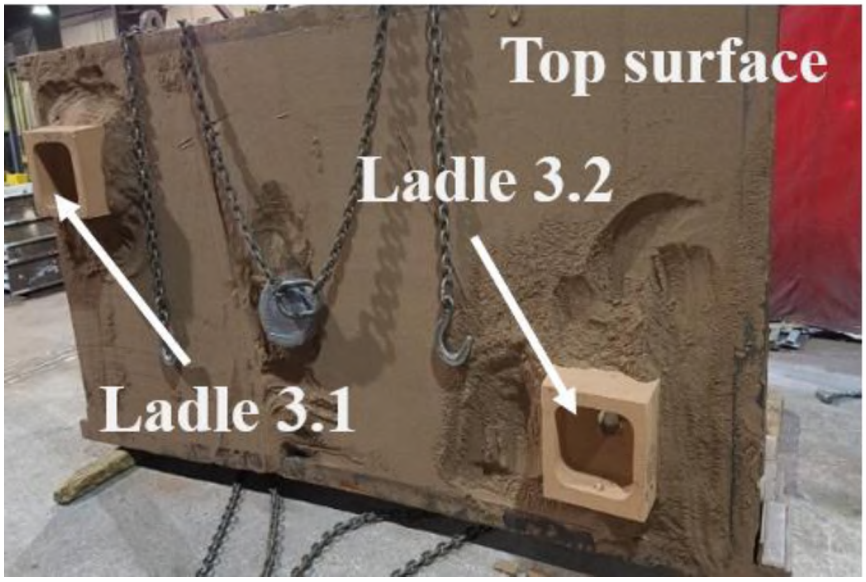

(b)

Figure 1. (a) Three mold sets used for laboratory-scale experiments (Experiments 1 and 2), (b) top surface of the mold used in industrial-scale experiment (Experiment 3) showing two pouring cups used for two different ladles, and (c) magnesia-stabilized zirconia 10ppi foam filter used in all three experiments.

(c)

Figure 1. (a) Three mold sets used for laboratory-scale experiments (Experiments 1 and 2), (b) top surface of the mold used in industrial-scale experiment (Experiment 3) showing two pouring cups used for two different ladles, and (c) magnesia-stabilized zirconia 10ppi foam filter used in all three experiments (cont.).

Samples were also sectioned directly from the filter to study the inclusion attachment mechanism and removal kinetics. Samples directly obtained from the central area of the filters (area marked in blue), as represented in Figure 2(a), were epoxy mounted under vacuum to prevent the air bubble formation, to preserve any deposits and to penetrate any pores in the sample. These samples were further cut into five smaller sections (~5mm wide each) using a diamond sectioning blade. These filter samples (S1-5) were then remounted with epoxy, polished, and coated with Au/Pd for characterizing in SEM. Elemental maps were created for 3-4 scanning areas of each samples (S1-5) at 25X magnifications to find out the inclusion attachment mechanism with the filter and

the distribution of saturated filter micropores through the filter thickness, as shown in Figure 2(b).

4. RESULTS

The final chemistry of the steel obtained from Experiment 1 is represented in Table 3. A thermodynamic analysis was carried out with this steel chemistry using FactSage 7.2 [20] to confirm the formation of liquid manganese silicate ($MnO.SiO_2$) inclusions at steelmaking temperatures. The samples were observed at different magnifications in manual mode using the SEM/EDS analysis. Spherical inclusions of different sizes and different nominal chemistries were observed for all the filter inlet and outlet samples. Figure 3 represents the liquid $MnO.SiO_2$ inclusions formed along with some minor constituents such as Al_2O_3, Cr_2O_3, CaO, MnS, etc.

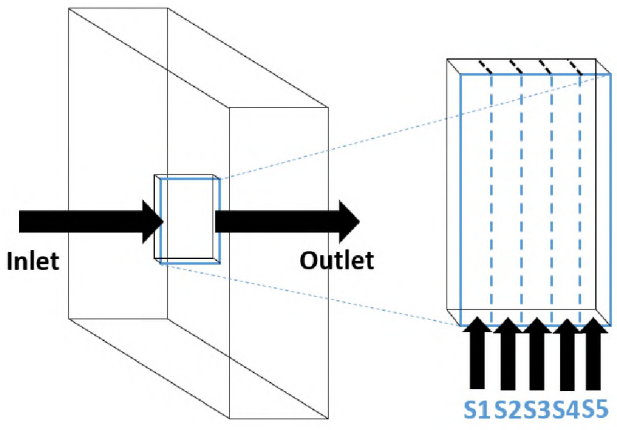

(a)

Figure 2. (a) Sectioning method to prepare samples directly from the filters and (b) method for elemental mappings of the filtration samples.

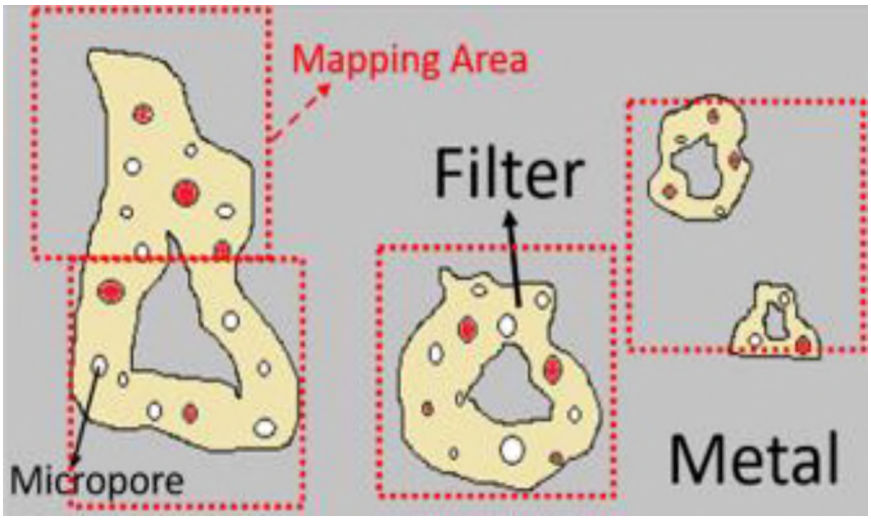

(b)

Figure 2. (a) Sectioning method to prepare samples directly from the filters and (b) method for elemental mappings of the filtration samples (cont.).

Table 3. Final steel chemistry for Experiment 1.

C	Si	Mn	Al	Cr	Ni	Mo	Cu	Ca	N	S	O	Fe
0.018	0.57	1.29	0.003	17.41	8.20	2.41	0.001	0.0005	0.015	0.0008	0.0237	Bal.

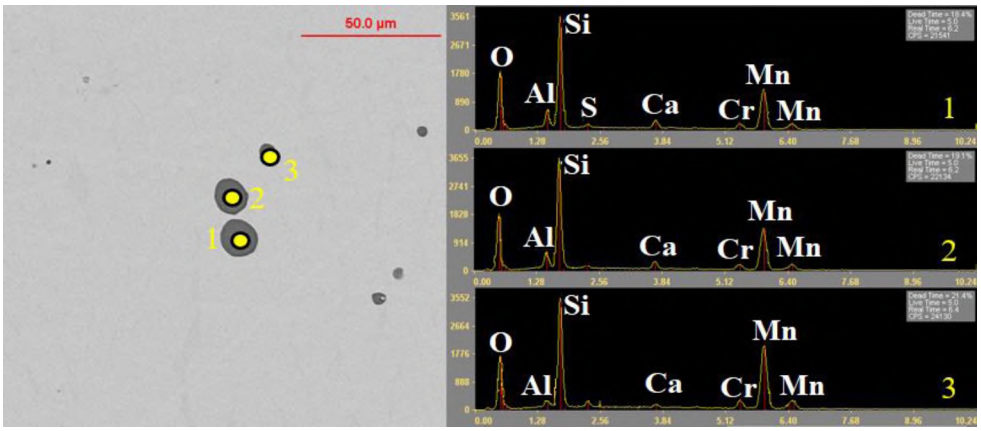

Figure 3. Spherical $MnO.SiO_2$ inclusions generated during Experiment 1.

The final chemistry obtained from Experiment 2 is shown in Table 4. The chemistry sample was collected from the middle of the ladle. Due to higher vapor pressure, the recovery of calcium was poor in the molten steel at steelmaking temperatures and hence the Ca content shown here may not be representative of the value for all the molds poured during this experiment. Therefore, thermodynamic software was not utilized here to confirm the formation of liquid inclusions. However, spherical calcium aluminate inclusions were observed in all the mold samples (Mold 2.1, 2.2 and 2.3), , as shown in Figure 4.

Table 4. Final steel chemistry for Experiment 2.

C	Si	Mn	Al	Cr	Ni	Mo	Cu	Ca	N	S	O	Fe
0.017	0.98	0.55	0.079	19.11	9.21	2.45	0.045	0.0013	0.017	0.0083	0.0283	Bal.

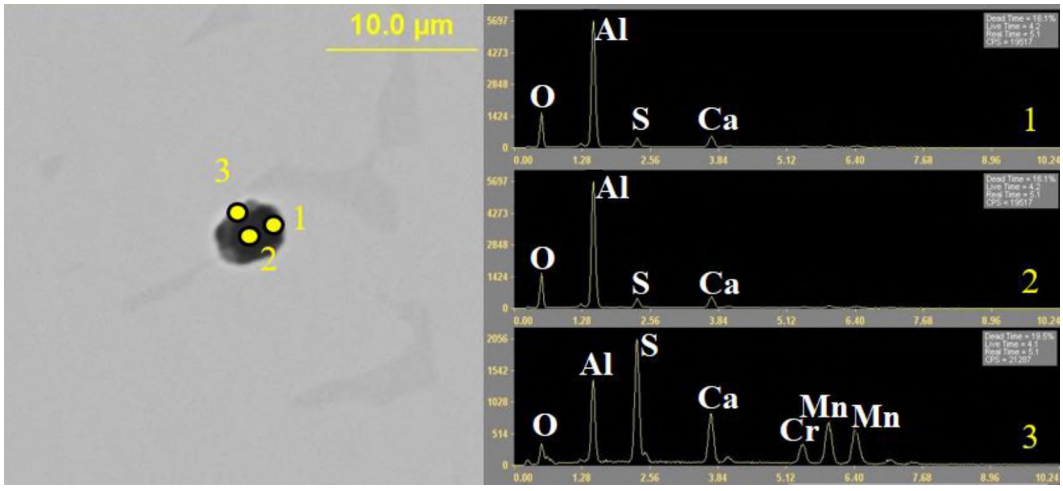

Figure 4. Spherical $CaO.Al_2O_3$ inclusions generated during Experiment 2.

To determine the physical state of the inclusions formed at different molds during Experiment 2, ternary diagrams are plotted. Inclusions from filter inlets of three molds (2.1, 2.2 and 2.3) are represented in Figure 5. It can be identified that only in Mold 2.3, semi-liquid inclusions were formed (region marked with dotted blue line), whereas in other two molds (2.1 and 2.2), only solid calcium aluminate inclusions were generated [21]. This may be due to the high vapor pressure of Ca at steelmaking temperatures and the difficulty in penetrating the Ca wire deep in the ladle, which more effectively treated the top part of the ladle.

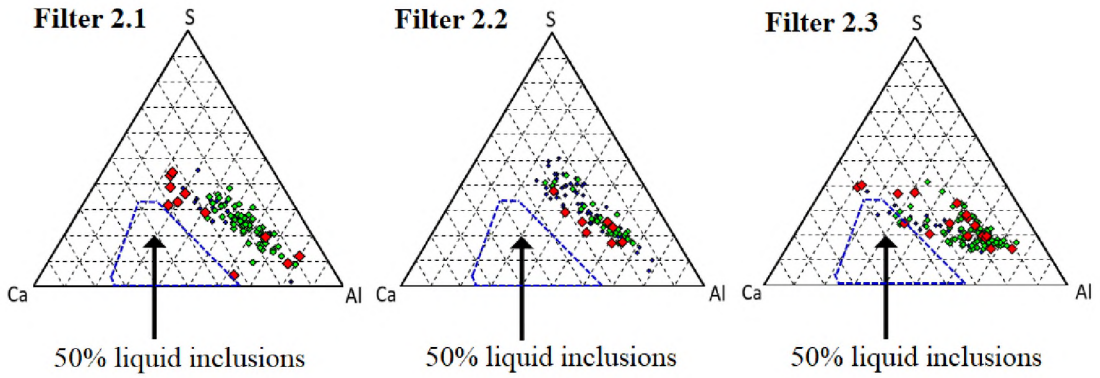

Figure 5. Ternary diagram obtained from characterizing filter inlet samples using AFA showed semi-liquid inclusions formed only in Mold 2.3 during Experiment 2.

The final chemistry obtained from Experiment 3 is presented in Table 5. During this industrial-scale experiment, multiple alloying elements were added to achieve the customers' requirements. Hence, complex inclusions were generated as shown in Figure 6. Thermodynamic analysis using FactSage 7.2 [20] confirmed the formation of complex liquid inclusions along with some Zr-rich solid phase deposited on those inclusions, as represented in Figure 6.

Table 5. Final steel chemistry for Experiment 3.

C	Si	Mn	Cr	Ni	Al	Mo	Co	Cu	Nb
0.0244	1.51	0.61	19.55	9.54	0.0079	0.1423	0.0930	0.1425	0.2610
W	**V**	**Ti**	**Zr**	**N**	**S**	**P**	**O**	**Ca**	**Fe**
0.0598	0.0464	0.0081	0.0072	0.0466	0.0034	0.0118	0.0361	0.0013	Bal.

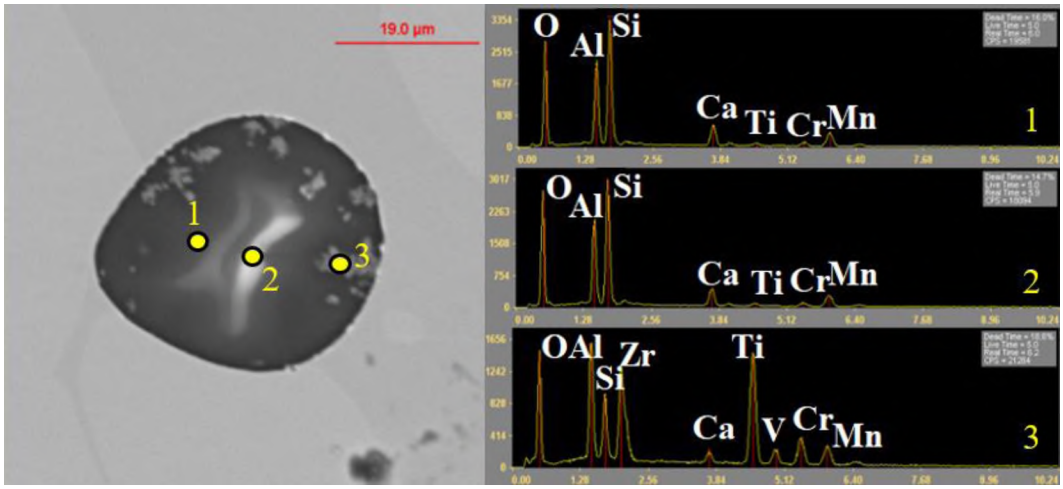

Figure 6. Spherical complex liquid inclusions generated during Experiment 3.

Inclusions were filtered effectively during all the three experiments, as shown in Figure 7. It was observed that in Experiments 1 and 2, Molds 1.3 and 2.3 (Filter 1.3 and 2.3 inlets) showed the highest total oxygen contents compared to the other molds. This is likely due to the reoxidation of steel melt at the top part of the ladles in both experiments. Also, these two molds showed the highest filtration efficiencies compared to the other two molds, as filtration efficiency is directly related to the initial inclusion concentration, which was demonstrated in a previous study of the authors [19]. In Experiment 3, total oxygen content for Filter 3.1 inlet was higher than Filter 3.2 inlet due to longer ladle

holding time of the first ladle (770s for Ladle 3.1) compared to the second one (647s for Ladle 3.2). Hence, chance of reoxidation of steel melt from Ladle 3.1 was higher compared to Ladle 3.2. Again, filtration efficiency for Filter 3.1 was higher compared to that of Filter 3.2 due to higher initial inclusion concentration.

Inclusion size distribution analyses were carried out for filter inlet samples obtained from all these experiments, presented in Figure 8. In laboratory-scale experiments (Experiments 1 and 2), the third molds poured (Molds 1.3 and 2.3) all contained larger inclusions and higher inclusion area fractions due to higher chance of reoxidation at the top of the ladle (Ladles 1 and 2), as shown in Figure 7(a) and (b). Similarly, in the industrial scale experiment (Experiment 3), Filter 3.1 inlet showed higher inclusion area fraction and formation of some very large inclusions (>40μm) due to a longer ladle holding time, as observed in Figure 7(c).

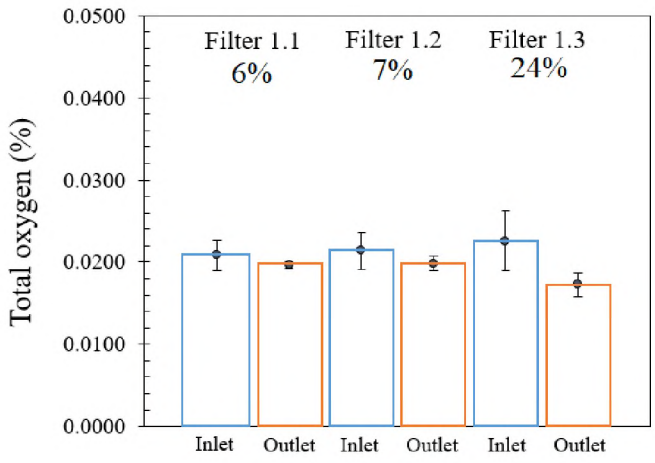

(a)

Figure 7. Filtration efficiency calculated by comparing total oxygen contents of filter inlets and outlets for: (a) Experiment 1, (b) Experiment 2 and (c) Experiment 3.

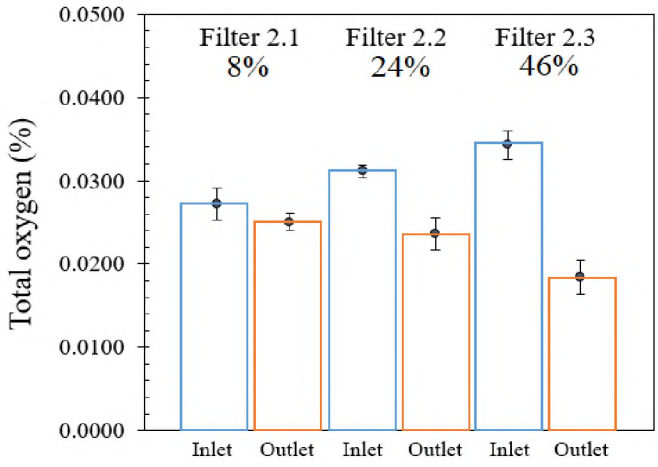

(b)

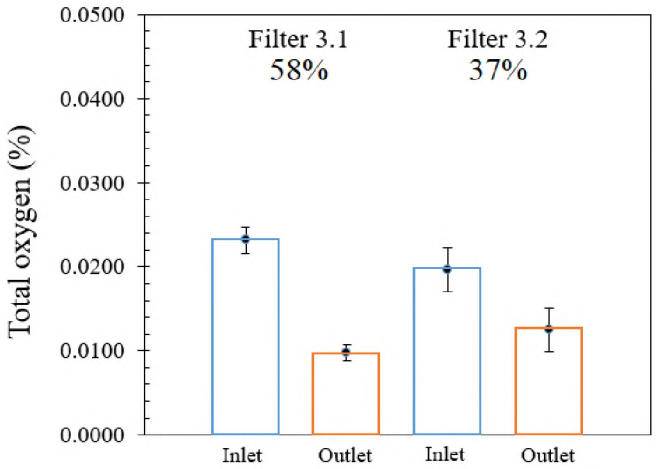

(c)

Figure 7. Filtration efficiency calculated by comparing total oxygen contents of filter inlets and outlets for: (a) Experiment 1, (b) Experiment 2 and (c) Experiment 3 (cont.).

Inclusion size distribution analyses were also carried out for all the filter inlet and outlet samples, as shown in Figure 9, to identify the effect of inclusions size on filtration efficiency. During this analysis, filtration efficiencies were also calculated and compared with that obtained from total oxygen content method. The results obtained from both

these methods were very much comparable. For most of the cases, larger inclusions (>5µm) were found to be more effectively filtered compared to the smaller ones.

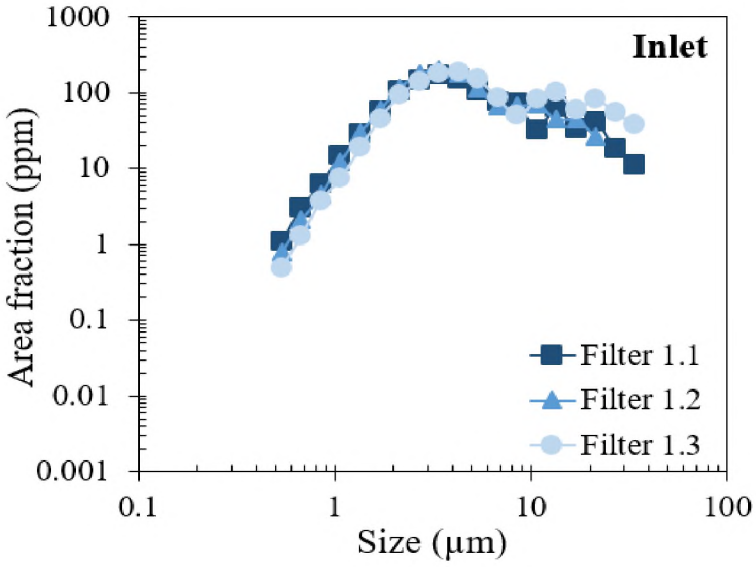

(a)

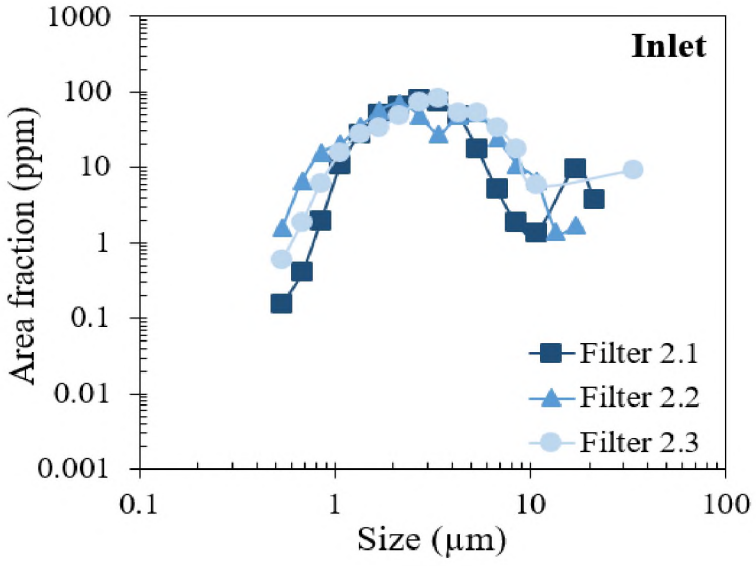

(b)

Figure 8. Size distribution analysis of inclusions area fractions for filter inlet positions for (a) Experiment 1, (b) Experiment 2 and (c) Experiment 3.

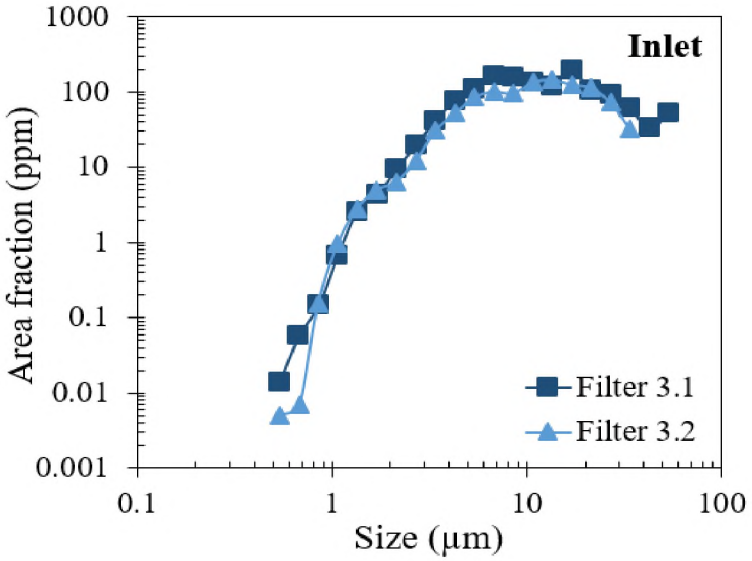

(c)

Figure 8. Size distribution analysis of inclusions area fractions for filter inlet positions for (a) Experiment 1, (b) Experiment 2 and (c) Experiment 3 (cont.).

5. DISCUSSION

In this current study, samples prepared directly from each filter were characterized using SEM/EDS. All the filtration samples were manually mapped using EDS analysis, and the liquid inclusions were observed to be captured within the open micropores of the filter webs. In Experiment 1, liquid manganese silicate inclusions were captured in the filter micropores, as shown in Figure 10(a), and from visual inspection it was found that the percentage of filled micropores decreased from entry to exit side of Filters 1.1, 1.2 and 1.3. In Experiment 2, filter open micropores were empty for Filters 2.1 and 2.2, because the solid calcium aluminate inclusions were not able to penetrate the filter micropores. However, Filter 2.3 was effective in capturing some liquid calcium

aluminate in the filter open micropores despite the fact that these inclusions were semi-solid, as shown in Figure 10(b). In this experiment number of filled micropores decreased from entry to exit side of the filter as well. In Experiment 3, complex liquid inclusions were observed both in the filter micropores as well as at the metal-filter macropore interface and most of the micropores were found to be filled, as shown in Figure 10(c). In all these experiments, molten steel can pass through the large filter macropores but cannot penetrate the small micropores due to high contact angle of steel with the zirconia filter surface (>90°) [22].

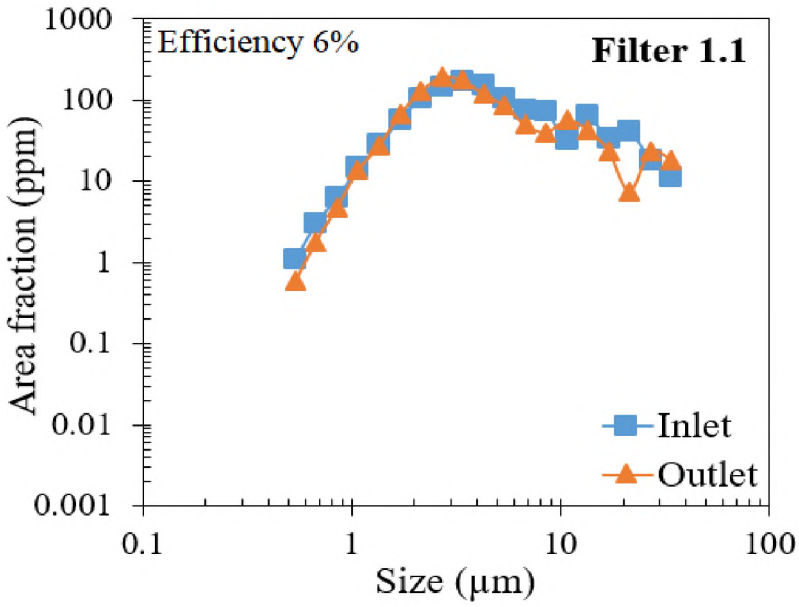

(a)

Figure 9. Size distribution analysis of inclusions area fractions for filter inlet and outlet positions and calculated filtration efficiency for (a) Filter 1.1, (b) Filter 1.2, (c) Filter 1.3, (d) Filter 2.1, (e) Filter 2.2, (f) Filter 2.3, (g) Filter 3.1 and (h) Filter 3.2.

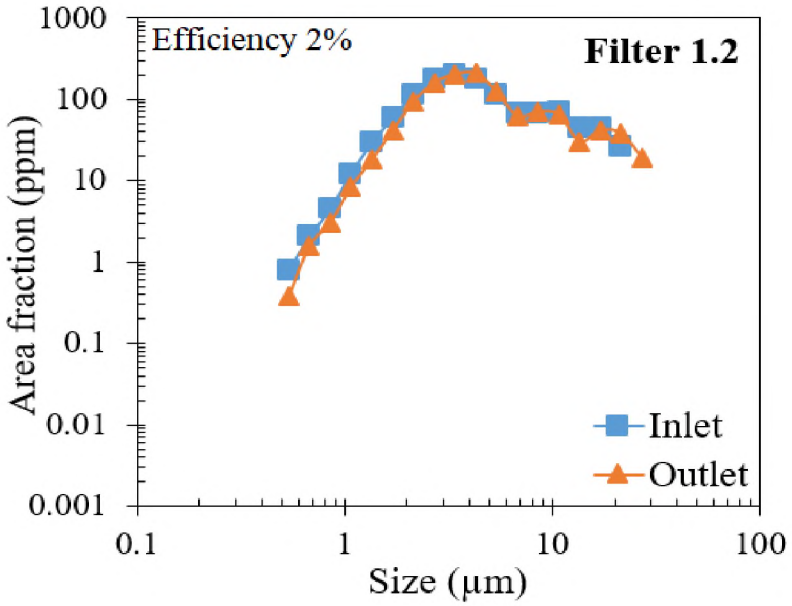

(b)

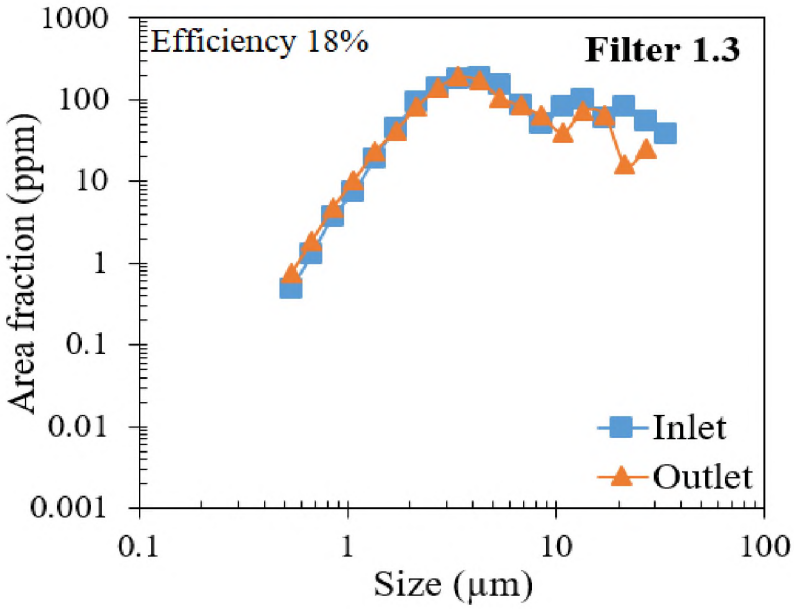

(c)

Figure 9. Size distribution analysis of inclusions area fractions for filter inlet and outlet positions and calculated filtration efficiency for (a) Filter 1.1, (b) Filter 1.2, (c) Filter 1.3, (d) Filter 2.1, (e) Filter 2.2, (f) Filter 2.3, (g) Filter 3.1 and (h) Filter 3.2 (cont.).

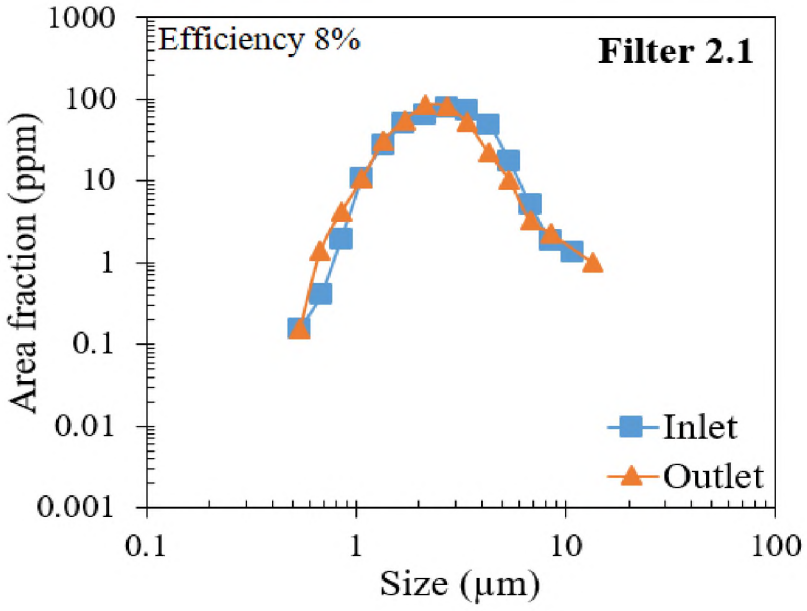

(d)

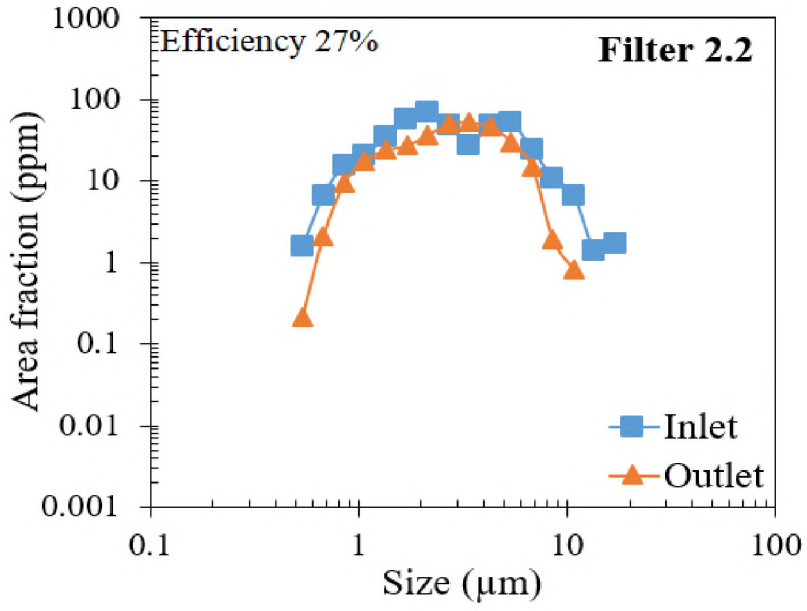

(e)

Figure 9. Size distribution analysis of inclusions area fractions for filter inlet and outlet positions and calculated filtration efficiency for (a) Filter 1.1, (b) Filter 1.2, (c) Filter 1.3, (d) Filter 2.1, (e) Filter 2.2, (f) Filter 2.3, (g) Filter 3.1 and (h) Filter 3.2 (cont.).

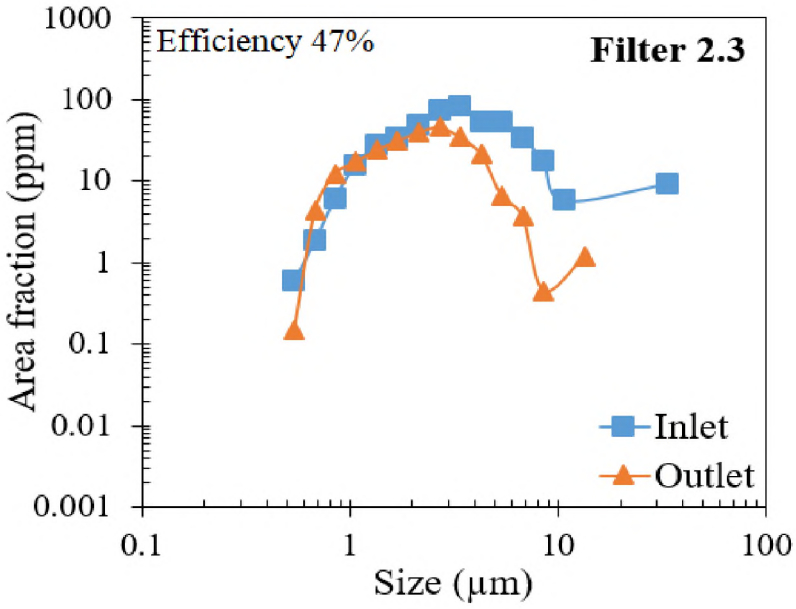

(f)

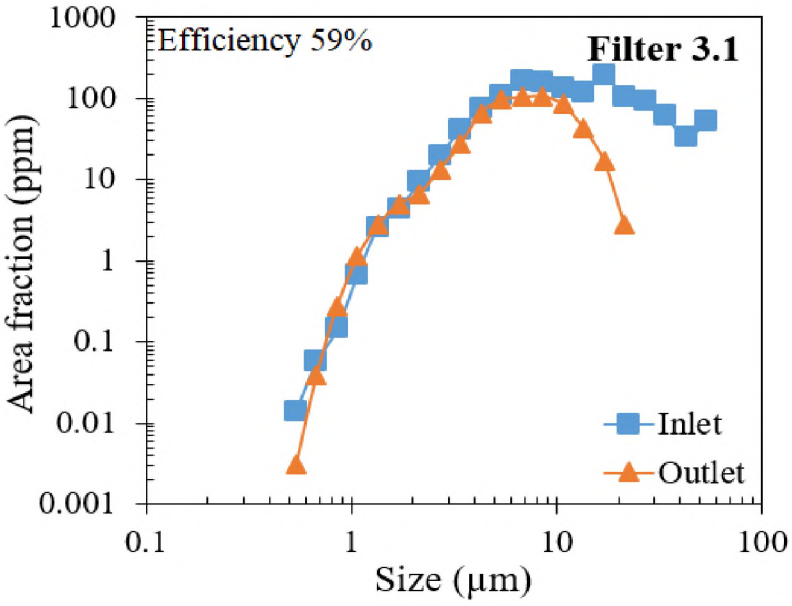

(g)

Figure 9. Size distribution analysis of inclusions area fractions for filter inlet and outlet positions and calculated filtration efficiency for (a) Filter 1.1, (b) Filter 1.2, (c) Filter 1.3, (d) Filter 2.1, (e) Filter 2.2, (f) Filter 2.3, (g) Filter 3.1 and (h) Filter 3.2 (cont.).

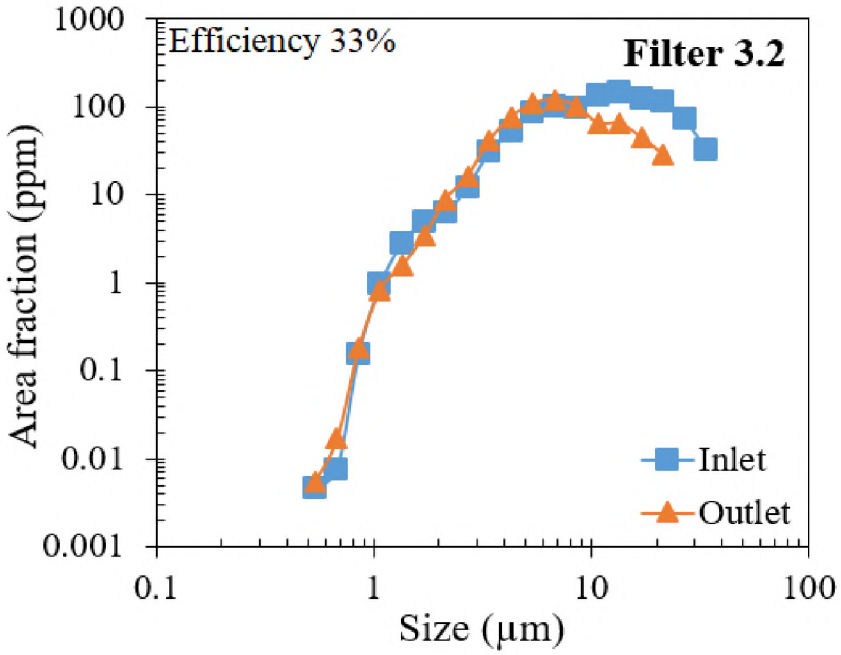

(h)

Figure 9. Size distribution analysis of inclusions area fractions for filter inlet and outlet positions and calculated filtration efficiency for (a) Filter 1.1, (b) Filter 1.2, (c) Filter 1.3, (d) Filter 2.1, (e) Filter 2.2, (f) Filter 2.3, (g) Filter 3.1 and (h) Filter 3.2 (cont.).

In a previous study by Janiszewski et al., it was reported that the liquid inclusions are captured at the metal-filter macropore interface [13], while a recent finding by the authors demonstrated that liquid manganese silicate inclusions were also captured at the filter micropores [18]. Foam filters exhibit this newly discovered capturing mechanism of liquid inclusions because of the low contact angle (<90°) of liquid inclusions with the zirconia filter surface [22]. High wettability of these non-metallic liquid inclusions helped them to be drawn into the ceramic filter micropores due to the interfacial tension forces.

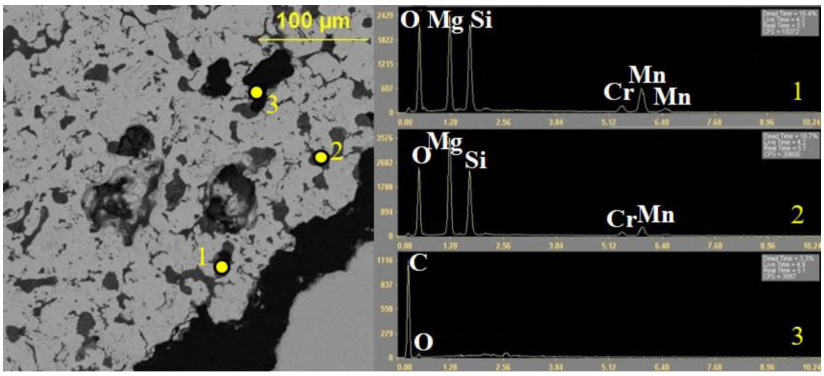

(a)

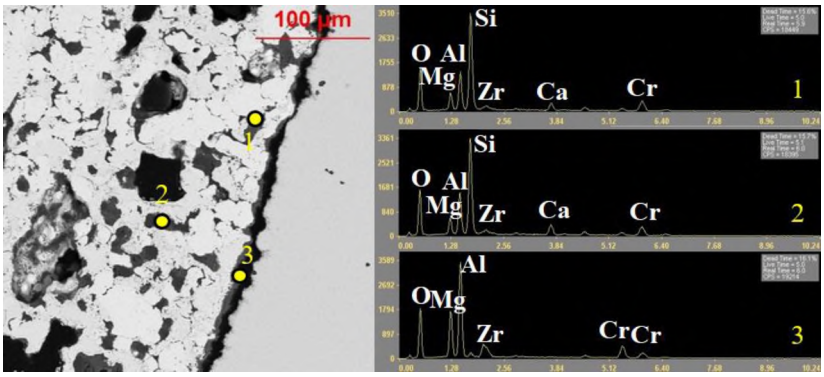

(b)

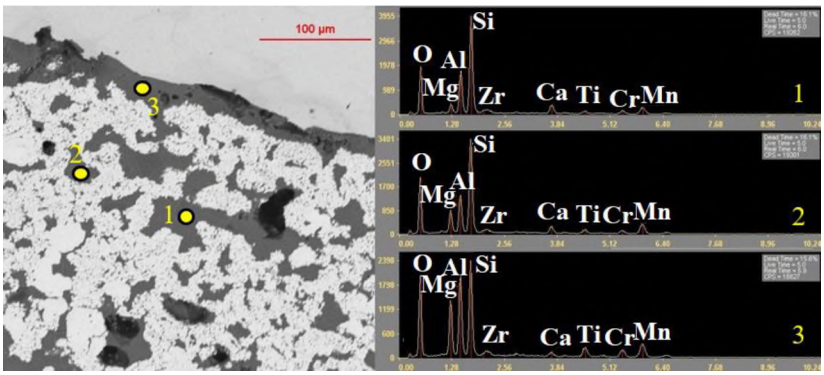

(c)

Figure 10. (a) Liquid manganese silicate inclusions were captured at the filter open micropores, (b) semi-liquid calcium aluminate inclusions were captured at filter open micropores, whereas alumina embedded in calcium aluminate reacts with magnesia to form spinel at the metal-filter macropore interface, and (c) complex liquid inclusions from Experiment 3 saturated the filter open micropores due to high inclusion loading, followed by an inclusion built up at metal-filter macropore interface.

To quantify the percent micropore saturation for each filtration sample from all three experiments, a two-step method has been utilized. In the first step, Archimedes' principle was applied to determine percent open micropores of magnesia-stabilized zirconia 10ppi foam filter samples [23]. The calculated value of open micropore was 25.5±2.8%. Using simple mathematical calculation, this percent open micropores was converted into the area ratio of zirconia to open micropores. In the second step, elemental maps were created for an unused filter sample. Mn and Ca were not found as the filter constituent elements and therefore these two can be implemented as the tracer elements for the liquid inclusions consisting of MnO and CaO respectively. Mn was used as a tracer element for the filters obtained from Experiment 1 and 3, whereas Ca was used for the filters obtained from Experiment 2. A representative image of mapping Mn and Zr for a selected area of a filtration sample is shown in Figure 11. Combining the results obtained from these two steps, micropore saturation (S) was calculated as represented by Equation (4).

$$S = \frac{A_{ZrO_2}}{A_{open\ micropores}} \times \frac{A_{liquid\ inclusions}}{A_{ZrO_2}} \times 100\% \quad (4)$$

Filter micropore saturation for Filters 1.1, 1.2, 1.3, 2.3, 3.1 and 3.2 were plotted against filter thickness from entry to exit side of the filters. In Experiment 1, only a few micropores were filled by the manganese silicate inclusions, as shown in Figure 12 (a), (b) and (c). Large error bars indicate the local variation in percent micropore saturation for all the filtration samples obtained from Experiment 1. Mostly unfilled micropores also explains the lower filtration efficiency during this experiment. In Experiment 2, semi-liquid calcium aluminate inclusions were captured in the micropores of Filter 2.3, as

represented in Figure 12 (d). Si was observed in the captured inclusions in the micropores (Figure 10(b)), which was absent in the inclusions present at the steel melt (Figure 4). Si pickup appears to have played an important role in keeping the inclusions liquid during the saturation of micropores. Mg-spinel ($MgO.Al_2O_3$) was also formed at the metal-filter micropore interface due to an exchange reaction indicated in Equation (5), which explains the higher filtration efficiency of calcium aluminate inclusions compared to manganese silicate inclusions. During Experiment 3, most of the filter micropores were filled by the complex liquid inclusions, as shown in Figure 12 (e) and (f), which explains the high filtration efficiency during the industrial trial.

$$(Al_2O_3)_{in\ calcium\ aluminate} + (MgO)_{in\ filter} = (MgO.Al_2O_3)_{at\ metal\text{-}filter\ macropore\ interface} \quad (5)$$

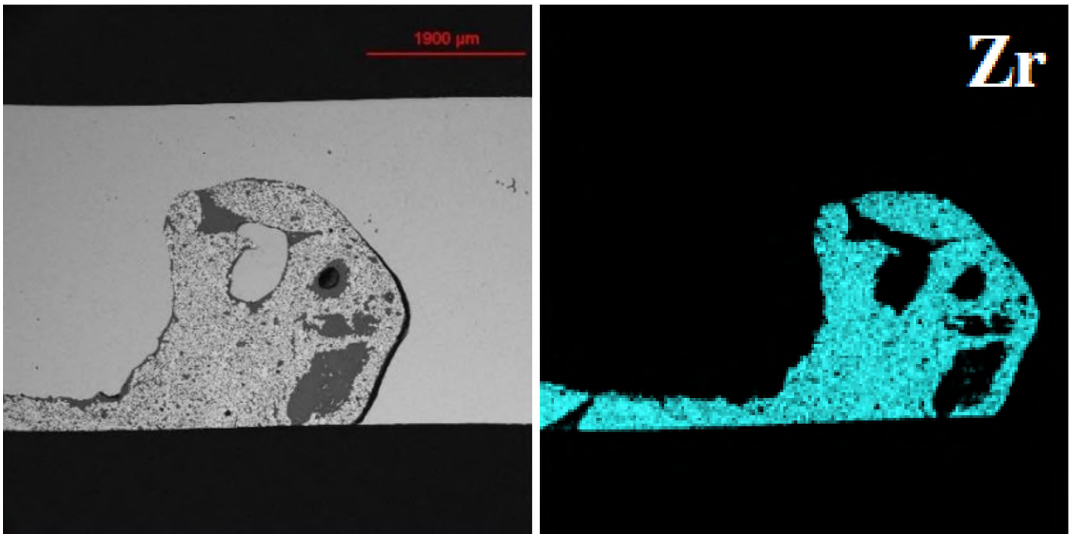

(a) (b)

Figure 11. (a) SEM image showing filter open micropores captured complex liquid inclusions in Experiment 3, (b) elemental mapping: Mn and (c) elemental mapping: Zr.

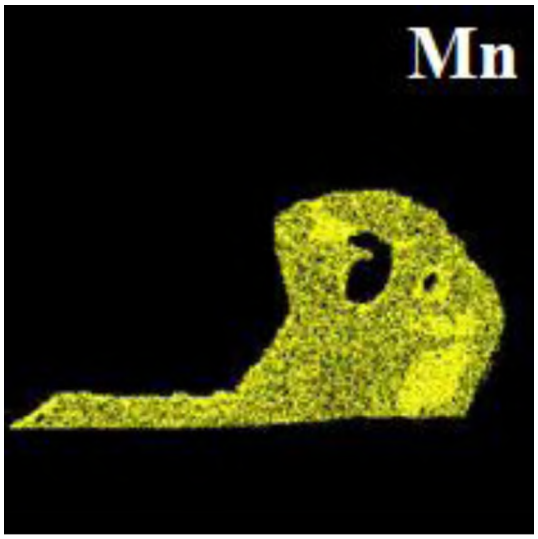

(c)

Figure 11. (a) SEM image showing filter open micropores captured complex liquid inclusions in Experiment 3, (b) elemental mapping: Mn and (c) elemental mapping: Zr (cont.).

The percentage of micropore saturation decreased exponentially from entry to exit side of the filters for all the cases, except for Filter 3.1, where a constant and fully saturated level was observed. Liquid inclusions come to the contact of the filter surface and due to interfacial tension forces, these inclusions were drawn into the filter open micropores. At higher the inclusion loading, there is a higher the probability for the inclusion to contact the filter wall and become captured in the filter micropores. During laboratory-scale experiments, only 7kg of steel was passed through the filters used, and hence the filter micropores were only partially filled. The entry side of the filter has a higher probability of capturing the liquid inclusions because the inclusion concentration decreases through the filter as inclusions are captured as steel flows towards the exit side of the filter. An exponential trend in captured inclusion concentration was therefore observed.

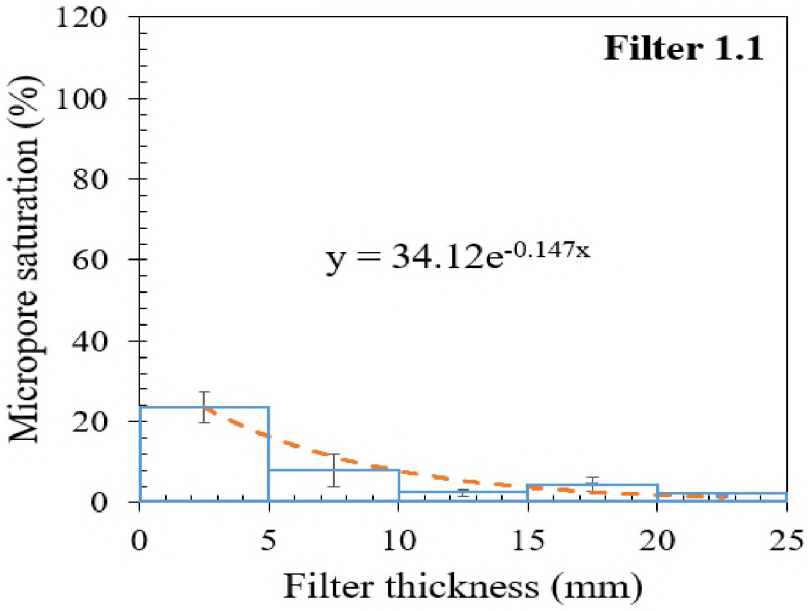

(a)

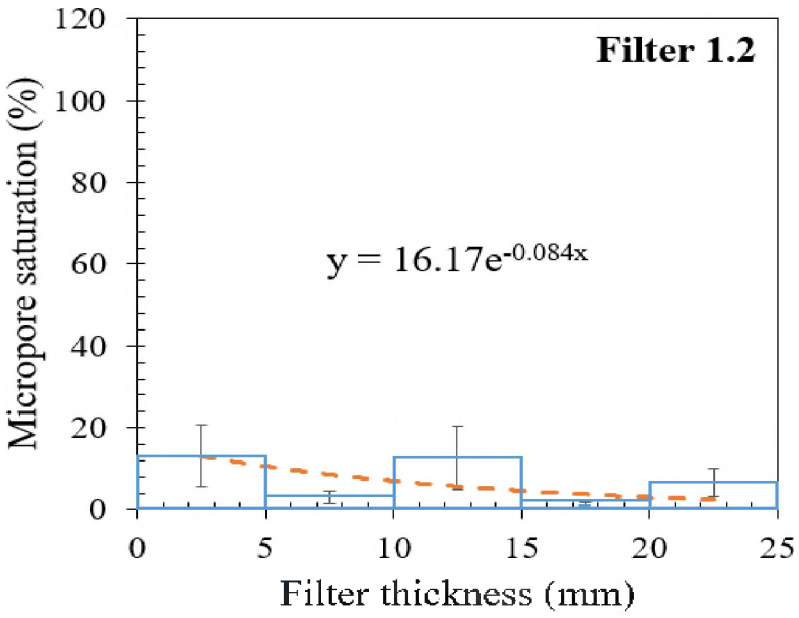

(b)

Figure 12. Percent micropore saturation against the filter thickness for: (a) Filter 1.1, (b) Filter 1.2, (c) Filter 1.3, (d) Filter 2.3, (e) Filter 3.1 and (f) Filter 3.2.

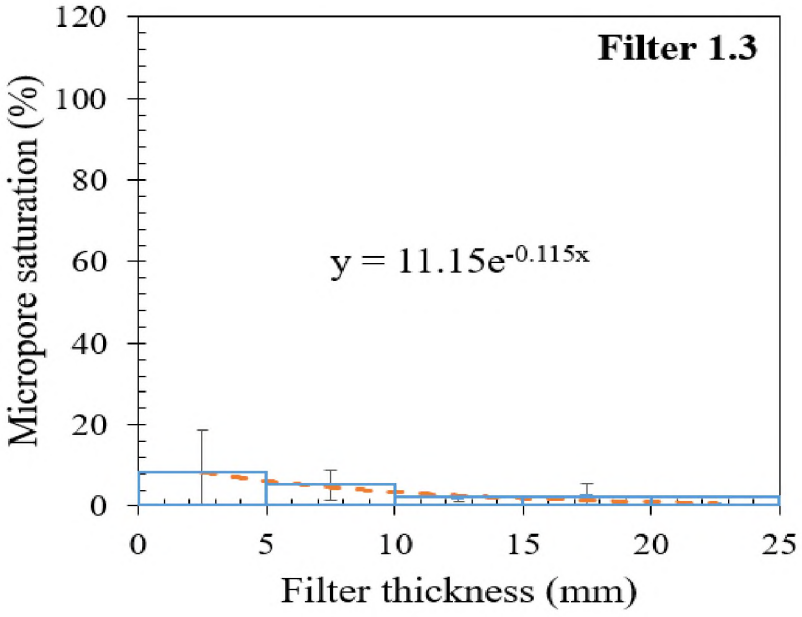

(c)

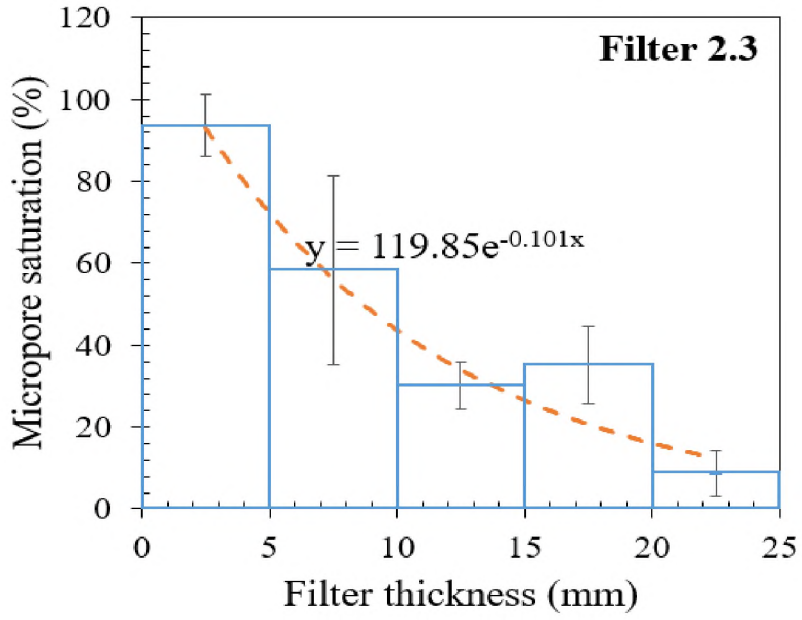

(d)

Figure 12. Percent micropore saturation against the filter thickness for: (a) Filter 1.1, (b) Filter 1.2, (c) Filter 1.3, (d) Filter 2.3, (e) Filter 3.1 and (f) Filter 3.2 (cont.).

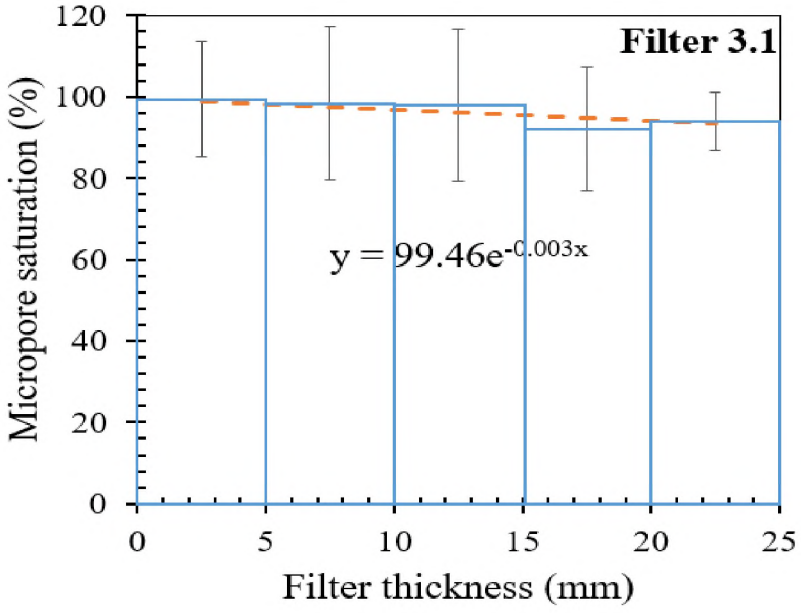

(e)

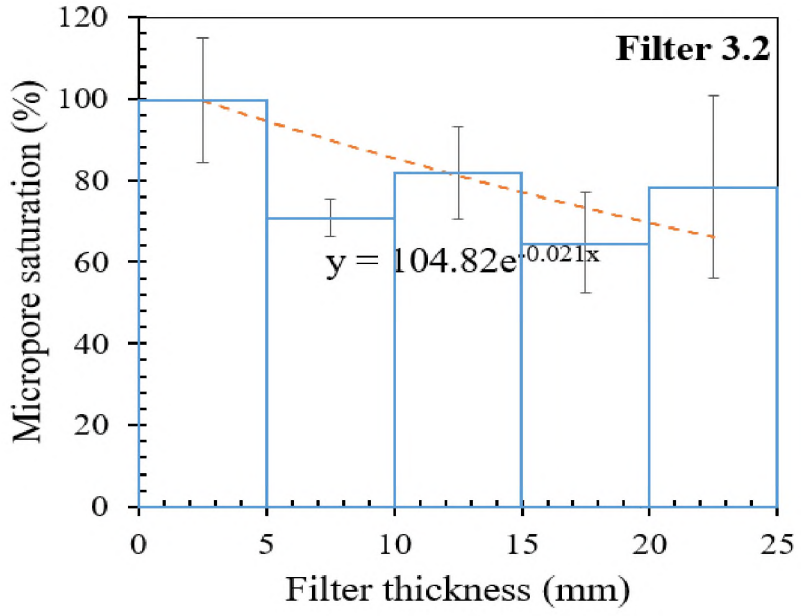

(f)

Figure 12. Percent micropore saturation against the filter thickness for: (a) Filter 1.1, (b) Filter 1.2, (c) Filter 1.3, (d) Filter 2.3, (e) Filter 3.1 and (f) Filter 3.2 (cont.).

In the case of Experiment 3, 821kg of liquid steel passed through the filters for a longer time period (61s for Ladle 3.1 and 58s for Ladle 3.2) compared to the laboratory-scale experiments (varying from 12-17s), and hence the filter surfaces had a much higher probability to capture the liquid inclusions and become saturated. Therefore, in both the filters in Experiment 3, most of the micropores were observed to be nearly completely filled by the complex liquid inclusions generated. Ladle 3.1 had a longer holding time (770s) than Ladle 3.2 (647s), and therefore steel melt from Ladle 3.1 had higher inclusion loading than Ladle 3.2. Hence, the steel melt passing through Filter 3.1 was found to be more saturated than Filter 3.2, as shown in Figure 8(c), 12(e) and 12(f). Filter 3.1 was completely saturated throughout the filter thickness, whereas, Filter 3.2 was only saturated at the filter inlet and then decreased exponentially towards the exit side, which indicated that the exponential capturing trend became constant after complete micropore saturation and then continuous liquid film started to build up at the metal- filter macropore interface.

Liquid inclusions first enter at the filter micropores following an exponential trend, as observed in Figure 12 (a), (b) and (c). Next the filter micropores at the entry side of the filter become saturated first, followed by gradual micropore saturation towards the exit side, as shown in Figure 12 (d) and (f). Finally, all the filter micropores become saturated and continuous liquid-film starts to build up at the metal- filter macropore interface, as represented in Figure 12 (e). This mechanism can be explained by the following rate equations, Equation 6 and 7, where, c is concentration of liquid inclusion at time t and k is the rate constant. A schematic of filter micropore saturation with increased inclusion loading is represented in Figure 13.

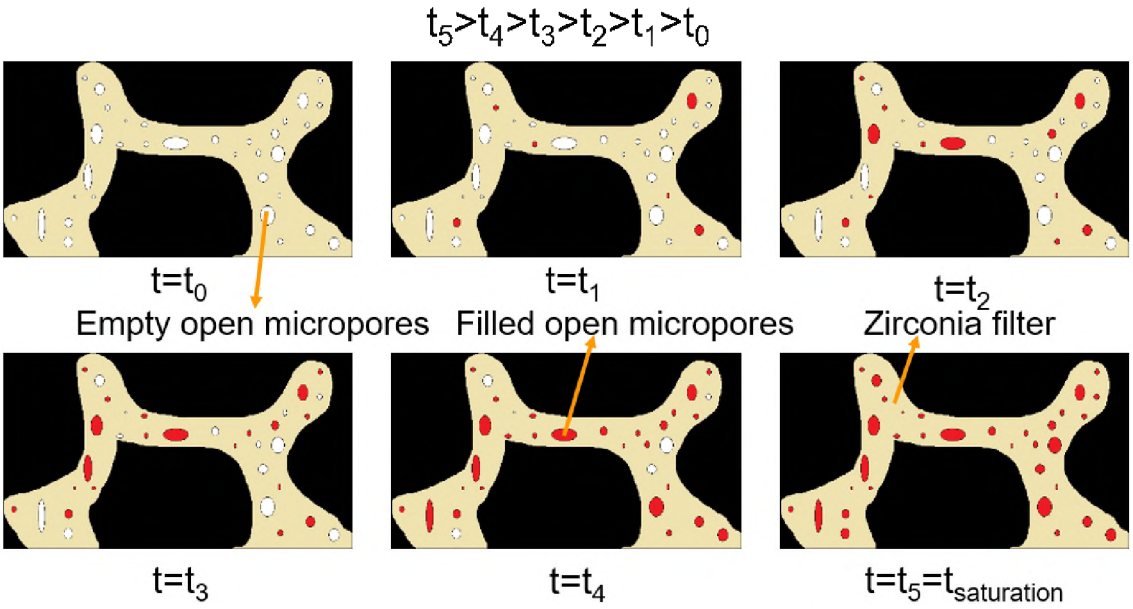

Figure 13. Saturation of filter open micropores with increased inclusion loading due to a prolonged filtration time.

$$\frac{dc}{dt} = kc, when\ filter\ micropores\ are\ not\ completely\ saturated \quad (6)$$

$$\frac{dc}{dt} = 0, when\ filter\ micropores\ are\ completely\ saturated \quad (7)$$

6. CONCLUSIONS

Two laboratory-scale experiments and one industrial-scale experiment were conducted using magnesia-stabilized zirconia 10ppi foam filters to investigate the filtration efficiency and inclusion attachment mechanism for several types of liquid inclusions. In all three experiments, the liquid inclusions were found to be removed effectively by filtration. The following conclusions can be drawn from these experimental trials:

1. In laboratory-scale experiments using teapot style ladles, the third mold cast had the highest total oxygen content and inclusion area fraction. The steel melt entering to those molds were from the top part of the ladle, where the possibility of reoxidation was at a maximum.
2. The filtration efficiency was also highest for the third mold cast in both laboratory-scale experiments supporting filtration models that predict that filtration efficiency is directly proportional to the initial inclusion concentration. For the current mold design, the maximum filtration efficiency was found to be 24% (by total oxygen content method) for manganese silicate inclusions, whereas, the maximum filtration efficiency for calcium aluminate inclusion was 46% (by total oxygen content method).
3. The higher filtration efficiency for calcium aluminate inclusions was partly due to exchange reaction at the metal-filter macropore interface, where alumina embedded in calcium aluminate reacts with magnesia present in filter to form spinel at the metal-filter macropore interface. The increase in efficiency may also be related to the presence of semi-solid inclusions in the Ca treated steel.
4. In the industry-scale experiment, maximum filtration efficiency was found to be 58% (by total oxygen content method). Most of the filter micropores were found to be saturated during this experimental trial.
5. During all these experiments, the larger inclusions (>5μm) were found to be more effectively removed than smaller inclusions. Larger inclusions also lead to higher filtration efficiency, due to their higher probability of attachment to the filter surface.

6. Liquid non-metallic inclusions were found to be captured by the ceramic foam filter, with their concentration first following an exponential trend until filter micropore saturation is reached. A constant level of micropore saturation was observed once the filter micropores were filled completely. Upon saturation, liquid inclusions can no longer be drawn into the micropores and they begin to build up at the metal-filter macropore interface, where the risk of inclusion release from the filter interface is increased. Two distinct mechanisms for inclusion capture and retention have been identified for the filtration of liquid inclusions: micropore capture and macropore interface attachment.

ACKNOWLEDGEMENTS

The authors wish to gratefully acknowledge the financial support and technical guidance from the industry mentoring committee of Peaslee Steel Manufacturing Research Center, Missouri University of Science and Technology. Special thanks go to Foseco for the material donation for this study. Authors would like to appreciate the help and support from Mr. Roger Broman and all the staffs from MetalTek International-Carondelet Division to carry out the industrial-scale experiment. The authors would also like to thank Logan Huddleston, Dominic Croce, Ife Siffre, Jacob Bartch and Caelen Johnson for their help during the experiments and sample preparations.

REFERENCES

1. H. Ouchida, K. Chijiiwa, J. Hoshino and K. Nishioka, "Fatigue Strength of Carbon-Steel Castings", *Bulletin of JSME*, 10 (39), p. 438 (1967).

2. A. Kinzel, "Method of Casting Steel Ingots", USA Patent (1932).

3. E. Ryntz, R. Schroeder, W. Chaput and W. Rassenfoss, "The Formation of Blowholes in Nodular Iron Castings", *AFS Transactions*, 91, p. 161, (1983)

4. R. Fruehan, "The Making, Shaping and Treating of Steel, 11 ed.; Vol. Steelmaking and Refining", AIST: Pittsburgh, PA, USA (1998).

5. W. Simmons, "Influence of Metal Filtration on the Production of High Integrity Cast Products", *Foundry Trade Journal*, January, p. 24. (1985).

6. C. Aneziris, S. Dudczig, J. lkova, M. Emmel and G. Schmidt, "Alumina Coatings on Carbon Bonded Alumina Nozzles for Active Filtration of Steel Melts", *Ceramics International*, 39, p. 2835 (2013).

7. W. Sutton, J. Palmer and J. Morris, "Development of Ceramic Foam Materials for Filtering High Temperature Alloys", *AFS Transactions*, 93, p. 339 (1985).

8. Z. Xu and F. Mampaey, "Mold Filling of Horizontal Castings and Influence of a Filter", *AFS Transactions*, 105, p. 853 (1997).

9. R. Morales, O. Davila-Maldonado, A. Adams, L. Oliveira and B. Alquist, "Computer and Fluid Flow Modeling of Filtration Mechanisms in Foam Filters". *AFS Transactions*, 116, p. 715 (2008).

10. D. Apelian, R. Mutharasan and S. Ali, "Removal of Inclusions from Steel Melts by Filtration", *Journal of Materials Science*, 20, p. 3501 (1985).

11. Foseco (Vesuvius): https://www.vesuvius.com.

12. S. Ali, R. Mutharasan, D. Apelian, "Physical Refining of Steel Melts by Filtration", *Metallurgical Transaction B*, 16B, p. 725 (1985).

13. K. Janiszewski and Z. Kudlinski, "The Influence of Non-Metallic Inclusions Physical State on Effectiveness of the Steel Filtration Process", *Steel Research International*, 77 (3), p. 169 (2006).

14. K. Raiber, P. Hammerschmid and D. Janke, "Experimental Studies on Al_2O_3 Inclusions Removal from Steel Melts Using Ceramic Filters", *ISIJ International*, 35 (4), p. 380 (1995).

15. L. Aubrey, J. Schmahl and M. Cummings, "Application of Advanced Reticulated Ceramic foam filter Technology to Produce Clean steel Castings", *AFS Transactions*, 101, p. 59 (1993).

16. K. Uemura, M. Takahashi, S. Koyama and M. Nitta, "Filtration Mechanism of Non-metallic Inclusions in Steel by Ceramic Loop Filter", *ISIJ International*, 32 (1), p. 150 (1992).

17. E. Kawecka-Cebula, Z. Kalicka and J. Wypartowicz, "Filtration of Nonmetallic Inclusions in Steel", *Archives of Metallurgy and Materials*, 51 (2), p. 261 (2006).

18. S. Chakraborty, R. O'Malley, L. Bartlett and L. Huddleston, "Effect of Physical State of Non-metallic Inclusions on the Accumulation Within Magnesia-Stabilized Zirconia Foam Filters", *Proceedings of the Iron and Steel Technology Conference*, Pittsburgh, PA, USA, p. 1029 (2019).

19. S. Chakraborty, R. O'Malley, L. Bartlett and M. Xu, "Efficiency of Solid Inclusion Removal from the Steel Melt by Ceramic Foam Filter: Design and Experimental Validation", *AFS Transactions*, 126, p. 325 (2018).

20. FactSage™ 7.2: www.factsage.com.

21. N. Verma, P. Pistorius, R. Fruehan, M. Potter, M. Lind and S. Story, "Transient Inclusion Evolution During Modification of Alumina Inclusions by Calcium in Liquid Steel: Part II. Results and Discussion", *Metallurgical and Materials Transactions B*, 42B, p. 720 (2011).

22. A. Cramb and I. Jimbo, "Interfacing Considerations in Continuous Casting", *Trans. of the ISS*, 6, p. 43 (1989).

23. J. Unosson, C. Persson and H. Engqvist, "An evaluation of methods to determine the porosity of calcium phosphate cements", *Journal of Biomedical Materials Research Part B: Applied Biomaterials*, 103B, p. 62 (2015).

SECTION

3. CONCLUSIONS AND RECOMMENDATIONS

3.1. CONCLUSIONS

The present work discussed filtration of both solid and liquid non-metallic inclusions using ceramic foam filter. Filtration during steel casting has been studied before by many researchers, though the basic difference in filtration mechanisms for solid and liquid inclusions removal was not understood very clearly. A mold assembly with a special rigging system was designed using fluid flow and solidification simulation software to study the efficiency of both solid and liquid inclusion removal by ceramic foam filtration. The design employs two Y-block castings in a single mold assembly, one with a filter in the runner and one without a filter. Using this design three mold sets were prepared, for each laboratory-scale experiment, which were filled from a single ladle to observe the effects of varying amounts of incoming inclusions on filtration efficiency in a single heat.

It is evident from this current study that both solid and liquid inclusions were captured effectively by magnesia stabilized zirconia 10ppi foam filters. The current study identified different capturing mechanisms for both solid and liquid inclusions. Also, the inclusion distribution through the filter thickness provided the information about the capture kinetics. Industrial-scale experiment was also conducted to understand the filtration processes with high inclusion loading, to observe any changes in the distribution of captured inclusions. SEM/EDS elemental mapping combined with quantitative

metallography and AFA analysis appear to be useful tools for quantifying inclusion removal efficiency and inclusion capture during molten metal filtration. Cathodoluminescence was also found to be a useful tool to identify the alumina inclusions captured by zirconia filters, and the interactions that occur between the filter and captured inclusions.

Floatation of some of the inclusions inside the mold cavity also contributed to inclusion removal. Filtered casting side of all three molds showed inclusion removal due to floatation in the mold cavity. Both filtration and floatation mechanisms appear to play an important role for inclusion removal. The combined effect is larger than filtration alone.

Solid inclusions were captured within the filter element by deep bed filtration and accumulated on the metal-filter macropore interface within the filter. Magnesia used to stabilize the zirconia in the filter reacted with the alumina inclusions present in the steel melt to form Mg-Al spinel and this further helped to capture the solid alumina inclusions. The entry side volume of the filter captured more inclusions than the exit side, and the amount captured decayed exponentially towards the exit side of the filter. The inclusion distribution through the filter followed a first order capture mechanism.

Liquid manganese silicate inclusions were mostly captured and held within the filter micropores. The presence of liquid manganese silicate inclusions was also observed at the metal-filter interface in some samples. The concentration of manganese silicate inclusions in the filter micropores decreased exponentially from the entry side to the exit side of the filter. A dual capturing mechanism has been established for liquid manganese silicate inclusions, which is a new addition to the literature.

Both solid and semi-liquid calcium aluminate inclusions were found to be captured by the magnesia-stabilized zirconia 10ppi foam filter. Solid calcium aluminate inclusions were captured only at the metal-filter macropore interface, whereas, the semi-liquid calcium aluminate inclusions were found at both filter micropores and metal-filter macropore interface. Alumina embedded in calcium aluminate inclusions reacted with magnesia present in filter to form Mg-Al spinel at the metal-filter macropore interface.

In industry-scale experiment, complex liquid non-metallic inclusions were found to be captured by the ceramic foam filter, with their concentration first following an exponential trend until filter micropore saturation is reached. A constant level of micropore saturation was observed once the filter micropores were filled completely. Upon saturation, liquid inclusions can no longer be drawn into the micropores and they begin to build up at the metal-filter macropore interface, where the risk of inclusion release from the filter interface is increased. Two distinct mechanisms for inclusion capture and retention have been identified for the filtration of liquid inclusions: micropore capture and macropore interface attachment.

Successively teemed molds using a bottom pour teapot-style ladle were observed to have increasing incoming inclusion concentrations. This is likely due to the reoxidation in the ladle during holding and pouring. The third molds had the highest total oxygen contents or inclusion area fractions, as the steel melt entering to those molds were coming from the top part of the ladle, where chances of reoxidation was maximum. The filtration efficiency was also maximum for the third molds in all the laboratory-scale experiments, as the filtration efficiency is directly related to the initial inclusion concentration. During all these experiments, the larger inclusions (>5μm) were found to

be more effectively removed than the smaller inclusions. Larger inclusions lead to higher filtration efficiency, due to their higher probability of getting attached to the filter surface.

3.2. RECOMMENDATIONS

Captured solid inclusions were found to be distributed exponentially following first order kinetics. In the current study, liquid inclusions were found to be captured by the filter micropores first, followed by a liquid-film built up at the metal-filter macropore interface. A kinetic model can be developed for this newly discovered capturing mechanism for liquid inclusions. If successful, it can be utilized not only to understand the capture kinetics or capturing mechanism of liquid inclusions, but also it will help to determine the capacity of the filter micropores of capturing these liquid inclusions. With the known filtration capacity, the ceramic filters possibly can be installed in the tundish or submerged entry nozzle, which may extend its application to the continuous steel casting.

3D printed zirconia filters can also be utilized for filtration of steel melt. Industrial filtration samples using 3D printed zirconia filters were received and analyzed at Missouri S&T. This experiment was carried out to filter SS 321 LC deoxidized with CaSiBa-ferroalloy to generate complex liquid inclusions. Two different filter pore sizes, 8mm/cell and 10mm/cell were used during this experiment as shown in Figure 3.1. Preliminary study showed that complex liquid inclusions were captured effectively at both filter micropores and metal-filter macropore interface, as represented in Figure 3.2.

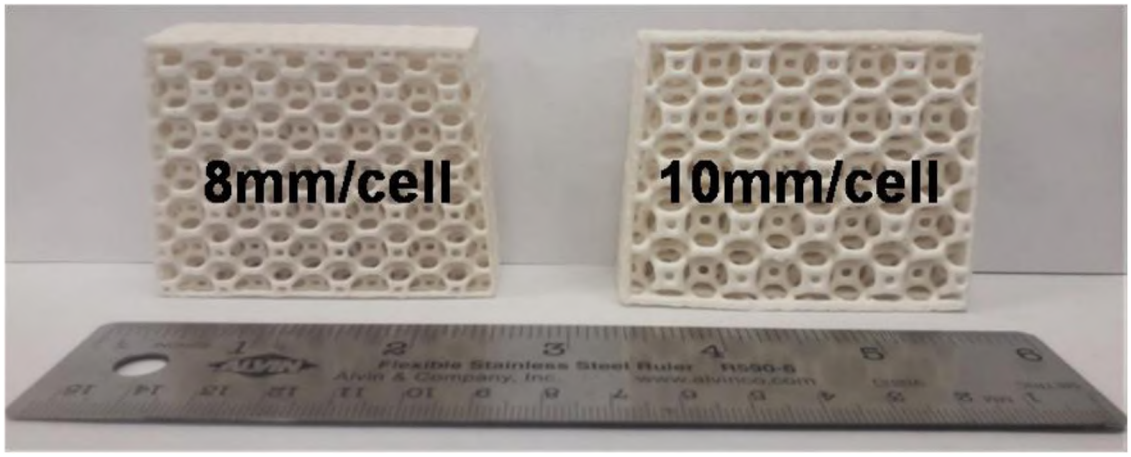

Figure 3.1. 3D printed zirconia filters.

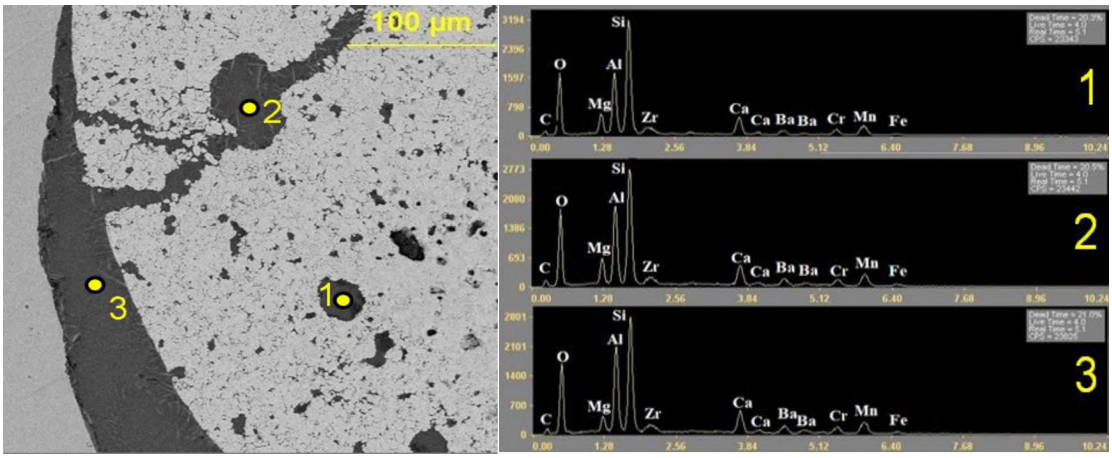

Figure 3.2. Complex liquid inclusions were captured both at filter micropores and metal-filter macropore interface.

In future, a mold can be designed using fluid dynamics and solidification simulation software, which can be utilized to carry out laboratory-scale, controlled environment experiments to compare the filtration efficiency and inclusion capture mechanism of 3D printed ceramic filters with that of the conventional ceramic foam or other types of filters.

APPENDIX A.

STEEL GRADE SELECTION

Thermodynamic simulations suggested that plain carbon steel can produce more non-metallic inclusions compared to both SS 316 and SS 321LC, provided all other experimental conditions remain same. Due to low superheat of plain carbon steel (50-60°C only for our current setup) available during tapping from the furnace, the steel melt quickly solidified during casting resulting in misruns or cold shuts. Both SS 316 and SS 321LC provided minimum 230°C superheat for the experiments, which was enough to avoid premature solidification of the molten steel when it passed through the ceramic filter during casting operations. Hence, stainless steel 316 and 321LC grades were selected for the experimental trials.

APPENDIX B.

FILTER OPEN MICROPOROSITY CALCULATION

To calculate filter open microporosity, two different methods were utilized. In Paper II, scanning electron microscopic images of unused filters were processed using ImageJ software to estimate the open microporosity of the filter. But there was a high chance of over-estimation of open microporosity by this method as on a few occasions the closed micropores of the filter may not be clearly distinguished from the open micropores. To avoid this error, a modified technique was adapted in Paper III. In this new method, Archimedes' principle was utilized to estimate the open microporosity of the unused filter using water as wetting medium.

Further, this calculated open microporosity of the filter was converted into area ratio of filter webs (considering only solid zirconia excluding the open micropores) to the open micropores. Area ratio of liquid inclusions to zirconia was estimated using SEM/EDS mapping of used filtration samples. Combining these two ratios, percent micropore saturation of the filtration samples were calculated.

BIBLIOGRAPHY

1. E. Turkdogan, "Fundamentals of Steelmaking", Institute of Materials: London, Great Britain (1996).

2. R. Fruehan, "The Making, Shaping and Treating of Steel, 11 ed.; Vol. Steelmaking and Refining", AIST: Pittsburgh, PA, USA (1998).

3. C. Aneziris, C. Schroeder, M. Emmel, G. Schmidt, H. Heller and H. Berek, "In Situ Observation of Collision between Exogenous and Endogenous Inclusions on Steel Melts for Active Steel Filtration", *Metallurgical and Materials Transactions B*, 44, p. 954 (2013).

4. L. Zhang, "Nucleation, Growth, Transport, and Entrapment of Inclusions During Steel Casting", *The Journal of The Minerals, Metals & Materials Society*, 65 (9), p. 1138 (2013).

5. L. Zhang, B. Rietow, B. Thomas and K. Eakin, "Large Inclusions in Plain-carbon Steel Ingots Cast by Bottom Teeming", *ISIJ International*, 46 (5), p. 670 (2006).

6. H. Ouchida, K. Chijiiwa, J. Hoshino and K. Nishioka, "Fatigue Strength of Carbon-Steel Castings", *Bulletin of JSME*, 10 (39), p. 438 (1967).

7. A. Kinzel, "Method of Casting Steel Ingots", USA Patent (1932).

8. E. Ryntz, R. Schroeder, W. Chaput and W. Rassenfoss, "The Formation of Blowholes in Nodular Iron Castings", *AFS Transactions*, 91, p. 161, (1983)

9. L. Zhang and B. Thomas, "Inclusion Nucleation, Growth, and Mixing During Steel Deoxidation", Continuous Casting Report No. 200206, University of Illinois at Urbana-Champaign, IL, USA, p. 1 (2002).

10. Z. Deng and M. Zhu, "Evolution Mechanism of Non-metallic Inclusions in Al-Killed Alloyed Steel during Secondary Refining Process", *ISIJ International*, 53 (3), p. 450 (2013).

11. W. Simmons, "Influence of Metal Filtration on the Production of High Integrity Cast Products", *Foundry Trade Journal*, January, p. 24. (1985).

12. O. Adaba, "Formation and Evolution of Spinel in Aluminum Killed Calcium Treated Linepipe Steels" MS Thesis: Missouri S&T, Rolla, MO, USA (2015).

13. Y. Jin, Z. Liu and R. Takata, "Nucleation and Growth of Alumina Inclusion in Early Stages of Deoxidation: Numerical Modeling", *ISIJ International*, 50 (3), p. 371 (2010).

14. H. Yin, H. Shibata, T. Emi and M. Suzuki, "*"In-situ"* Observation of Collision, Agglomeration and Cluster Formation of Alumina Inclusion Particles on Steel Melts", *ISIJ International*, 37 (10), p. 936 (1997).

15. L. Wang, J. Li, S. Yang, C. Chen, H. Jin and X. Li, "Coarsening Behavior of Particles in Fe-O-Al-Ca Melts", *Scientific Reports*, 9, p. 3670 (2019).

16. D. Gaskell, "Introduction to the Thermodynamics of Materials. 5 ed.", Taylor & Francis Group, LLC: New York, NY, USA (2008).

17. M. Faraji, D. Wilcox, R. Thackray, A. Howe, I. Todd and P. Tsakiropoulos, "Quantitative Characterization of Inclusions in Continuously Cast High-Carbon Steel", *Metallurgical and Materials Transactions B*, 46, p. 2490 (2015).

18. C. Pfeiler, M. Wu and A. Ludwig, "Influence of Argon Gas Bubbles and Non-metallic Inclusions on the Flow Behavior in Steel Continuous Casting", *Materials Science and Engineering: A*, 115, p. 413 (2005).

19. P. Tassot and N. Reichert, "Ways of Improving Steel Quality in the Tundish", *Metallurgical Research & Technology*, 107 (5), p. 179 (2010).

20. S. Abdelaziz, G. Megahed, I. El-Mahallawi and H. Ahmed, "Control of Ca Addition for Improved Cleanness of Low C, Al Killed Steel", *Ironmaking & Steelmaking*, 36 (6), p. 432 (2009).

21. C. Aneziris, S. Dudczig, J. lkova, M. Emmel and G. Schmidt, "Alumina Coatings on Carbon Bonded Alumina Nozzles for Active Filtration of Steel Melts", *Ceramics International*, 39, p. 2835 (2013).

22. W. Sutton, J. Palmer and J. Morris, "Development of Ceramic Foam Materials for Filtering High Temperature Alloys", *AFS Transactions*, 93, p. 339 (1985).

23. Z. Xu and F. Mampaey, "Mold Filling of Horizontal Castings and Influence of a Filter", *AFS Transactions*, 105, p. 853 (1997).

24. R. Morales, O. Davila-Maldonado, A. Adams, L. Oliveira and B. Alquist, "Computer and Fluid Flow Modeling of Filtration Mechanisms in Foam Filters". *AFS Transactions*, 116, p. 715 (2008).

25. M. Jacobs, "Filters: The Hows & Whys", *Engineered Casting Solutions*, Fall, p. 50 (2001).

26. D. Apelian, R. Mutharasan and S. Ali, "Removal of Inclusions from Steel Melts by Filtration", *Journal of Materials Science*, 20, p. 3501 (1985).

27. Foseco (Vesuvius): https://www.vesuvius.com.

28. S. Ali, R. Mutharasan, D. Apelian, "Physical Refining of Steel Melts by Filtration", *Metallurgical Transaction B*, 16B, p. 725 (1985).

29. K. Janiszewski and Z. Kudlinski, "The Influence of Non-Metallic Inclusions Physical State on Effectiveness of the Steel Filtration Process", *Steel Research International*, 77 (3), p. 169 (2006).

30. K. Janiszewski, "Influence of Slenderness Ratios of a Multi-hole Ceramic Filters at the Effectiveness of Filtration of Non-metallic Inclusions from Liquid Steel", *Archives of Metallurgy and Materials*, 57 (1), p. 135 (2012).

31. J. Day and H. Kind, "The Development and Application of Cellular Ceramic Filters for Gray and Ductile Iron", *AFS Transactions*, 92, p. 339 (1984).

32. K. Uemura, M. Takahashi, S. Koyama and M. Nitta, "Filtration Mechanism of Non-metallic Inclusions in Steel by Ceramic Loop Filter", *ISIJ International*, 32 (1), p. 150 (1992).

33. K. Raiber, P. Hammerschmid and D. Janke, "Experimental Studies on Al_2O_3 Inclusions Removal from Steel Melts Using Ceramic Filters", *ISIJ International*, 35 (4), p. 380 (1995).

34. L. Aubrey, J. Schmahl and M. Cummings, "Application of Advanced Reticulated Ceramic foam filter Technology to Produce Clean steel Castings", *AFS Transactions*, 101, p. 59 (1993).

35. K. Janiszewski and Z. Kudlinski, "Removal of Liquid Non Metallic Inclusion from Molten Steel Using the Method Filtration", *Metal*, Hradec and Moravicí, Czech Republic (2006).

36. J. Stamper, "The Filtration of Steel Castings with Ceramic Foam Filters", *AFS Transactions*, 93, p. 867 (1985).

37. T. Stone and P. Day, "Cellular Ceramic Steel Foundry Filter Development", *AFS Transactions*, 93, p. 87 (1985).

38. A. Artz, "Filtration of Ferrous Metals", *Modern Casting*, March, p. 24 (1986).

39. T. Johnson, H. Kind, J. Wallace, C. Nieh and H. Kim, "Laboratory and Foundry Performance Characterization of Extruded Cellular Ceramic Filters for Steel Foundry Applications", *AFS Transactions*, 97, p. 879 (1989).

40. J. Hitchings and S. Clark, "Refractory Cloth Filtration of Ductile Iron and the Mechanism of Inclusion Trapping", *AFS Transactions*, 98, p. 401 (1990).

41. P. Bates and R. Kent, "The Use of Ceramic Foam Filters in the Production of High Integrity Steels and Ni-base Alloys", *ISIJ International*, 32 (5), p. 682 (1992).

42. D. Apelian and R. Mutharasan, "Filtration: A Melt Refining Method", *Journal of Metals*, September, p. 14 (1980).

43. P. Sanford and S. Sibley, "Optimization of Al Casting Productivity Using Foam Filter Technology and Application, *AFS Transactions*, 104, p. 1063 (1996).

44. W. Baker, "Testing Filters for Steel Castings", *AFS Transactions*, 94, p. 215 (1986).

45. J. Morris, S. Sahu and U. Sievers, "Advanced Reticulated Ceramic Metal Filters and Performance Results from Select Steel Foundries", *AFS Transactions*, 98, p. 671 (1990).

46. B. Sirrell and J. Campbell, "Mechanism of Filtration in Reduction of Casting Defects Due to Surface Turbulence During Mold Filling", *AFS Transactions*, 105, p. 645 (1997).

47. V. Singh, "Inclusion Modification in Steel Castings Using Automated Inclusion Analysis", MS Thesis: Missouri S&T, Rolla, MO, USA (2009).

48. V. Thapliyal, "Inclusion Engineering in Mn-Si De-oxidized Steel for Thin-strip Casting", PhD Dissertation: Missouri S&T, Rolla, MO, USA (2015).

49. M. Harris, "A Study on Non-Metallic Inclusions in Foundry Steel Process", MS Thesis: Missouri S&T, Rolla, MO, USA (2016).

50. O. Adaba, "Oxide Inclusion Evolution and Factors that Influence Their Size and Morphology", PhD Dissertation: Missouri S&T, Rolla, MO, USA (2019).

51. K. Janiszewski, K. Gryc and M. Tkadleckova, "Change of Slenderness Ratios of Multi-hole Ceramic Filters from $\lambda = 1{,}67$ to $\lambda = 3{,}34$ as a Factor Determining the Effectiveness of Steel Filtration Process", *Metal*, Brno, Czech Republic (2012).

52. E. Kawecka-Cebula, Z. Kalicka and J. Wypartowicz, "Filtration of Nonmetallic Inclusions in Steel", *Archives of Metallurgy and Materials*, 51 (2), p. 261 (2006).

53. A. Cramb and I. Jimbo, "Interfacing Considerations in Continuous Casting", *Trans. of the ISS*, 6, p. 43 (1989).

54. F. Heuzeroth, J. Fritzsche and U. Peuker, "Wetting and Its Influence on the Filtration Ability of Ceramic Foam Filters", *Particuology*, 18, p. 50 (2015).

55. W. Su, T. Johnson, J. Day, J. Wallace and F. Li, "The Development and Characterization of Extruded Cellular-Ceramic Filters for Steel Foundry Applications", *AFS Transactions*, 96, p. 161 (1988).

56. R. Olson and L. Martins, "Cellular Ceramics in Metal Filtration", *Advanced Engineering Materials*, 7 (4), p. 187 (2005).

57. C. Tian, "On the Removal of Non-Metallic Inclusions from Molten Steel through Filtration", PhD Dissertation: McGill University, Montreal, Quebec, Canada (1990).

58. F. Acosta, A. Castillejos, J. Almanza and A. Flores, "Analysis of Liquid Flow through Ceramic Porous Media Used for Molten Metal Filtration", *Metallurgical and Materials Transactions B*, 26B, p. 159 (1995).

59. C. Tian and R. Guthrie, "Direct Simulation of Initial Filtration Phenomena within Highly Porous Media", *Metallurgical and Materials Transactions B*, 26B, p. 537 (1995).

60. F. Acosta and A. Castillejos, "A Mathematical Model of Aluminum Depth Filtration with Ceramic Foam Filters: Part I. Validation for Short-Term Filtration", *Metallurgical and Materials Transactions B*, 31B, p. 491 (2000).

61. F. Acosta and A. Castillejos, "A Mathematical Model of Aluminum Depth Filtration with Ceramic Foam Filters: Part II. Application to Long-Term Filtration", *Metallurgical and Materials Transactions B*, 31B, p. 503 (2000).

62. O. Davila-Maldonado, A. Adams, L. Oliveira, B. Alquist and R. Morales, "Simulation of Fluid and Inclusions Dynamics during Filtration Operations of Ductile Iron Melts Using Foam Filters", *Metallurgical and Materials Transactions B*, 39B, p. 818 (2008).

63. S. Bao, T. Engh, M. Syvertsen, A. Kvithyld and M. Tangstad, "Inclusion (Particle) Removal by Interception and Gravity in Ceramic Foam Filters", *Journal of Materials Science*, 47, p. 7986 (2012).

64. A. Asad, E. Werzner, C. Demuth, S. Dudczig, A. Schmidt, S. Ray, C. Aneziris and R. Schwarze, "Numerical Modeling of Flow Conditions during Steel Filtration Experiments", *Advanced Engineering Materials*, 19, p. 1700085 (2017).

65. A. Asad, K. Chattopadhyay and R. Schwarze, "Effect of Turbulence Modeling on the Melt Flow and Inclusions Transport in a Steel Filtration Experiment", *Metallurgical and Materials Transactions B,* 49B, p. 2270 (2018).

66. J. Dumaillet and G. Wilson, "Comparison of Flow Modification Through Foundry Filters Using Both Water Modeling and Simulation Software: Part 1", *AFS Transactions*, 110, p. 187 (2002).

67. A. Adams, O. Davila-Maldonado, L. Oliveira and B. Alquist, "Enhancing filtration knowledge to improve foundry performance", *Foundry Trade Journal*, April, p. 86, (2010).

68. R. Schuhmann, J. Carrig, T. Nguyen, V. Alguine and A. Dahle, "Modeling and Validation of Molten Metal Flow in Permanent Mold Casting", *AFS Transactions*, 108, p. 599 (2000).

69. A. Schulte, S. Lekakh, V. Richards and D. Van Aken, "Modeling for Improved Casting Quality of High Aluminum Steels", *AFS Transactions*, 118, p. 437 (2010).

70. J. Campbell, "Complete Casting Handbook", Elsevier Ltd.: Oxford, UK (2011).

VITA

Soumava Chakraborty was born in Hooghly, West Bengal, India. He received his Bachelor of Science in Chemistry and Bachelor of Technology in Chemical Technology from University of Calcutta, India in 2011. After his graduation, he worked as an Executive Trainee at British Paints, New Delhi, India. In 2013 he started his graduate study and in 2015 he received his Master of Technology in Materials Science and Engineering from Indian Institute of Technology Kanpur, India. After his graduation, he continued his research there as a Senior Project Associate.

In August 2016, Soumava started his doctoral study at the Peaslee Steel Manufacturing Research Center at Missouri University of Science and Technology, Rolla, USA, under the guidance of Prof. Ronald J. O'Malley. He worked on filtration of non-metallic inclusions for foundry steelmaking. He presented his works at two international conferences-Metalcasting Congress, Fort Worth, TX, USA in 2018 and AISTech, Pittsburgh, PA, USA in 2019. In December 2020, he received his Doctor of Philosophy in Materials Science and Engineering from Missouri University of Science and Technology, Rolla, MO, USA.

Soumava was a member of American Foundry Society, Materials Advantage and Tau Beta Pi Missouri Beta Chapter. He received two Best Paper awards from American Foundry Society- Steel Division (2019) and Association of Iron and Steel Technology- Specialty Alloy & Foundry Technology Committee (2020) for his work on filtration of non-metallic inclusions.